Critical Mechanical Structures – Thermal Fluctuations and Self-Assembly

by

Deshpreet Singh Bedi

A dissertation submitted in partial fulfillment
of the requirements for the degree of
Doctor of Philosophy
(Physics)
in The University of Michigan
2017

Doctoral Committee:

Assistant Professor Xiaoming Mao, Chair
Assistant Professor Emanuel Gull
Associate Professor David K. Lubensky
Professor Michael J. Solomon
Associate Professor Kai Sun

Deshpreet Singh Bedi

dbedi@umich.edu

ORCID iD: 0000-0002-2795-1426

To my wife and family.

ACKNOWLEDGEMENTS

First and foremost, I would like to thank my advisor, Xiaoming Mao. The research contained in this dissertation is largely a result of her continual support, guidance, and care over the past few years. I will forever be grateful to her for her commitment to my success and for all the knowledge and wisdom that she has imparted to me. I would also like to acknowledge the other members of her group, with whom I shared an office and, consequently, countless invaluable discussions regarding not only our research but also much beyond: Zeb, Leyou, Shang, Di, and Shangnan.

I am also thankful to have had the opportunity to collaborate with Professor Michael Solomon and his former graduate student, Joseph Ferrar. I greatly enjoyed our many fruitful discussions and found immense value in the perspectives they were able to provide. I was fortunate to have a number of modes of interaction with Professors Kai Sun, Emanuel Gull, and David Lubensky, including attending intriguing courses taught by them, having discussions with them about my research and physics in general, as well as asking them for impromptu advice sessions. I want to thank each of them for their ever-pertinent guidance and feedback and for taking the time to serve on my dissertation committee.

The support and warm friendship of many colleagues over the years made my time in Ann Arbor supremely enjoyable, and I am glad to have forged lasting relationships with a number of them: Uttam, Marta, Shengtao, Jeremy, Jiahua, Thomas, Christine, Arash, Pedro, Alejandro, and Yue.

My time here was especially enhanced by the Michigan Sikh Sangat. I am truly blessed to have been a part of such a supportive and loving community. I was also wonderfully

fortunate to have my entire family living close by in Michigan. Spending numerous weekends with my parents, siblings, and nieces and nephew always provided me with precious relaxation and rejuvenation. It is impossible to overstate how much their unconditional love and encouragement helped propel me through my graduate years.

Finally, none of this would have been remotely achievable without the tremendous support and dedication of my amazing wife, Suneet. No words can adequately describe the lengths to which she went to ensure that my progress remain as unhindered as possible. I owe everything to her presence in my life.

TABLE OF CONTENTS

DEDICATION ii

ACKNOWLEDGEMENTS iii

LIST OF FIGURES viii

LIST OF APPENDICES xvii

ABSTRACT xviii

CHAPTER

I. Introduction 1

1.1 Critical mechanical structures and mechanical instability 1
1.1.1 The Maxwell counting rule 3
1.1.2 Examples of critical lattices 8
1.2 Self-assembly of open structures 10
1.2.1 Janus particles 12
1.2.2 Capillary interactions 13
1.3 Organization of the dissertation 15

II. Finite-temperature buckling of an extensible rod 17

2.1 Introduction 17
2.2 Model and analytic theory 19
2.2.1 The extensible-rod Hamiltonian with anharmonic terms . . 19
2.2.2 Classical ($T = 0$) Euler buckling 23

2.2.3 Fluctuation corrections to stability and finite-temperature buckling . . . 27
2.2.4 Effective force . . . 34
2.3 Monte Carlo simulations . . . 37
2.4 Conclusion and discussion . . . 39

III. Twisted-untwisted transition of the kagome lattice at finite temperature and the self-assembly of the twisted kagome lattice with Janus particles . . . 42

3.1 Introduction . . . 42
3.2 Kagome lattice preliminaries . . . 45
3.3 Zero-temperature analysis . . . 46
3.4 Finite-temperature free energy calculation . . . 51
3.4.1 Asymptotic form of the free energy . . . 56
3.4.2 The stability of the kagome lattice . . . 59
3.5 Tri-block Janus particles . . . 64
3.5.1 Derivation of the effective Hamiltonian for Janus particles . 66
3.5.2 Two-dimensional triblock Janus particles . . . 70
3.5.3 Three-dimensional triblock Janus particles . . . 74
3.5.4 Effective Hamiltonian and the phase diagram . . . 78
3.6 Discussion . . . 81

IV. Self-assembly of thin triangular prisms via capillary interactions . 83

4.1 Introduction . . . 83
4.2 Theory of capillary interactions . . . 85
4.2.1 Analytic interface height solutions . . . 85
4.2.2 Interaction energy between two capillary multipoles . . . 89
4.2.3 Contact-line boundary conditions . . . 91
4.3 Experimental system . . . 95
4.4 Methods for numerical analysis . . . 98
4.4.1 Pairwise modeling of the interaction potential using Surface Evolver . . . 98
4.4.2 Computing particle trajectories leading to pair binding . . 100
4.5 Capillary interactions of triangular prisms . . . 103

4.6 Dilute binding events 110
4.6.1 Experimental results 110
4.6.2 Simulation results 111
4.7 Discussion 117

V. Conclusion 119

5.1 Future directions 120

APPENDICES 123

BIBLIOGRAPHY 136

LIST OF FIGURES

1.1 Two-square frames consisting of bonds connecting $N = 6$ sites. (a) has 7 bonds and two floppy modes, as indicated by the dashed bonds, (b) has 8 bonds and one floppy mode, and (c) has 9 bonds and no floppy modes – it is entirely rigid. Note that, in these cases, each addition of a bond has removed one floppy mode. (d) also has 9 bonds, but the extra bond has been redundantly placed in the left square plaquette, creating a state of self stress, as indicated by the arrows on the bonds. Therefore, according to the generalized Maxwell counting rule, there is still one floppy mode, corresponding to the right square plaquette. 6

1.2 Examples of floppy modes for two-dimensional critical lattices. The left column corresponds to finite floppy modes in the (top) nearest neighbor (NN) square lattice and the (bottom) NN kagome lattice. In particular, the floppy mode for the NN kagome lattice is the uniform twisting mode that we will be considering further. Both of these deformations cost no energy as they do not change the length of the NN bonds. These finite floppy modes only apply under free boundary conditions. The right column corresponds to infinitesimal floppy modes. These floppy modes exist even under periodic boundary conditions. Note that the include of next-nearest-neighbor (NNN) bonds would gap these modes, as they would change the length of the NNN bonds. 8

2.1 (a) Illustration of an extensible rod under compression. (b) Predicted phase diagram for two-dimensional finite-temperature buckling of an extensible rod in the plane of normalized compression and temperature (as defined in Sec. 2.2). The thick black curve represents the phase boundary between the straight (unshaded) and the buckled (shaded with vertical lines) phases. The dashed curve denotes the boundary of the critical regime (light blue region) where the thermal-fluctuation correction to the effective force is of $O(\sqrt{T})$. 19

2.2 Feynman diagrams corresponding to terms in $\langle H_4 \rangle_>$. The diagrams are systematically divided into rows and columns: each row is associated with a single elastic parameter that is the coefficient of the originating term in $\langle H_4 \rangle_>$, while the columns specify which elastic parameter's renormalization the diagrams contribute to. Namely, the first column presents the basic vertex diagrams, while the second and third columns list those that renormalize τ and κ, respectively. Each external leg corresponds to a $\boldsymbol{\pi}^<$ field, and slashes denote spatial derivatives with respect to x_d. The various internal lines differentiate between the interactions and are used for index bookkeeping. 31

2.3 Predicted phase diagram for three-dimensional finite-temperature buckling of an extensible rod in the plane of normalized compression and temperature. The thick black curve represents the phase boundary between the straight (unshaded) and the buckled (shaded with vertical lines) phases. The dashed curve denotes the boundary of the critical regime (light blue region) where the thermal-fluctuation correction to the effective force is of $O(\sqrt{T})$. 35

2.4 Plots of the dimensionless effective force in both two (a) and three (b) dimensions at various values of $\bar{T}$. Note that $-\bar{f} = f/|\tau_c(0)|$. Negative values correspond to a compressive force, while positive values correspond to a stretching force. The dots on each curve indicate the transition point between the straight and buckled phases for each value of $\bar{T}$. The $\bar{T} = 0.001$ curve in three dimensions does not have a dot as there is no phase transition at that temperature; the rod remains in the straight phase. 36

2.5 Results of Monte Carlo simulations run with $\bar{\tau} = 1.3, 1.5, 1.7$ in both two ((a)-(c)) and three ((d)-(f)) dimensions. For each value of $\bar{\tau}$ and in each dimension, three different lengths were simulated. Each data point corresponds to the combined Binder cumulant value of ten independent simulations run with identical parameters. The lines connecting the data points explicitly illustrate that the Binder cumulant curves do indeed simultaneously cross at, or very close to, the respective critical temperatures. 38

3.1 (Left) The kagome lattice with lattice sites (red circles), and nearest-neighbor (NN) (solid black lines) and next-nearest-neighbor (NNN) (dashed blue lines) bonds. Note the sets of straight lines of NN bonds in three symmetry directions, which allow for states of self-stress and, consequently, floppy modes under periodic boundary conditions when NNN bonds are not present. (Right) The twisted kagome lattice. Notice that the straight lines no longer exist, so that the states of self-stress as well as floppy modes have been removed. 44

3.2 The potential energy of next-nearest-neighbor bonds connected by an anharmonic spring as given by Eq. (3.3.9). For $\kappa > 0$, the potential is single-well, so all NNN bonds are the same length – yielding a regular hexagonal cell corresponding to an untwisted kagome lattice. For $\kappa < 0$, the potential is double-well, so the energetically-preferred configuration for the hexagonal cell is one where three NNN bonds are longer than the regular-hexagon NNN bonds, and three NNN bonds are shorter. This yields an irregular hexagonal cell corresponding to a twisted kagome lattice. At zero temperature, this is what governs the structural phase transition between the kagome and twisted kagome lattices. 48

3.3 (Left) Complete phonon spectrum for the untwisted kagome lattice. Dashed lines depict frequencies at $\tau = 0$ and solid lines at $\tau = 0.01$. The inset shows the first Brillouin zone with high symmetry points Γ, M, and K indicated. There is a line of floppy modes along ΓM when $\tau = 0$ (corresponding to no NNN bonds) that are lifted to finite frequency values for all $\mathbf{q} \neq 0$ for $\tau = 0.01$. (Right) Complete phonon spectrum for the twisted kagome lattice. Dashed lines depict frequencies at $\tau = 0, \lambda = 0, \alpha = 0.15$ (NN lattice) and $\tau = 0.01, \lambda = 100, \alpha = 0.01$ (NNN lattice). Note that the two twisted kagome spectra are relatively similar, though the inclusion of the anharmonic term in the NNN potential is coupled with α necessarily being small. The value of the ω plateau for the lowest mode is well approximated by the value at M given in Eq. (3.4.30). 57

3.4 Comparisons of the value of the integral of $\ln\det\widetilde{\mathbf{D}}_{\mathbf{q}}/v_0$ over the first Brillouin zone, as computed using two methods: the asymptotic form in Eq. 3.4.33 (blue solid line), and exact values obtained by numerical integration involving the complete dynamical matrix (orange points). (Left) Untwisted kagome lattice, with $\alpha = 0$, $\lambda = 100$; (Right) twisted kagome lattice, with $\alpha = 0.01$, $\lambda = 100$. Both indicate that the asymptotic form is indeed a good analytic approximation for the exact solution. 60

3.5 Plots of the order parameter, the twisting angle α, as a function of τ for various values of reduced temperature, $\widetilde{T}$ and $\lambda = 100$. The discontinuous jumps in α occur at the transition from the untwisted kagome lattice (where $\alpha = 0$) to the twisted kagome lattice (where $\alpha \neq 0$) and are characteristic of a first-order phase transition. 63

3.6 The predicted phase diagram for the kagome and twisted kagome lattices. The transition, identified by the solid blue curve, is first order for $T > 0$. The $T = 0$ structural transition is continuous. The orange dashed curve marks where the twisted kagome lattice first appears as a metastable state (for decreasing τ or T). Both critical curves follow $\tau_c \propto -T^{2/3}$. The lined region between $\tau = 0$ and the phase boundary is the region where the kagome lattice is entropically stabilized. 64

3.7 Examples of isoenergetic open structures formed by Janus particles. (Left) The kagome lattice, with an angle between triangles (outlined in green) of 120°, formed by Janus particles with non-offset patches. (Right) The twisted kagome lattice, with an angles between triangles deviating from 120°, formed by Janus particles with offset patches. Note that while Janus particles with offset patches can potentially form a kagome lattice, depending on the patch size, offset angle, and temperature, Janus particles with non-offset patches cannot form a twisted kagome lattice, as angles that deviate from 120° are entropically disfavored. 66
3.8 A two-dimensional triblock Janus particle with one attractive patch (of angular radius ϕ_0) offset by an angle β. The four green solid lines represent the four attractive bonds of the particle separated by angles $\delta, \delta', \gamma, \gamma'$. The red arrow points to the "north" pole of the particle, defined without loss of generality to be opposite the non-offset bottom patch. The orange arrow bisects the offset patch. The black portions represent the attractive patches. 71
3.9 A three-dimensional triblock Janus particle with one attractive patch (of angular radius ϕ_0) offset by an angle β. The four green solid lines represent the four attractive bonds of the particle. The red arrow points to the "north" pole of the particle, defined without loss of generality to be opposite the non-offset bottom patch. The orange arrow, which points to the center of the offset patch, provides the third angle needed to fully specify the orientation of the particle. The black circular portions represent the attractive patches. 74
3.10 The orientational entropy of a three-dimensional triblock Janus particle as a function of twisting angle α for various patch sizes ϕ_0 and patch offset angles β. $\alpha = 0$ corresponds to bonds with nearest neighbors, yielding an untwisted kagome lattice. (Left) Orientation entropy for particles with a patch size of $\phi_0 = 45°$ offset at $\beta = 0°, 15°, 30°$. (Right) Orientational entropy for particles with patch sizes of $\phi_0 = 40°, 45°, 50°, 55°$ at a single offset angle $\beta = 30°$. 77
3.11 Values of α^*, the value of the twisting angle α with maximal entropy, as a function of the offset angle β for five different patch sizes. The black dashed line is $\alpha^* = \beta$; for all patch sizes, the value of α^* converges to this line as β increases; expectedly, the smaller the patch size, the earlier the convergence, as the twisting angle is more constrained for a smaller patch size. 77
3.12 A plot of $\tau/(\tau_0\widetilde{T})$ as a function of offset angle β and patch size ϕ_0, where $\tau_0 = \tau(\beta = 0)$ for a given patch size. The left white dashed curve is $\tau = 0$, while the right dashed curve marks where the weight for untwisted bonds $\Omega_0 = \Omega(\alpha = 0)$ first vanishes (for increasing β). The leftmost region, where $\tau > 0$, will necessarily yield an untwisted kagome lattice, whereas the rightmost region, where $\Omega_0 = 0$, yields a twisted kagome lattice. The middle region is where the temperature-dependent phase transition occurs. The three red dots correspond to the plots of the orientational weights (degeneracy factors) on the right for a patch size of $\phi_0 = 40°$. The values of β were chosen to illustrate the profile of the weight function in each of the three regions discussed above. 81

3.13 The Janus particle phase diagram as a function of offset angle β and temperature $\widetilde{T}$ for five different patch sizes. To the left of, and above, each corresponding phase boundary is the untwisted kagome phase, while to the right of, and below, is the twisted kagome phase. 82
4.1 Hexapole-like capillary interaction between triangles may lead to the self-assembly of kagome lattices. (a) Hexapole-like interactions between two bowed triangles (positive at tips and negative at edges) cause tip-to-tip binding. (b) The kagome lattice where edges of triangles form straight lines. (c,d) two twisted kagome lattices with different twisting angle. These different versions of the kagome lattice are related by a soft deformation which only changes the angle between the triangles, which leads to a negative Poisson's ratio. (e) Depending on the strength of the hexapole-like interaction, disordered assemblies of triangles may also occur. 84
4.2 Theoretical interface height profiles for particles with circular cross-sections and contact lines undulating according to prescribed multipole moments. (a) A capillary quadrupole ($m = 2$), with four alternating regions of positive and negative interface height (the equilibrium interface height far from any particles is taken to be zero), and (b) A capillary hexapole ($m = 3$) with six alternating regions of positive and negative interface height. 88
4.3 Theoretical capillary interaction potential between two capillary hexapoles as a function of separation distance, r, scaled by the diameter of the particles' circular projection, $2R$, and the particles' relative orientation, $|\theta_1 - \theta_2|$. The three insets show the interface height profile of three configurations corresponding to relative orientations of 0°, 30°, and 60° at a distance of $r/2R = 1.8$. 92
4.4 Cross-section showing the movement of a three-phase contact line between solid (S), liquid (L), and gas (G) phases with contact angle θ_c by an amount dx. The solid (dotted) line represents the initial (resultant) interface. Used in the derivation of the Young equation. 93
4.5 Close-up schematic of the surface of an arbitrary particle at an interface. $\hat{\mathbf{t}}$ is the unit tangent vector to the contact line, $\hat{\mathbf{n}}$ is the unit normal vector to the surface of the particle, and $\hat{\mathbf{b}}$ is the unit binormal vector. $\hat{\boldsymbol{\gamma}}$ is tangent to the interface and lies in the plane spanned by the vectors $\hat{\mathbf{n}}$ and $\hat{\mathbf{b}}$. The angle between $\hat{\boldsymbol{\gamma}}$ and $\hat{\mathbf{b}}$ is the contact angle, θ_c. 94
4.6 SEM images of thin, equilateral triangular microprisms from SU-8 epoxy resin. Equilateral triangle (edge length, $L = 120\,\mu$m) prisms of varying thickness (T) a) $T \sim 2.5\,\mu$m, $T/L = 1/50$, b) $T \sim 5\,\mu$m, $T/L = 1/25$, c) $T \sim 12\,\mu$m, $T/L = 1/10$, d) $T \sim 20\,\mu$m, $T/L = 1/5$. Reprinted from [109] with permission. 96
4.7 Self-assembled open networks from capillary-driven binding of thin triangular microprisms. (a) $T/L = 1/50$, (b) $T/L = 1/25$, (c) $T/L = 1/10$, and (d) $T/L = 1/5$ equilateral triangular microprisms. Scale-bars are $100\,\mu$m. Reprinted from [109] with permission. 97

4.8 Environmental SEM images of $T/L = 1/50$ triangular prisms, fixed at an air-gellan/water, illustrating interfacial deformation that follows the bowing of the prism due to contact-line pinning. (a) Positive "positional" polarity, corresponding to downward bowing. (b) Negative "positional" polarity, corresponding to upward bowing. Scale bars are $20\,\mu$m. Adapted from [109] with permission. 98
4.9 Identification of triangular prism binding states ($T/L = 1/25$). Each row of images (a)-(c) represents a different location within a network structure. The relative position of the microscope's focal plane to the air-water interface is varied by column as follows: Column (1): Microscope focal plane is $\sim$200 μm below the interface. In-focus prisms are identified with red markers. Column (2): Microscope focal plane is $\sim$200 μm above the interface. In-focus prisms are identified with blue markers. Column (3): Microscope focal plane is at the interface. Bonds between prisms with the same positional polarity are identified with blue and red connecting lines, bonds between prisms with the opposite positional polarity are identified with purple connecting lines. Column (4): Microscope focal plane is at the interface. Prism-prism bonds are identified by their positional-polarity-independent orientation: side-side (orange connecting lines), tip-tip (green connecting lines), side-side offset (brown connecting lines), tip-side (pink connecting lines). Scale-bar is $100\,\mu$m. Reprinted from [109] with permission. 99
4.10 Interface height profile for a (a) bowed-up triangular prism and a (b) bowed-down triangular prism, where the zero value is set by the equilibrium interface height at large distances from the prism. The inset in (a) is a close-up of the Surface Evolver simulation output. (c) A comparison of the interface height profile around a bowed-up triangular prism (data points) and an ideal hexapole (solid curves) as a function of angle at two different distances from the triangular prism, shown in the inset. Simulated interface height profiles for (d) two bowed-up triangular prisms and (e) one bowed-up and one bowed-down prism for both tip-to-tip and tip-to-side configurations. Zoomed-in rendering of simulated interface height profile for (f) a tip-to-tip configuration for two bowed-up prisms; and (g) a tip-to-side configuration for one bowed-up and one bowed-down prisms, illustrating the existence of a capillary bridge in both cases. 105

4.11 Numerically-simulated capillary interaction potential between two bowed-up triangular prisms, with the left prism held at 0°. This two-dimensional slice of the full three-dimensional configuration space is directly comparable to the theoretical interaction potential in Fig. 4.3. (b) All orientation angles for the triangular prism system are defined according to the convention shown: the orientations are defined by the angle a specific tip of the prism makes with the line connecting the centers of the two prisms. (c) The capillary interaction potential for two-bowed up triangular prisms in mirror-symmetric configurations as a function of the separation distance, r, on a log scale, for various orientation angle values. A dashed reference line, corresponding to the theoretical interaction potential for two ideal hexapoles, $U \sim r^{-6}$, is shown for comparison. 107

4.12 (a) Interaction energy potential values for two bowed-up triangular prisms in mirror-symmetric configurations at various separation distances. 0° corresponds to a tip-to-tip configuration, while 60° corresponds to a side-to-side configuration. Interaction energy potentials plotted as a function of orientation angles for (b) $r = 192$ and (c) $r = 132$. (d)-(f) The corresponding figures for the case of one bowed-up and one bowed-down triangular prism. 108

4.13 Optical microscopy images of the 2 types of binding trajectories observed for polar prisms ($T/L \leq 1/10$), shown for $T/L = 1/50$ (rows (a) and (b)) and $T/L = 1/25$ (rows (c) and (d)). For prisms of $T/L = 1/50$ (rows (a) and (b)), contact occurs between the 5th and 6th images of each row. For prisms of $T/L = 1/25$ (rows (c) and (d)), contact occurs in the 5th image of each row. Rows (a) and (c), tip-to-tip binding trajectory: the prisms approach and first contact occurs at the tips. The prisms then rotate into a collapsed, fully flush edge-to-edge orientation. Rows (b) and (d), tip-to-midpoint edge binding trajectory: the prisms approach and contact one another in an orientation such that the tip of one prism binds at the midpoint of the other prism's edge. The prisms then rotate into an edge-to-edge orientation in which the two edges are offset from each other by $L/2$. Scale bars are 100 μm. Reprinted from [109] with permission. 111

4.14 Comparison of experimentally observed and simulated trajectories for a pair of triangular prisms of the same polarity. Top row: observed r vs. $t_c - t$ curves in log-log scale (left) and linear scale (inset), where t_c is taken to be the first frame in which the two prisms touch in each event; and observed θ_1, θ_2 vs $t - t_c$ curves (right). Four events are shown as explained in the legend, and lines showing $\beta = 1/8$ (consistent with hexapolar interaction) and 1/6 (consistent with quadrupolar interaction) are added. Illustrations of the prism configurations are added in the θ_1, θ_2 plot to show the geometry. Configurations at the time of contact ($t = t_c$) are pointed to by arrows, and the points at $t - t_c > 0$ show prism rotations after contact, with final configurations marked by circles. Bottom row: counterparts of the r and θ_1, θ_2 plots from simulation. Instead of contact time, t_m is the time where the separation distance reaches $r_m = 132\,\mu$m (the lower bound of r in our computation), at which the prisms touch if $\theta_1 = \theta_2 = 0$. We have chosen initial conditions that are close to two experimental trajectories. 112

4.15 Comparison of experimentally observed and simulated trajectories for a pair of triangular prisms of opposite polarities. Top row: experimental observations. Bottom row: simulation results. All conventions are the same as in Fig. 4.14. Note that in two experimental events, the prisms approach faster in the far-field regime than quadrupolar interactions would dictate, which we believe to be due to some accidental drift of the interface. 113

4.16 Configuration trajectories for three representative initial conditions (close to (a),(b) tip-to-tip, (c),(d) tip-to-edge, and (e),(f) edge-to-edge) and two different viscous-damping coefficient ratios. The top row shows the separation distance as a function of simulation time, with insets plotting separation distance values as a function of time-to-contact on a log scale. The gray reference line corresponds to the theoretical case of two ideal hexapoles approaching each other in a mirror-symmetric configuration. The bottom row shows the orientation angles of the triangular prisms as a function of simulation time. 114

4.17 "Phase" diagrams illustrating the final configurations ($r = 132\,\mu$m) for all possible initial orientations for two bowed-up triangular prisms at $r = 264\,\mu$m for two different viscous-damping coefficient ratios, (a) $\eta_{\tilde{\theta}}/\eta_r = 1.46$ and (b) $\eta_{\tilde{\theta}}/\eta_r = 0.146$. The final configurations are all mirror-symmetric and lie somewhere along the line in (c), with blue corresponding to tip-to-tip final configurations, red corresponding to side-to-side final configurations, and gray denoting initial conditions that lead to trapped configurations which are due to artificial kinks in the computed pair potential. (d) Capillary interaction potential values for mirror-symmetric configurations with two tips of the triangular prisms remaining in contact (thus, the separation distance, r, decreases below $132\,\mu$m as $\theta_1 = \theta_2$ increases. The potential indicates a tendency for tip-to-tip configurations to ultimately collapse to side-to-side configurations. 115

4.18 "Phase" diagrams illustrating the final configurations ($r = 132\,\mu$m) for all possible initial orientations for one bowed-up and one bowed-down triangular prism at $r = 264\,\mu$m for two different viscous-damping coefficient ratios, (a) $\eta_{\tilde{\theta}}/\eta_r = 1.46$ and (b) $\eta_{\tilde{\theta}}/\eta_r = 0.146$. The final configurations lie somewhere along the curve in (c), with blue corresponding to tip-to-edge final configurations and red corresponding to offset-edge-to-edge final configurations. 116

LIST OF APPENDICES

A. Deriving the effective force for an extensible rod 124

B. The kagome lattice dynamical matrix 130

C. Deriving the three-band effective dynamical matrix 133

ABSTRACT

Critical mechanical structures are structures on the verge of mechanical instability. Mechanical instability governs many fascinating phenomena in nature, including jamming, rigidity percolation, glass transitions, and structural phase transitions. Close to mechanical instability, the mechanical response and properties of these critical structures are dominated by the emergence of floppy modes, which are structural deformations that cost very little elastic energy. Although mechanical instability in athermal systems is well understood, how thermal fluctuations interact with floppy modes to modify transitions associated with the point of instability remains largely unexplored. To this end, we study the effect of thermal fluctuations on the phase transitions of various critical mechanical systems.

The first project presented in this dissertation concerns the buckling of rods at finite temperature. Thermal fluctuations can play an important role in the buckling of elastic objects at small scales, such as polymers or nanotubes. We study the finite-temperature buckling transition of an extensible rod by analyzing fluctuation corrections to the elasticity of the rod. We find that, in both two and three dimensions, thermal fluctuations delay the buckling transition, and near the transition, there is a critical regime in which fluctuations are prominent and make a contribution to the effective force that is of the order of the square root of the temperature. We verify our theoretical prediction of the phase diagram with Monte Carlo simulations.

The second project discussed in this dissertation examines how thermal fluctuations change structural transitions in lattices. We present an analytic study of the finite-temperature structural transition for the kagome lattice. Our model exhibits a zero-temperature contin-

uous twisted-untwisted transition as the sign of the next-nearest-neighbor spring constant changes. At finite temperature, we show that the divergent contribution of floppy modes to the vibrational entropy renormalizes this spring constant, resulting in a first-order transition.

Another expanding area of research is the self-assembly of open structures and mechanical metamaterials with novel properties at small scales. In large part to floppy modes, these intriguing properties include negative Poisson's ratio and tunable topological mechanical properties. Employing self-assembly allows for the expedient synthesis of such structures. To this end, we study different techniques currently used in self-assembly. We propose an experimental manifestation of the twisted kagome lattice via self-assembling tri-block Janus particles with offset attractive patches. We also characterize the twisted-untwisted phase transition that these particles can undergo. This may lead to a novel smart material with, for instance, a Poisson's ratio that is tunable between positive and negative values.

The third project discussed in this dissertation explores the self-assembly of open structures using triangular prisms on an air-water interface. We present our theoretical and numerical analysis of how capillary interactions between these prisms, mediated by the deformation of the interface around the prisms, lead to directional binding and the self-assembly of large-scale open structures. We show how particle bowing and contact-line pinning yields a capillary hexapole-like interaction that results in two sets of distinct, highly-directional binding events: tip-to-tip and tip-to-edge-midpoint. We analyze the collapse of these binding events to edge-sharing configurations that impede the formation of ordered, open structures such as the kagome lattice, and we briefly discuss design principles that can be used to stabilize such interactions.

CHAPTER I

Introduction

1.1 Critical mechanical structures and mechanical instability

Critical mechanical structures are structures that are close to mechanical instability. Of course, the subject of mechanical instability has always been an area of great interest, as we specifically engineer large-scale structures to be stable and resistant to failure – understanding the potential areas of weakness and sources of instability is, naturally, a matter of safety. It is not always the case, however, that mechanical instability is a property simply to be avoided. In expediently-engineered systems, especially at small scales, mechanical instability is indeed a property that can be exploited for various practical purposes. This is due to that fact that in critical mechanical structures – that is, near mechanical instability – a small number of "floppy modes", which are modes of deformation in the structure that cost very little energy (in fact, theoretically, there exist deformation modes that cost *no* energy, but in real systems, there is always a finite energy cost, albeit quite small), arise. Because the floppy modes cost such little energy, they are oftentimes the modes of deformation that significantly determine a material's response and, correspondingly, its properties.

For instance, there is a burgeoning interest in so-called "mechanical metamaterials", which are materials that derive their novel mechanical properties from their structure rather

than their chemical composition. Examples of these novel properties include negative Poisson's ratio, negative compressibility, negative thermal expansion, reprogrammability, and transformability, and it is precisely the specific structure of the material and the consequent existence of floppy modes that enable them [1–7]. The study of floppy modes and deformation mechanisms is also important in a biological context, such as in disordered networks of biopolymers (as can be found in the extracellular matrix, for instance), which are soft against small deformations but stiff against large ones due to the fact that initial deformation modes are floppy, involving only bending of the polymers, rather than energetically-costly stretching of the polymers [8, 9].

At small scales, as well, systems are being fabricated that utilize these minimal-energy mechanisms [10, 11]. At the colloidal and nano scales, however, thermal fluctuations are an important consideration, and it becomes crucial to understand the effect of thermal fluctuations on these systems and their inherent floppy modes. In some cases, the interplay between floppy modes and thermal fluctuations produces intriguing properties, such as "order-by-disorder", a phenomenon in which thermal fluctuations induce entropic splitting of energetically-degenerate ground states [12, 13] – though one can imagine how the destruction of such a degeneracy could also potentially interfere with the engineered exploitation of mechanisms in systems. Another interesting phenomenon arising from finite temperature effects is that of negative thermal expansion [14]. Normally, we expect positive thermal expansion when a sample is heated, but in open structures with transverse phonon floppy modes – such as in the example of $Sc_{1-x}Ti_xF_3$ [15], which has a cubic arrangement of corner-sharing octahedra that can twist – the fluctuations cause, on average, the volume of the unit cell to decrease as temperature increases, resulting in negative thermal expansion. Clearly, it is important to study the effect of thermal fluctuations on a variety of systems with floppy modes.

Finally, critical mechanical structures are frequently open structures, meaning that, once assembled, the packing fraction of their constituent components is far less than the maximal

packing fraction achieved by close-packing. This manifests itself in the form of open spaces and voids in between the components that make up the structure. Due to this openness, certain deformation and floppy modes are accessible to the structure that would not have been otherwise, if it were close-packed. A pathway towards efficient realization of open structures on small scales that does not require manual construction is self-assembly, which is the automated assembly of components into a larger organized structure. As we will discuss in this dissertation, there are various promising methods of self-assembly that enable the synthesis of open, critical structures with interesting mechanical properties.

1.1.1 The Maxwell counting rule

We begin our discussion of critical mechanical structures by characterizing instability and floppy modes in a mathematical way. In 1864, James C. Maxwell completed his seminal work [16] in structural rigidity theory, in which he formulated the conditions necessary for the mechanical stability of a frame, or truss. For a frame – a collection of points connected by rigid lines, or struts – to be stiff, such that attempting to alter the distance between any two points in the frame would require changing the length of at least one connecting line, Maxwell determined that each nominal degree of freedom in the frame would need to be stabilized by a constraint. In the context of a lattice with N sites and N_b central-force bonds embedded in d dimensions, this can be expressed as the equation

$$N_0 = N_{\text{d.o.f.}} - N_b, \tag{1.1.1}$$

where N_0 is the number of zero modes, which correspond to deformations of the system that cost no elastic energy, and $N_{\text{d.o.f.}} = dN$ is the number of degrees of freedom of the system, given no constraints; each bond is a constraint that removes one degree of freedom. Out of the N_0 zero modes, $f(d) = d(d+1)/2$ are trivial rigid translations and rotations of the entire lattice with free boundary conditions; for a lattice with periodic boundary conditions, which

is the case we will be primarily concerned with, $f(d) = d$ – only the rigid translations remain as trivial zero modes. The number of zero modes that correspond to actual deformations of the lattice, then, is

$$M = N_0 - f(d) = N_{\text{d.o.f.}} - N_b - f(d). \tag{1.1.2}$$

These remaining modes are called floppy modes or mechanisms. For a lattice to be stiff, or rigid, there cannot be any floppy modes – $M = 0$; all lattice deformations must cost finite energy. Therefore, the condition on the number of constraints in order for the lattice to be rigid is

$$N_b = dN - f(d). \tag{1.1.3}$$

It is common to re-express this condition in terms of a critical coordination number z_c, where $z = 2N_b/N$ is the number of neighbors that a given site is connected to via bonds (for a disordered system where each constituent particle has a varying number of neighbors, the mean coordination number $\langle z \rangle$ is used instead). In this case,

$$z_c = 2d - 2\frac{f(d)}{N} \approx 2d, \tag{1.1.4}$$

where the approximation becomes exact in the limit that $N \to \infty$. Thus, a large system with a coordination number of $z = 2d$ is marginally stable or rigid. For $z > 2d$, the system is over-constrained and there are no floppy modes, whereas for $z < 2d$, the system is completely floppy.

The above Maxwell rule is not completely general, as it does not account for the fact that constraints can be redundant [17] – placed in such a way to not increase rigidity – which allows for stresses to be distributed among the bonds in such a way as to not yield any net forces on the particles. This is known as a state of self stress. The generalized version of the counting rule, which can be rigorously proven as an index theorem [18], is

$$M = dN - N_b + N_s - f(d), \tag{1.1.5}$$

where N_s is the number of states of self stress. For a system with no redundant bonds, $N_s = 0$, and we recover the analysis of above. In a lattice that has a finite number of states of self stress ($N_s > f(d)$), however, even for a lattice with $N_b = dN - f(d)$ constraints (or, in the large lattice limit, $z = z_c = 2d$), there will exist floppy modes. A lattice where $z = z_c$, such that $N_s = N_0$, is called a *Maxwell lattice*, and the point $z = z_c$ is called the *Maxwell critical point*.

There are two types of floppy modes: "finite" floppy modes that are associated with finite displacements of sites that do not stretch any bonds, and "infinitesimal" ones that are associated with small displacements of sites that do not change the length of any bonds to first order in displacements. Small motions that are transverse to the initial direction of the bond correspond to infinitesimal floppy modes: for a small displacement δx, the change in the length of the bond (which we take to initially have length 1) is

$$\delta l = \sqrt{1 + (\delta x)^2} - 1 \approx \frac{(\delta x)^2}{2} = 0 + \mathcal{O}((\delta x)^2). \tag{1.1.6}$$

Whereas finite floppy modes are possible when considering a finite lattice with free boundary conditions, only infinitesimal floppy modes are available to a periodic Maxwell lattice with periodic boundary conditions.

Let us consider a couple of simple illustrative examples of the Maxwell counting rule. The first is a two-square frame consisting of bonds connecting $N = 6$ sites. When the frame contains $N_b = 7$ bonds positioned as shown in Fig. 1.1(a), it has $N_0 = 2 \times 6 - 7 = 5$ zero modes and $M = 5 - 3 = 2$ floppy modes, one for each square plaquette. When an extra diagonal bond is placed in the left square (Fig. 1.1(b)), it becomes rigid ($N_0 = 2 \times 4 - 5 = 3$ and $M = 3 - 3 = 0$), while the right square remains floppy; the entire frame has only that one floppy mode: $M = 2 \times 6 - 8 - 3 = 1$. With diagonal bonds placed in both square plaquettes (Fig. 1.1(c)), the entire frame becomes rigid. In the three preceding cases, there are no redundant bonds, and, therefore, the simple Maxwell count (without needing to consider

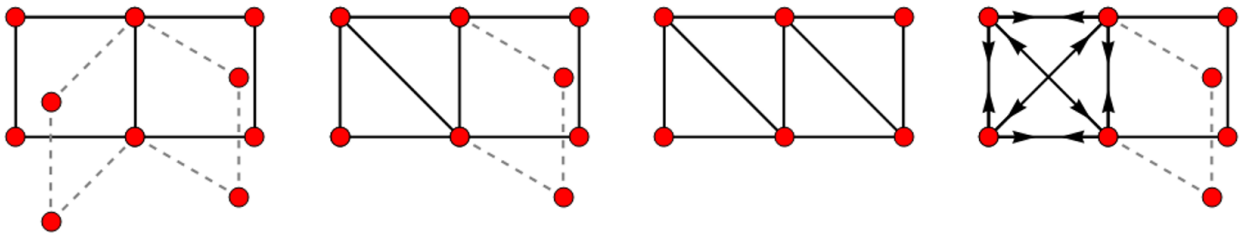

Figure 1.1: Two-square frames consisting of bonds connecting $N = 6$ sites. (a) has 7 bonds and two floppy modes, as indicated by the dashed bonds, (b) has 8 bonds and one floppy mode, and (c) has 9 bonds and no floppy modes – it is entirely rigid. Note that, in these cases, each addition of a bond has removed one floppy mode. (d) also has 9 bonds, but the extra bond has been redundantly placed in the left square plaquette, creating a state of self stress, as indicated by the arrows on the bonds. Therefore, according to the generalized Maxwell counting rule, there is still one floppy mode, corresponding to the right square plaquette.

states of self stress) suffices. If, however, the final diagonal bond is also placed in the left square (Fig. 1.1(d)), the right square becomes floppy even though the number of bonds in the frame is the same as in the previous case. This is because the outer bonds of the left square can be placed under tension (compression) and the inner diagonal bonds under compression (tension) with magnitudes such that the net forces on all sites are zero – hence, the frame has a state of self stress, and $N_s = 1$. Then, according to Eq. (1.1.5), $M = 2 \times 6 - 9 + 1 - 3 = 1$.

A second example, of particular relevance to the study of lattices, as we will see, is a set of sites connected by a straight line of parallel bonds under periodic boundary conditions. A state of self stress exists in this configuration: there are no forces on any of the sites when all the bonds are under either equal tension or equal compression. This state of self stress and, consequently, the extra floppy mode, are removed when the straight line is eliminated by, for instance, changing the bonds to a "zigzagged" configuration. Thus, in a lattice, there is one additional floppy mode for each straight line of bonds, and that floppy mode is removed by any modification of the lattice that eliminates those straight lines.

Maxwell's counting analysis has been applied to a number of systems, including rigidity percolation [19–22], jamming of packed spheres [23–26], biopolymer networks [9, 27, 28], and

beyond. For instance, let us consider rigidity percolation, which describes the transition of a system to (from) a rigid state with the addition (dilution) of bonds, in a two-dimensional central-force triangular lattice. If all bonds are present, the coordination number is $\langle z \rangle = 6 > 2d = 4$. As expected, this lattice is completely rigid. If we retain bonds with a probability p, however, the lattice is diluted, and the average coordination number becomes $\langle z \rangle = 6p$. For a sufficiently large value of p, the lattice should become floppy. Mean field as well as numerical analyses have shown that this occurs at the critical value $p_c \approx 2/3$, which is precisely the value that is predicted by Maxwell counting, since, in this case, $\langle z \rangle = 4$, the Maxwell critical point for two-dimensional systems.

Granular matter, which consist of particles that interact repulsively only when touching and are of macroscopic scale so that thermal fluctuations are negligible, is one of a class of disordered materials that undergo a jamming transition as the packing fraction, ϕ, of the system is increased. Granular materials can be approximately modeled as frictionless disks or spheres[1] in two or three dimensions, respectively, which interact via finite-range repulsive pair potentials as governed by their diameters. For small packing fractions, the particles are free to flow in response to any applied stresses without overlapping with each other, and the systems behaves as a fluid. Above a critical density, ϕ_J, which occurs at the so-called Point J, each particle (aside from a small number of rattlers) is held in mechanically-stable equilibrium positions by its neighbors, and the system becomes jammed – it is able to withstand small stresses without deforming irreversibly. This jamming transition can be characterized by the order parameter $\langle z \rangle$. Below the critical point, there are no overlaps, and $\langle z \rangle = 0$. Numerical simulations have shown that at the critical point, the coordination number jumps discontinuously from 0 to $z_c = 2d$, in accordance with Maxwell counting, and

[1]Note that this is merely an approximation. At macroscopic scales, in particular, granular materials are frictional, though on colloidal scales, the frictionless approximation is valid. Granular materials have also been studied using *frictional* constituents, which leads to interesting phenomena such as shear jamming [29] at lower packing fractions than the critical value ϕ_J we discuss here.

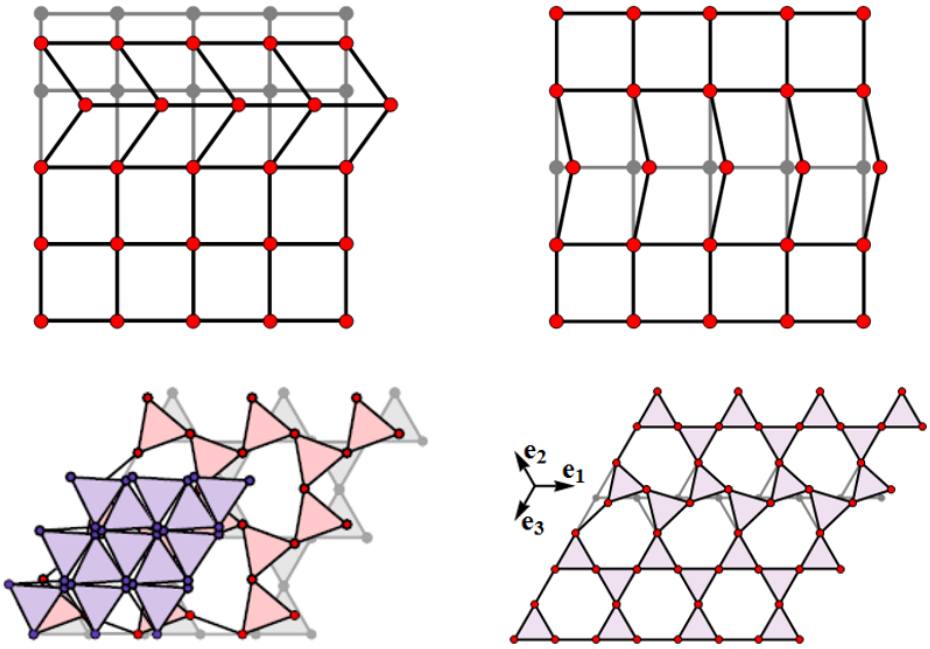

Figure 1.2: Examples of floppy modes for two-dimensional critical lattices. The left column corresponds to finite floppy modes in the (top) nearest neighbor (NN) square lattice and the (bottom) NN kagome lattice. In particular, the floppy mode for the NN kagome lattice is the uniform twisting mode that we will be considering further. Both of these deformations cost no energy as they do not change the length of the NN bonds. These finite floppy modes only apply under free boundary conditions. The right column corresponds to infinitesimal floppy modes. These floppy modes exist even under periodic boundary conditions. Note that the include of next-nearest-neighbor (NNN) bonds would gap these modes, as they would change the length of the NNN bonds.

that above the critical packing fraction,

$$\Delta z \equiv \langle z \rangle - z_c \sim (\Delta\phi)^{1/2}, \tag{1.1.7}$$

where $\Delta\phi \equiv \phi - \phi_J$ [30–32].

1.1.2 Examples of critical lattices

In this section, we introduce three simple two-dimensional periodic lattices that, when only consisting of sites joined by nearest-neighbor bonds, are Maxwell lattices, with $z = 2d = 4$.

1.1.2.1 The square lattice

The nearest-neighbor square lattice has a unit cell consisting of a single site with $z = 4$ neighbors; therefore, it has a phonon spectrum that consists only of 2 acoustic phonon bands and no optical phonon bands. Because the square lattice contains straight lines in orthogonal directions, each line is a state of self stress for a periodic lattice: $N_s = N_x + N_y$, where there are N_x (N_y) sites in the x (y) direction. Therefore, since the nearest-neighbor (NN) square lattice is a Maxwell lattice, there are also $N_0 = N_x + N_y$ zero modes, where the trivial zero modes are associated with $\mathbf{q} = 0$ and are states of infinitesimal uniform shear, and the non-trivial zero modes are infinitesimal floppy modes in which any row or column is rigidly displaced (Fig. 1.2). These zero modes lie along the q_x and q_y axes of the first Brillouin Zone (1BZ), from one edge to the other. When next-nearest-neighbor bonds are added in, all floppy modes are removed, and the phonon spectrum becomes gapped everywhere except at $\mathbf{q} = 0$.

1.1.2.2 The kagome lattice

The nearest-neighbor kagome lattice has a unit cell consisting of three sites, each with $z = 4$ neighbors; therefore, it has a phonon spectrum that consists of 2 acoustic phonon bands and 4 optical phonon bands. The kagome lattice contains straight lines along three symmetry directions; taking $N_x = N_y$ for simplicity, we can determine that there should be $3N_x$ states of self stress along the symmetry directions and, consequently, the same number of zero modes along those same lines. Just as above, each non-trivial zero mode is an infinitesimal floppy mode corresponding to microrotations of triangles along the corresponding straight line (Fig. 1.2). Adding next-nearest-neighbor (NNN) bonds gaps the lowest mode and all other modes except for the two zero modes remaining at $\mathbf{q} = 0$.

1.1.2.3 The twisted kagome lattice

The twisted kagome lattice is constructed from the kagome lattice by rotating all the upward-facing triangles uniformly by a twisting angle α, which corresponds to the zero mode at point Γ (Fig. 1.2). In this case, the straight lines of the untwisted kagome lattice become zigzagged and, therefore, unable to sustain any states of self stress. This leaves only the two $\mathbf{q} = 0$ states of self stress so that the lines of floppy modes of the untwisted kagome lattice have been lifted without the need for NNN bonds. The finite nearest-neighbor twisted kagome lattice is uniformly compressed by a factor of $\cos\alpha$ in each direction – the volume of the unit cell is equal to $2\sqrt{3}a^2\cos^2\alpha$ for NN bonds fixed at length a. Since the volume of the NN lattice can change without changing the length of any NN bonds – and, hence, without any energy cost – the bulk modulus $B = 0$ for the twisted kagome lattice. Furthermore, it contract isotropically: any contraction undergone in one direction will also be undergone in the orthogonal direction. This corresponds to the property of being auxetic, or having a negative Poisson's ratio. This, coupled with the fact that $B = 0$, means that the twisted kagome lattice is *maximally auxetic* – it has a Poisson's ratio of -1. Adding NNN bonds stabilizes the lattice, yielding a finite bulk modulus.

1.2 Self-assembly of open structures

Self-assembly is a process by which constituent components of a system autonomously organize into ordered patterns or structures due to the nature of interactions among the components, obviating the need for tedious and difficult top-down manipulation [33, 34]. Self-assembly is ubiquitous in nature: all biological entities, from cell membranes and individual cells to supremely complex multicellular life are indeed self-assembled. In non-biological contexts, self-assembly has been implemented with building blocks on various scales, including atoms, molecules, macromolecules, and colloidal particles, and there is a growing focus on the role of shape and interaction anisotropy in creating novel structures [35, 36].

We will focus on so-called static self-assembly, in which the final structure is a global or local equilibrium state. Frequently, self-assembly is a purely spontaneous process in which the associated change in free energy is negative throughout – though it is possible that self-assembly may require overcoming an initial energy barrier. In some instances, the spontaneous self-assembly process is driven by a decrease in energy (such as with capillary interactions, as we will discuss); in many others, the process is due to an increase in entropy. In the latter case, it may seem counterintuitive that the entropy of the system has increased since most self-assembled structures are more "ordered" than the initial "disordered" mixture of the individual components. However, as in the cases of the isotropic to nematic transition of thin rods as well as in the crystallization of hard spheres, we observe that the loss of orientational or positional entropy due to ordering is more than compensated by the increase in translational entropy due to an increase in available space per particle [37].

The simplest primary building block that can be used in self-assembly are isotropic spherical colloids. Using these constituents yielded ordered structures with simple symmetries and high packing fractions, such as face-centered cubic, hexagonal close-packed, and body-centered cubic. Over the past decade, however, there have been significant advances made in particle synthesis that have led to a variety of anisotropic particles, both in shape and chemical heterogeneity. Some examples include cubes, triangles, tetrahedra, rods, and stars, as well as Janus and patchy particles of various shapes [36]. These anisotropies can produce highly-tuned and directional particle interactions that lead to the formation of specific desired structures with novel properties.

One particular aim of this directed self-assembly with anisotropic particles is the formation of open structures, which consist of ordered arrangements of their constituents that result in low packing fractions and open spaces between them. The openness of the structure enables fluctuations and deformations that are not accessible to close-packed structures. Open structures are known to exist in nature and have also been artificially engineered; they exhibit a fascinating array of properties, such as negative Poisson's ratio, negative ther-

mal expansion, and tunable topological mechanical properties, that typically do not occur in more conventional materials. In connection with our discussion on lattices, the kagome family of lattices consists of open lattices that share many of these unique material aspects.

Necessarily, open structures have low coordination numbers and, therefore, are close to the point of mechanical instability. Consequently, the constituent components must be designed in such a way that ensure stabilized directional bonding, such that the open structures do not collapse into close-packed assemblies. In the remainder of this section, we will introduce two different techniques, with differing constituent components, that can be used to self-assemble stable open structures, which we will expound upon in Chapters III and IV.

1.2.1 Janus particles

Janus particles are named after the two-faced Roman god Janus, as they both share the characteristic of having two distinct and opposing faces [38]. Janus particles are nano- and micro-scale colloidal particles with differing surface chemical compositions on their two sides. Even without considering self-assembly, this anisotropy has interesting applications: for instance, micron-sized spherical polysterene beads with a thin layer of platinum deposited on one hemisphere placed in an aqueous hydrogen peroxide solution display monodirectional self-propelled "swimming" trajectories [39], and biocompatible Janus polymeric nanoparticles can carry both a hydrophobic drug and a hydrophilic drug in a single particle, allowing for the effective delivery of two drugs with disparate solubility [40]. Janus particles can also be fabricated in a variety of shapes, including spheres, ellipsoids, and cylinders, and disks, with the functionalization axis either horizontal or vertical [41].

The asymmetric, directional interaction between Janus particles has been shown to induce self-assembly of the particles into clusters [42], staggered one-dimensional chains and two-dimensional crystals in an AC electric field [43], and, theoretically, a rich variety of close-packed crystalline phases for varying finite external pressure [44]. There is also another interesting application of Janus particles in the form of ellipsoids that relates to the idea of mecha-

nisms in mechanical metamaterials: they are found to self-assemble into orientationally- and positionally-ordered finite-length one-dimensional fibers that can be reversibly elongated and contracted through a sliding mechanism under the presence of an AC electric field [10].

In all of these examples thus far, the constituent components of self-assembly have been diblock Janus particles, and all resultant assemblies have involved clustering or close-packing. Recently, the use of triblock Janus particles, consisting of two hydrophobic attractive patches on either end and a charged band in the middle, lying in an aqueous salt solution, which screens the electrostatic repulsion, allowing for self-assembly by the short-range attractive hydrophobic interaction, has been found to spontaneously self-assembly into a large-scale two-dimensional kagome lattice [45, 46]. We will explore this further in Chapter III and discuss how the triblock Janus particle can be modified to allow for the self-assembly of the twisted kagome lattice.

1.2.2 Capillary interactions

A particle adsorbed to an interface between two immiscible fluids deforms the interface around itself by imposing a boundary condition on the height of the interface at the three-phase contact line, where the interface between the two fluids meets the particle surface. The deformation of the interface away from its equilibrium state (for the case of no background curvature, this is a flat interface) creates excess interfacial surface area. Since interfacial energy is directly proportional to its area, where the proportionality constant is the surface tension, this corresponds to excess interfacial energy. If there is a second particle in the vicinity of the first particle, the nature of the resultant interface-mediated capillary force between the two particles – that is, whether it is attractive or repulsive – is determined entirely by whether the excess area decreases (attractive) or increases (repulsive). For two millimeter-scaled particles with circular horizontal cross-sections, the interface will deform non-negligibly and isotropically (this is what will later be termed as a monopole term) due to gravitational forces; therefore, the interface deformation is in the same direction for both

particles so that the particles will want to move toward each other in order to minimize the excess interfacial area. If there are numerous particles, they will attract one another and ultimately clump together into an ordered, close-packed structure. The phenomenon is surely familiar to many – it is known as the "Cheerios" effect, as individual Cheerios floating on milk tend to clump together after some time.

For micron-scaled particles, however, gravitational effects are typically negligible and, thus, there should seemingly be no interface deformation and resultant capillary assembly. Interestingly, however, it has been observed in experimental systems that interface deformations in the form of undulations around the contact line do in fact occur due to anisotropic particle shape, surface roughness, and chemical inhomogeneity. The effect of this is that, for a given particle anisotropy, there will be regions around the particle where the interface deforms upwards – which we will consider to be a positive capillary charge – and other regions where the interface deforms downwards – a negative capillary charge (of course, the entirety of the deformation occurs in such a way that the particle remains in mechanical equilibrium). Particles will attract one another when they are oriented such that like capillary charges are pointing towards each other, and will repel one another when unlike charges are lined up instead. Furthermore, the capillary interaction is strongest where the deformation is most significant. In the case of a cylindrical particle with a small radius-to-length aspect ratio lying with its long axis parallel to the interface, the interface necessarily deforms much more at the ends than along the sides of the cylinder in order to satisfy mechanical equilibrium; therefore, end-to-end assembly is much more favorable than side-to-side assembly in a system of these cylindrical particles.

Thus, for a system of particles with undulating contact lines, the particles will assume energetically-favorable relative orientations and inter-particle distances to minimize the excess interfacial surface area. By expediently selecting specific particle shapes and associated design parameters, capillary interactions can be utilized to promote self-assembly of these particles into extended regular open structures, as desired. In particular, thin polygons such

as triangles are well-suited for the self-assembly of open lattices if the anisotropic interactions can be biased to favor tip-to-tip capillary interactions over side-to-side (or tip-to-side) interactions, since the latter would result in a close-packed structure.

1.3 Organization of the dissertation

There are two general questions that have motivated the various works contained in this dissertation. First, what is the effect of thermal fluctuations on critical mechanical structures and mechanical instability? And second, how can we employ various self-assembly techniques to create mechanical metamaterials with novel properties. Both of these are rather large in their scope, and will require significant study by a number of researchers from many different facets and viewpoints, but we have attempted to add to the general understanding of these concepts for some specific systems.

In Chapter II, based on [47], we study the finite-temperature buckling transition of an extensible rod by analyzing fluctuation corrections to the elasticity of the rod using a continuum model. We find that, in both two and three dimensions, thermal fluctuations delay the buckling transition. We also verify our theoretical prediction of the phase diagram with Monte Carlo simulations using a discrete model for the rod.

In Chapter III, we present an analytic study of the finite-temperature rigidity transition for the kagome lattice. Our model exhibits a zero temperature continuous twisted-untwisted transition as the sign of the next-nearest-neighbor spring constant changes. At finite temperature, we show that the divergent contribution of floppy modes to the vibrational entropy renormalizes this spring constant, resulting in a first-order transition. We also propose an experimental manifestation of such open lattices and the associated transition in the system of self-assembling tri-block Janus particles.

In Chapter IV, we present the experimental findings, from our collaborators Joseph Ferrar and Michael Solomon, of capillary-driven binding between thin, equilateral triangular

microprisms adsorbed to a flat air-water interface, where physical bowing of the prisms is observed, leading to tip-to-tip or tip-to-side-midpoint binding events dependent on the relative bowing polarities of the prisms. We present the results of numerical simulations of these triangular particles at an interface, including individually and in pairs. We show how particle bowing can yield two distinct binding events and connect it to theory in terms of a capillary multipole expansion. Finally, we use our numerical simulation results to compute dilute-binding trajectories and compare them to experiment.

Finally, in Chapter V, we summarize the work in this dissertation and discuss relevant future research directions.

CHAPTER II

Finite-temperature buckling of an extensible rod

2.1 Introduction

When a thin elastic rod is under compression on its two ends, it experiences an instability towards buckling as the compression exceeds a critical value; this is the classical Euler buckling problem [48, 49]. This critical compression is determined by the competition between the compression and bending energy costs of the rod. The buckling instability plays an important role in many problems in fields ranging from physics to engineering and biology [27, 50–54].

More recently, experimental studies on buckling phenomena at small length scales, such as the buckling of stiff or semiflexible polymers, nano-filaments, and nanotubes, have been enabled by advances in various technologies [55–59]. These studies may lead to novel devices that utilize transitions between multiple mechanical ground states. At these small scales, it is necessary to include effects of thermal fluctuations, which have been shown to lead to interesting phenomena near mechanical instabilities in various systems [13, 46, 60–64]. Such thermal-fluctuation effects have been theoretically investigated, and phenomena such as corrections to the projected end-to-end length, shifts in the critical compression, and

softening of the buckling transition have been discovered [65–72]. However, most of these theoretical studies on how fluctuations renormalize the buckling transition have focused on the case of inextensible polymers and have employed the worm-like chain model, which assumes that the polymer has a *constant contour length*. This is an idealized limit where the rod cannot be stretched or compressed. For real rods, although the resistance against stretching is much stronger than that against bending, it is worthwhile to discuss whether the extensibility of the rod changes what is known about buckling at finite temperature.

In this chapter, we investigate finite-temperature buckling using a model elastic energy that allows for rod extensions. In this model, the end-to-end distance is the control parameter (fixed-strain ensemble), and the rod is allowed to have transverse fluctuations, which both stretch/compress and bend the rod. By integrating out higher-momentum modes which couple to the first fundamental mode through anharmonic terms, we calculate fluctuation corrections to the rigidity and analyze the buckling transition of the renormalized theory. We find that, in both two and three dimensions, thermal fluctuations shift the buckling transition to larger-magnitude values of compression. Our Monte Carlo simulations verify the analytic phase diagram we obtain (Fig. 2.1). In addition, we also analytically calculate the effective force of the rod, showing that, close to the buckling transition, thermal fluctuations are prominent and contribute an $O(\sqrt{T})$ correction to the effective force.

It is worth pointing out that, in the presence of thermal fluctuations, the rod is never completely "straight." The physical meaning of having a "straight-buckled" transition is that the mean-square transverse fluctuations of the rod (e.g., the mean-square transverse displacement of the midpoint of the rod) change from zero in the straight phase to a nonzero value in the buckled phase. In other words, the elastic free energy minimum of the rod changes from the straight configuration to the buckled configurations.

This chapter is organized as follows: we construct the model and discuss the analytic theory in Sec. 2.2 and present the Monte Carlo simulations in Sec. 2.3. Then, in Sec. 2.4, we summarize our results and discuss relations to other studies.

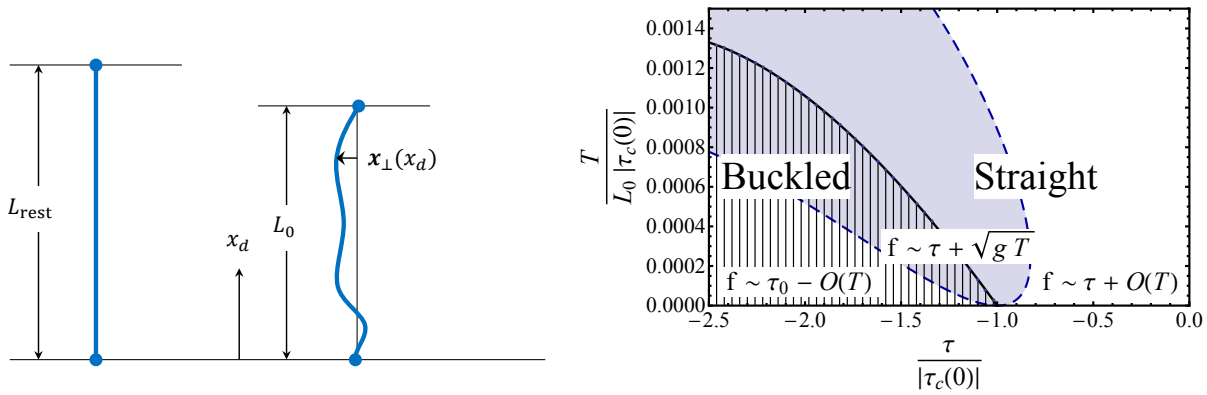

(a) (b)

Figure 2.1: (a) Illustration of an extensible rod under compression. (b) Predicted phase diagram for two-dimensional finite-temperature buckling of an extensible rod in the plane of normalized compression and temperature (as defined in Sec. 2.2). The thick black curve represents the phase boundary between the straight (unshaded) and the buckled (shaded with vertical lines) phases. The dashed curve denotes the boundary of the critical regime (light blue region) where the thermal-fluctuation correction to the effective force is of $O(\sqrt{T})$.

2.2 Model and analytic theory

2.2.1 The extensible-rod Hamiltonian with anharmonic terms

We consider a thin elastic rod with rest length L_{rest} embedded in d dimensions, as shown in Fig. 2.1a. Here, L_0 is the end-to-end distance, or projected length, of the rod, which is the control parameter of our theory, and L is the instantaneous contour length in the presence of thermal fluctuations.

Assuming that the rod is made of a homogeneous material with Young's modulus E, its stretching rigidity g and bending rigidity κ are given by

$$\begin{aligned} g &= \pi a^2 E / L_{\text{rest}}, \\ \kappa &= EI = (\pi/4) E a^4, \end{aligned} \tag{2.2.1}$$

where a is the radius of the rod, and I is the moment of inertia of the cross-section. Throughout this work, we require that the relative strengths of the (mechanical) rigidities against

bending and against stretching or compression of the rod satisfy

$$\frac{k_\perp}{k_\parallel} \propto \frac{\kappa}{gL_{\rm rest}^3} \propto \left(\frac{a}{L_{\rm rest}}\right)^2 \ll 1, \tag{2.2.2}$$

where $k_\perp$ and $k_\parallel$ are the corresponding longitudinal and transverse spring constants, respectively, meaning that it is much more energetically costly to stretch/compress the rod than it is to bend the rod. This is satisfied by most microscopic rod-like objects, including polymers, nanowires and nanotubes [71].

The instantaneous stretching and compression elastic energy of the rod can be written as

$$\begin{aligned} U_{sc} &= \frac{1}{2}g(L - L_{\rm rest})^2 \\ &= \frac{1}{2}g\big[(L - L_0) + (L_0 - L_{\rm rest})\big]^2. \end{aligned} \tag{2.2.3}$$

We define τ to be the force applied to the ends of the straight rod at $T = 0$, when there are no thermal fluctuations (i.e., $L = L_0$):

$$\tau \equiv g(L_0 - L_{\rm rest}), \tag{2.2.4}$$

so that $\tau > 0$ corresponds to stretching of the rod, while $\tau < 0$ corresponds to compression.

We proceed to derive the Hamiltonian of the rod for a given compression τ and an instantaneous fluctuation configuration, which is described by

$$\begin{aligned} &\mathbf{r}(x_d) = (x_1, \ldots, x_{d-1}, x_d) \equiv (\mathbf{x}_\perp, x_d), \\ &0 \le x_d \le L_0, \end{aligned} \tag{2.2.5}$$

where x_d parametrizes the rod using the projected end-to-end distance, $\mathbf{r}(x_d)$ is the position

of the rod at x_d, and $\mathbf{x}_\perp$ denotes the transverse displacement of the rod. We define derivatives

$$\boldsymbol{\pi}(x_d) \equiv \frac{d\mathbf{x}_\perp}{dx_d} = \left(\frac{dx_1}{dx_d}, \cdots, \frac{dx_{d-1}}{dx_d}\right), \tag{2.2.6}$$

where $\boldsymbol{\pi}$ is a one- (two-) dimensional vector for the case of a rod embedded in two (three) dimensions.

The change in the length of the rod due to thermal fluctuations can be expressed in terms of the $\boldsymbol{\pi}$ field as

$$L - L_0 = \int_0^{L_0} dx_d \ \left(\sqrt{1 + |\boldsymbol{\pi}|^2} - 1\right). \tag{2.2.7}$$

Using this, we can then write the stretching and compression elastic energy (2.2.3) as

$$U_{sc} = \frac{\tau^2}{2g} + \tau \int_0^{L_0} dx_d \ \left(\sqrt{1 + |\boldsymbol{\pi}|^2} - 1\right) + \frac{g}{2}\left[\int_0^{L_0} dx_d \ \left(\sqrt{1 + |\boldsymbol{\pi}|^2} - 1\right)\right]^2. \tag{2.2.8}$$

The bending energy of the rod is given by

$$U_b = \frac{\kappa}{2} \int_0^{L} ds \ |d_s \hat{\mathbf{t}}(s)|^2, \tag{2.2.9}$$

where s labels the arc length. We assume the bending rigidity to be homogeneous along the arc length, given that we are considering the regime where stretching is much more energetically costly than bending. Here, $\hat{\mathbf{t}}(s)$ is the unit tangent vector at s and $|d_s \hat{\mathbf{t}}(s)|$ is the local curvature. U_b can also be expressed in terms of $\boldsymbol{\pi}(x_d)$:

$$U_b = \frac{\kappa}{2} \int_0^{L_0} dx_d \ \left[\frac{|\boldsymbol{\pi}'|^2}{(1 + |\boldsymbol{\pi}|^2)^{3/2}} - \frac{(\boldsymbol{\pi} \cdot \boldsymbol{\pi}')^2}{(1 + |\boldsymbol{\pi}|^2)^{5/2}}\right], \tag{2.2.10}$$

where $\boldsymbol{\pi}'$ is shorthand for $d\boldsymbol{\pi}/dx_d$ and we used

$$\hat{\mathbf{t}}(x_d) = \frac{d\mathbf{r}(x_d)/dx_d}{|d\mathbf{r}(x_d)/dx_d|} = \frac{(\boldsymbol{\pi}(x_d), 1)}{\sqrt{1 + |\boldsymbol{\pi}(x_d)|^2}} \tag{2.2.11}$$

and

$$ds = \sqrt{1 + |\boldsymbol{\pi}|^2} dx_d. \tag{2.2.12}$$

The total Hamiltonian of the rod is a sum of both the stretching/compression and the bending contributions,

$$H = U_{sc} + U_b. \tag{2.2.13}$$

The Hamiltonian can then be written as a series expansion up to $O(\boldsymbol{\pi}^4)$,

$$H = H_0 + H_2 + H_4, \tag{2.2.14}$$

where

$$H_0 = \frac{\tau^2}{2g} \tag{2.2.15}$$

is the energy of the straight rod with no fluctuations ($L = L_0$),

$$H_2 = \frac{1}{2} \int_0^{L_0} dx_d \left(\tau |\boldsymbol{\pi}|^2 + \kappa |\boldsymbol{\pi}'|^2 \right) \tag{2.2.16}$$

contains terms quadratic in $\boldsymbol{\pi}$, and

$$H_4 = \frac{1}{2}\int_0^{L_0} dx_d \left[-\frac{\tau}{4}|\boldsymbol{\pi}|^4 - \frac{3\kappa}{2}|\boldsymbol{\pi}|^2|\boldsymbol{\pi}'|^2 - \kappa(\boldsymbol{\pi}\cdot\boldsymbol{\pi}')^2\right] + \frac{g}{8}\iint_0^{L_0} dx_d dx'_d\, |\boldsymbol{\pi}(x_d)|^2|\boldsymbol{\pi}(x'_d)|^2 \tag{2.2.17}$$

includes terms quartic in $\boldsymbol{\pi}$. Here $\boldsymbol{\pi}'$ is shorthand notation for $d\boldsymbol{\pi}/dx_d$. This Hamiltonian H includes contributions from both stretching and compression as well as bending of the rod. The last term in H_4, coming from $g(L-L_0)^2/2$, appears to be nonlocal; however, as we shall see, it simply leads to a $\boldsymbol{\pi}^4$ term in Fourier space with its momentum sum limited to a special channel.

Note that this formulation with fixed end-to-end distance is the same as the one used in the classical Euler buckling problem in textbooks [49]. A similar formulation has also been used in Refs. [67, 68], which focus on quantum aspects of buckling. Additionally, because we are interested in the case where the rod is much more resistant to stretching than it is to bending, the stretching can be taken to be small and highly homogeneous throughout the rod. This allows for the approximation to be made that the parameters κ and g are uniform along the rod, as in Ref. [73].

2.2.2 Classical ($T = 0$) Euler buckling

The $T = 0$ buckling transition is obtained by analyzing the stability of the quadratic coefficient of the Hamiltonian H, while the $T = 0$ configuration is determined by the location of the minimum of H. It is convenient to analyze this Hamiltonian in momentum space.

To obtain the Fourier transform of this Hamiltonian, we need to pay special attention to the specific boundary conditions of the problem. Here, $\boldsymbol{\pi}$ has to be a real-valued field, and $\mathbf{x}_\perp(x_d)$ (the perpendicular component of $\mathbf{r}$, as defined in Eq. 2.2.5) has to vanish at the two ends, $x_d = 0$ and $x_d = L_0$. This limits the Fourier series of $\mathbf{x}_\perp(x_d)$ to $\sin(n\pi x_d/L_0)$

basis functions, and the Fourier series of $\boldsymbol{\pi}(x_d)$ to $\cos(n\pi x_d/L_0)$ basis functions. In order to work with the more convenient basis of exponential functions, we necessarily extend the rod to $x_d \in [-L_0, L_0]$ to obtain periodic boundary conditions from the physical fixed boundary conditions and limit $\boldsymbol{\pi}(x_d)$ to be real-valued even functions on this interval (correspondingly, $\mathbf{x}_\perp(x_d)$ is limited to real-valued odd functions), so that the value of $\boldsymbol{\pi}(x_d)$ for $-L_0 < x_d < 0$ is determined by

$$\begin{aligned} \mathbf{x}_\perp(x_d) &= -\mathbf{x}_\perp(-x_d) \\ \boldsymbol{\pi}(x_d) &= \boldsymbol{\pi}(-x_d). \end{aligned} \tag{2.2.18}$$

Therefore, we can write the Fourier transform as

$$\boldsymbol{\pi}(x_d) = \frac{1}{2L_0} \sum_q \boldsymbol{\pi}_q e^{iqx_d}, \tag{2.2.19}$$

$$\boldsymbol{\pi}_q = \int_{-L_0}^{L_0} dx_d \, \boldsymbol{\pi}(x_d) e^{-iqx_d}, \tag{2.2.20}$$

with

$$q = \frac{n\pi}{L_0}, \;\; n \in \mathbb{Z} \setminus \{0\}. \tag{2.2.21}$$

Because $\boldsymbol{\pi}(x_d)$ is real and even, we have constraints on $\boldsymbol{\pi}_q$ that

$$\boldsymbol{\pi}_q = \boldsymbol{\pi}_{-q} = \boldsymbol{\pi}_q^*. \tag{2.2.22}$$

Therefore, positive and negative q values do not constitute independent modes.

The quadratic-order Hamiltonian, which is sufficient to ascertain the stability of the system, can then be written as

$$H_2 = \frac{1}{8L_0} \sum_q (\tau + \kappa q^2) \boldsymbol{\pi}_q^2, \tag{2.2.23}$$

where q is given by Eq. (2.2.21). To reiterate, although the sum seemingly counts excess modes by including both positive and negative values of q, these modes are not actually independent; the above sum is even in q, and the number of independent modes is the same as in the case of expanding H in terms of $\sin(n\pi x_d/L_0)$. It is straightforward to extract the $T = 0$ Euler buckling condition from this equation. The magnitude of the lowest allowed momentum mode is $q_1 = \pi/L_0$, since the $q = 0$ mode is excluded by the above fixed-end boundary conditions. In order for the Hamiltonian to have a stable equilibrium at $\boldsymbol{\pi}_q = \mathbf{0}$, its matrix representation must be positive definite – all its eigenvalues must be positive:

$$\tau + \kappa q^2 > 0 \ \ \forall q. \tag{2.2.24}$$

Applying this condition to the lowest mode, we obtain the critical compression

$$\tau_c(0) = -\kappa \frac{\pi^2}{L_0^2}, \tag{2.2.25}$$

where the 0 in parentheses indicates that this is a $T = 0$ result. Recall that $\tau < 0$ corresponds to compression of the rod, so that for any compression $\tau > \tau_c(0)$ (i.e., compression with a magnitude less than that of the critical value), the rod remains straight.

For $\tau < \tau_c(0)$, on the other hand, the harmonic-level Hamiltonian is no longer stable at $\boldsymbol{\pi} = \mathbf{0}$. The number of modes that have become unstable depends on the value of τ; for $(n+1)^2\tau_c(0) < \tau < n^2\tau_c(0)$, the first n modes are unstable, as each of their coefficients in H_2 is negative. Thus, for increasingly negative values of τ, it is possible to have various metastable states corresponding to higher orders of buckling; for any value of $\tau < \tau_c(0)$, however, the most energetically favorable buckled configuration is the $n = 1$ mode. In this chapter, we will only be concerned with analyzing the instability of the first momentum mode when considering the buckling transition; therefore, our discussion in the buckled phase will be restricted to the case of $4\tau_c(0) < \tau < \tau_c(0)$, since the second mode becomes unstable for $\tau < 4\tau_c(0)$. In this range of compression values, the new stable state – corresponding to the

$n = 1$ buckled phase – is fixed by the anharmonic terms in H_4 with only $\boldsymbol{\pi}_1$ nonzero.

The value of $\boldsymbol{\pi}_1$ is determined by minimizing the total Hamiltonian with both $\boldsymbol{\pi}^2$ and $\boldsymbol{\pi}^4$ terms. Taking $\boldsymbol{\pi}_q = \mathbf{0}$ for all but the first mode ($|q| = \pi/L_0$), the Hamiltonian becomes

$$H = H_0 + \frac{\tau - \tau_c(0)}{4L_0}|\boldsymbol{\pi}_1|^2 + \frac{-\frac{3}{2}\tau + 5\tau_c(0) + gL_0}{32L_0^3}|\boldsymbol{\pi}_1|^4. \tag{2.2.26}$$

The minimum-energy configuration is determined by

$$\left.\frac{\partial H}{\partial \boldsymbol{\pi}_1}\right|_{\hat{\boldsymbol{\pi}}_1} = 0, \tag{2.2.27}$$

where $\hat{\boldsymbol{\pi}}_1$ denotes the mode corresponding to this minimum-energy configuration. Thus, we find that

$$|\hat{\boldsymbol{\pi}}_1| = \sqrt{\frac{4L_0^2(\tau_c(0) - \tau)}{-\frac{3}{2}\tau + 5\tau_c(0) + gL_0}}. \tag{2.2.28}$$

Applying the limit of stretching stiffness much greater than bending stiffness [Eq. (2.2.2)] such that $gL_0 \gg |\tau_c(0)|, |\tau|$, we obtain

$$|\hat{\boldsymbol{\pi}}_1| = \sqrt{\frac{4L_0(\tau_c(0) - \tau)}{g}}. \tag{2.2.29}$$

This leads to the $T = 0$ equilibrium buckled configuration

$$|\hat{\mathbf{x}}_\perp(x_d)| = \frac{1}{\pi}\sqrt{\frac{4L_0(\tau_c(0) - \tau)}{g}}\sin\left(\frac{\pi x_d}{L_0}\right). \tag{2.2.30}$$

In two dimensions, where $\mathbf{x}_\perp$ is simply a number, there are two degenerate equilibrium buckled configurations corresponding to $\pm|\hat{\mathbf{x}}_\perp(x_d)|$. In three dimensions, however, there are an infinite number, consistent with a $U(1)$ symmetry corresponding to rotation about the x_d-axis.

The energy of this equilibrium buckled configuration is

$$H = \frac{\tau^2}{2g} - \frac{(\tau_c(0) - \tau)^2}{2g} = \frac{2\tau\tau_c(0) - \tau_c(0)^2}{2g}, \tag{2.2.31}$$

indicating a constant force at $T = 0$ in the buckled phase

$$f = g\frac{\partial H}{\partial \tau} = \tau_c(0). \tag{2.2.32}$$

2.2.3 Fluctuation corrections to stability and finite-temperature buckling

The finite-temperature phases are determined by the minima of the free energy of the rod, which includes entropic contributions. At finite temperature, thermal fluctuations excite all modes of the rod, and these fluctuations renormalize the stability of the rod against buckling. In order to analyze this entropic effect on the buckling transition, at which the first mode q_1 becomes unstable, we follow a procedure similar to that of momentum shell renormalization. We first separate the first modes from the higher-momentum fluctuation modes:

$$\boldsymbol{\pi} = \boldsymbol{\pi}_q^< + \boldsymbol{\pi}_q^>, \tag{2.2.33}$$

where

$$\boldsymbol{\pi}_q^< = \begin{cases} \boldsymbol{\pi}_q & \text{if } |q| = q_1 \\ 0 & \text{if } |q| > q_1 \end{cases} \quad \text{and} \quad \boldsymbol{\pi}_q^> = \begin{cases} 0 & \text{if } |q| = q_1 \\ \boldsymbol{\pi}_q & \text{if } |q| > q_1 \end{cases}. \tag{2.2.34}$$

It follows that $\boldsymbol{\pi}(x_d) = \boldsymbol{\pi}^<(x_d) + \boldsymbol{\pi}^>(x_d)$. These two components are decoupled in the quadratic Hamiltonian because they are nonzero over disjoint momentum ranges and, therefore, orthogonal, so

$$H_2 = H_2(\boldsymbol{\pi}^<) + H_2(\boldsymbol{\pi}^>). \tag{2.2.35}$$

In the quartic-order Hamiltonian H_4, on the other hand, they are coupled via cross terms.

The partition function can then be written as

$$\begin{aligned} Z &= \int \mathcal{D}\boldsymbol{\pi}^{<}\mathcal{D}\boldsymbol{\pi}^{>}\, e^{-\frac{1}{T}(H_0+H_2(\boldsymbol{\pi}^{<})+H_2(\boldsymbol{\pi}^{>})+H_4(\boldsymbol{\pi}^{<},\boldsymbol{\pi}^{>}))} \\ &= \int \mathcal{D}\boldsymbol{\pi}^{<}\, e^{-F^{<}(\boldsymbol{\pi}^{<})/T} \\ &= Z_0^{>} \int \mathcal{D}\boldsymbol{\pi}^{<}\, e^{-(H_0+H_2(\boldsymbol{\pi}^{<}))/T} \left\langle e^{-H_4(\boldsymbol{\pi}^{<},\boldsymbol{\pi}^{>})/T} \right\rangle_{>} \end{aligned} \tag{2.2.36}$$

where, in the second line, we define the Landau free energy

$$F^{<}(\boldsymbol{\pi}^{<}) = H_0 + H_2(\boldsymbol{\pi}^{<}) - T \ln \int \mathcal{D}\boldsymbol{\pi}^{>}\, e^{-\frac{1}{T}(H_2(\boldsymbol{\pi}^{>})+H_4(\boldsymbol{\pi}^{<},\boldsymbol{\pi}^{>}))}. \tag{2.2.37}$$

This Landau free energy, with all other modes $\boldsymbol{\pi}^{>}$ integrated out, determines the finite-temperature stability of the first mode. This is because the resulting $F^{<}(\boldsymbol{\pi}^{<})$ will include terms quadratic order in $\boldsymbol{\pi}^{<}$,

$$F_2^{<}(\boldsymbol{\pi}^{<}) = \frac{1}{8L_0} \sum_{q}^{<} (\tilde{\tau} + \tilde{\kappa} q^2) \boldsymbol{\pi}_q^2, \tag{2.2.38}$$

with the original elastic parameters replaced by renormalized ones, which is subject to a stability criterion similar to the one encountered in the $T = 0$ analysis. Therefore, to facilitate the calculation of integrating out $\boldsymbol{\pi}^{>}$, we have introduced the quantities

$$Z_0^{>} = \int \mathcal{D}\boldsymbol{\pi}^{>} e^{-H_2(\boldsymbol{\pi}^{>})/T}, \tag{2.2.39}$$

which is the quadratic-order partition function of $\boldsymbol{\pi}^{>}$, and

$$\left\langle e^{-H_4(\boldsymbol{\pi}^{<},\boldsymbol{\pi}^{>})/T} \right\rangle_{>} \equiv \frac{1}{Z_0^{>}} \int \mathcal{D}\boldsymbol{\pi}^{>}\, e^{-\frac{1}{T}(H_2(\boldsymbol{\pi}^{>})+H_4(\boldsymbol{\pi}^{<},\boldsymbol{\pi}^{>}))}. \tag{2.2.40}$$

Following a cumulant expansion, we can then write

$$\left\langle e^{-H_4(\boldsymbol{\pi}^<,\boldsymbol{\pi}^>)/T}\right\rangle_> = e^{-\frac{1}{T}\langle H_4\rangle_> + \frac{1}{2T^2}\left(\langle H_4^2\rangle_> - \langle H_4\rangle_>^2\right) + \mathcal{O}\left((H_4/T)^3\right)}, \tag{2.2.41}$$

which yields additional terms in the exponential that can, therefore, be directly included into the Landau free energy as

$$F^<(\boldsymbol{\pi}^<) = H_0 + H_2(\boldsymbol{\pi}^<) + \langle H_4\rangle_> + \frac{1}{T}\left(\langle H_4^2\rangle_> - \langle H_4\rangle_>^2\right) + \mathcal{O}\left(\frac{H_4^3}{T^2}\right). \tag{2.2.42}$$

Since we are ultimately trying to deduce the effect of thermal fluctuations on the stability threshold, we are interested in the corrections to the quadratic terms in $|\boldsymbol{\pi}^<|$. In the straight phase, $\langle \pi_a \pi_b\rangle \sim T\delta_{ab}$, meaning that $\langle H_4\rangle \sim T|\boldsymbol{\pi}^<|^2$ will provide an $O(T)$ correction to the quadratic-order coefficients, while terms from $\langle H_4^2\rangle/T$ will result in an $O(T^2)$ correction. Since we are doing a perturbative expansion in small fluctuations, which necessitates small temperatures, we need only calculate $\langle H_4\rangle_>$.

The explicit form of H_4 is given in Eq. (2.2.17), and here we replace $\boldsymbol{\pi}$ by $\boldsymbol{\pi}^< + \boldsymbol{\pi}^>$. Expanding each term in H_4 out, we have (note that we are using Einstein summation notation over the $d-1$ components of the $\boldsymbol{\pi}$ field)

$$\begin{aligned}
-\frac{\tau}{8}\int_0^{L_0} dx_d\, \langle|\boldsymbol{\pi}|^4\rangle_> &= -\frac{\tau}{8}\int_{-L/2}^{L/2} dx_d\, \langle \pi_a\pi_a\pi_b\pi_b\rangle_> \\
&= -\frac{\tau}{8}\int_0^{L_0} dx_d \Big[\pi_a^<\pi_a^<\pi_b^<\pi_b^< + \pi_a^<\pi_a^<\langle\pi_b^>\pi_b^>\rangle_> + 4\pi_a^<\pi_b^<\langle\pi_a^>\pi_b^>\rangle_> \\
&\qquad\qquad + \pi_b^<\pi_b^<\langle\pi_a^>\pi_a^>\rangle_> + \langle\pi_a^>\pi_a^>\pi_b^>\pi_b^>\rangle_>\Big] \\
&= -\frac{\tau}{8}\int_0^{L_0} dx_d \left[|\boldsymbol{\pi}^<|^4 + 2(d-1)|\boldsymbol{\pi}^<|^2\frac{1}{(2L_0)^2}\sum_q^> G_{0q} + 4|\boldsymbol{\pi}^<|^2\frac{1}{(2L_0)^2}\sum_q^> G_{0q} + \langle|\boldsymbol{\pi}^>|^4\rangle_>\right] \\
&= -\frac{\tau}{8}\int_0^{L_0} dx_d \left[|\boldsymbol{\pi}^<|^4 + 2(d+1)|\boldsymbol{\pi}^<|^2\frac{1}{(2L_0)^2}\sum_q^> G_{0q} + \langle|\boldsymbol{\pi}^>|^4\rangle_>\right],
\end{aligned} \tag{2.2.43}$$

$$-\frac{3\kappa}{4}\int_0^{L_0} dx_d\ \langle|\boldsymbol{\pi}|^2|\partial_{x_d}\boldsymbol{\pi}|^2\rangle_> = -\frac{3\kappa}{4}\int_0^{L_0} dx_d\ \Big[|\boldsymbol{\pi}^<|^2|\partial_{x_d}\boldsymbol{\pi}^<|^2 + (d-1)|\boldsymbol{\pi}^<|^2\frac{1}{(2L_0)^2}\sum_q^> q^2 G_{0q} + (d-1)|\partial_{x_d}\boldsymbol{\pi}^<|^2\frac{1}{(2L_0)^2}\sum_q^> G_{0q} + \langle|\boldsymbol{\pi}^>|^2|\partial_{x_d}\boldsymbol{\pi}^>|^2\rangle_>\Big], \tag{2.2.44}$$

$$-\frac{\kappa}{2}\int_0^{L_0} dx_d\ \langle(\boldsymbol{\pi}\cdot\partial_{x_d}\boldsymbol{\pi})^2\rangle_> = -\frac{\kappa}{2}\int_0^{L_0} dx_d\ \Big[(\boldsymbol{\pi}^<\cdot\partial_{x_d}\boldsymbol{\pi}^<)^2 + |\boldsymbol{\pi}^<|^2\frac{1}{(2L_0)^2}\sum_q^> q^2 G_{0q} + |\partial_{x_d}\boldsymbol{\pi}^<|^2\frac{1}{(2L_0)^2}\sum_q^> G_{0q} + \langle(\boldsymbol{\pi}^>\cdot\partial_{x_d}\boldsymbol{\pi}^>)^2\rangle_>\Big], \tag{2.2.45}$$

and

$$\frac{g}{8}\iint_0^{L_0} dx_d dx_d'\ \langle|\boldsymbol{\pi}(x_d)|^2|\boldsymbol{\pi}(x_d')|^2\rangle_> = \frac{g}{8}\iint_0^{L_0} dx_d dx_d'\ \Big[|\boldsymbol{\pi}^<(x_d)|^2|\boldsymbol{\pi}^<(x_d')|^2 + \langle|\boldsymbol{\pi}_>(x_d)|^2|\boldsymbol{\pi}_>(x_d')|^2\rangle_>\Big] + \frac{g}{8}\int_0^{L_0} dx_d\ 2(d-1)|\boldsymbol{\pi}^<(x_d)|^2\frac{1}{(2L_0)}\sum_q^> G_{0q}. \tag{2.2.46}$$

In these equations,

$$G_{0q} = \frac{4L_0 T}{\tau + \kappa q^2}. \tag{2.2.47}$$

Using the notation of Eq. (2.2.52), we can also write

$$\frac{1}{4L_0^2}\sum_q^> G_{0q} = 2\bar{T}\mathcal{A}(\bar{\tau}). \tag{2.2.48}$$

Feynman diagrams corresponding to these terms are included in Fig. 2.2.

As mentioned previously, we are interested in extracting the contribution to the coefficients of the quadratic-order $\boldsymbol{\pi}^<$ terms from $\langle H_4\rangle_>$. Collecting terms, and defining renor-

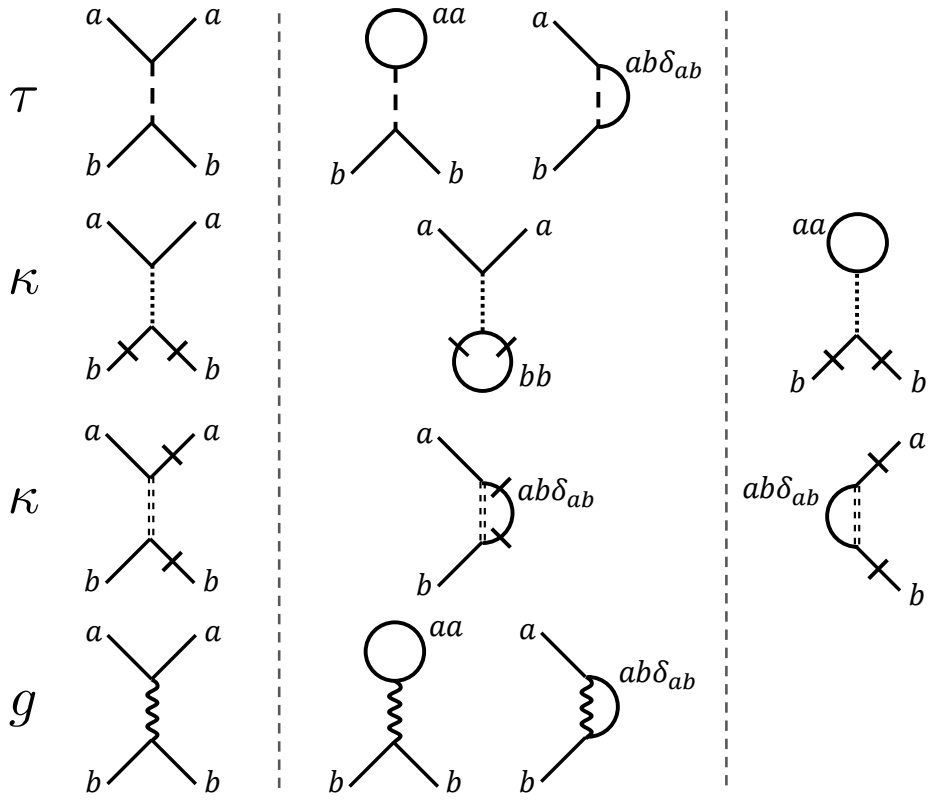

Figure 2.2: Feynman diagrams corresponding to terms in $\langle H_4 \rangle_>$. The diagrams are systematically divided into rows and columns: each row is associated with a single elastic parameter that is the coefficient of the originating term in $\langle H_4 \rangle_>$, while the columns specify which elastic parameter's renormalization the diagrams contribute to. Namely, the first column presents the basic vertex diagrams, while the second and third columns list those that renormalize τ and κ, respectively. Each external leg corresponds to a $\boldsymbol{\pi}^<$ field, and slashes denote spatial derivatives with respect to x_d. The various internal lines differentiate between the interactions and are used for index bookkeeping.

malized elastic parameters $\tilde{\tau}$ and $\tilde{\kappa}$ as the modified coefficients, we find

$$\tilde{\tau} = \tau + \frac{1}{2}\left[-(d+1)\tau + (d-1)gL_0\right] \frac{1}{(2L_0)^2} \sum_q^> G_{0q} - \kappa \left[1 + \frac{3}{2}(d-1)\right] \frac{1}{(2L_0)^2} \sum_q^> q^2 G_{0q}, \tag{2.2.49}$$

$$\tilde{\kappa} = \kappa \left\{1 - \left[1 + \frac{3}{2}(d-1)\right] \frac{1}{(2L_0)^2} \sum_q^> G_{0q}\right\}. \tag{2.2.50}$$

The $\frac{1}{(2L_0)^2}\overset{>}{\sum_q} q^2 G_{0q}$ term appears to have an ultraviolet divergence, but it actually vanishes. This is because it originates from quartic-order terms in the bending energy (see Eq. (2.2.17)) where the spatial derivatives are on the legs that combine to form the loops in the Feynman diagrams. This corresponds to a factor of $|\boldsymbol{\pi}'|^2$, which is the leading-order term in the gradient expansion of the difference in orientation between neighboring segments on the rod. We can show this by restoring the full form of this factor for a segmented rod, $\sum_{x_d} |\boldsymbol{\pi}(x_d) - \boldsymbol{\pi}(x_d + \ell_0)|^2$, where ℓ_0 is the projected length of each segment, and writing it in momentum space. Doing so, we obtain a factor of $1 - \cos(q\ell_0)$ rather than only the leading-order term q^2. Here, $q = n\pi/N\ell_0$, so that $q\ell_0 = n\pi/N$. Taking the continuum limit where $N \to \infty$, the factor $1 - \cos(q\ell_0)$ is highly oscillatory and the thus the whole expression, $\frac{1}{(2L_0)^2}\overset{>}{\sum_q}[1 - \cos(q\ell_0)]G_{0q}$ vanishes.

Simplifying these equations, we obtain expressions for the renormalized elastic parameters,

$$\begin{aligned}
\tilde{\tau} &\equiv \tau + \mathcal{A}(\bar{\tau})\bar{T}|\tau_c(0)|\left[(d-1)\bar{g} + (d+1)\bar{\tau}\right] \\
\tilde{\kappa} &\equiv \kappa - \mathcal{A}(\bar{\tau})\bar{T}(3d-1)\kappa,
\end{aligned} \tag{2.2.51}$$

where we have defined the dimensionless quantities

$$\begin{aligned}
\bar{T} &\equiv \frac{T}{L_0|\tau_c(0)|} \\
\bar{g} &\equiv \frac{gL_0}{|\tau_c(0)|} \\
\bar{\tau} &\equiv \frac{\tau}{\tau_c(0)} > 0,
\end{aligned} \tag{2.2.52}$$

and

$$\mathcal{A}(\bar{\tau}) \equiv \sum_{n=2}^{\infty} \frac{1}{n^2 - \bar{\tau}} = \frac{3\bar{\tau} - 1}{2(\bar{\tau} - 1)\bar{\tau}} - \frac{\pi}{2\sqrt{\bar{\tau}}} \cot \pi\sqrt{\bar{\tau}}. \tag{2.2.53}$$

In accordance with the range of τ we are considering in this work, $0 < \bar{\tau} < 4$. As will be justified shortly, close to the $T = 0$ buckling transition, we can expand $\mathcal{A}(\bar{\tau})$ in powers of $\bar{\tau} - 1$,

$$\mathcal{A}(\bar{\tau}) = \frac{3}{4} + \left(\frac{\pi^2}{12} - \frac{11}{16}\right)(\bar{\tau} - 1) + O[(\bar{\tau} - 1)^2]. \tag{2.2.54}$$

The magnitude of the effective compression, $\tilde{\tau}$, as well as the effective bending rigidity, $\tilde{\kappa}$, both decrease with increasing temperature. It is easy to understand the decrease in $\tilde{\tau}$: thermal fluctuations tend to increase the instantaneous arc length of the rod from its $T = 0$ straight-rod length so that the rod effectively feels less compression. In previous works [69, 74], the fluctuation correction to $\tilde{\kappa}$ was shown to have a prefactor of $(d - 2)$ instead of $(3d - 1)$ as we have here. The difference arises from the fact that the rod is assumed to be inextensible and, therefore, is modeled as a worm-like chain in these previous papers, whereas it is extensible in our model. Consequently, it was necessary to reparametrize the rod in terms of x_d rather than the arc length, s, modifying the form of the bending energy.

The buckling transition occurs when the first mode becomes unstable, which is when

$$\tilde{\tau} + \tilde{\kappa} q_1^2 = 0. \tag{2.2.55}$$

This condition can be solved to obtain a critical temperature separating the straight ($\bar{T} > \bar{T}_c$) and buckled ($\bar{T} < \bar{T}_c$) phases of the rod for a given compression $\bar{\tau} > 1$,

$$\bar{T}_c(\bar{\tau}) = \frac{\bar{\tau} - 1}{[(d-1)\bar{g} + (d+1)\bar{\tau} - (3d-1)]\,\mathcal{A}(\bar{\tau})}. \tag{2.2.56}$$

The phase boundary in two dimensions determined by this equation is plotted as the solid black line in Fig. 2.1. The three-dimensional version is shown in Fig. 2.3. In the limit that we have been considering of stretching stiffness much greater than bending stiffness [Eq.(2.2.2)],

we have $\bar{g} \gg 1$, so that we can write a simplified expression for the critical temperature,

$$\bar{T}_c(\bar{\tau}) = \frac{\bar{\tau} - 1}{(d-1)\bar{g}\mathcal{A}(\bar{\tau})} \to \frac{4\,(\bar{\tau} - 1)}{3(d-1)\bar{g}}. \tag{2.2.57}$$

The expression following the arrow is the limiting case true for sufficiently low temperatures such that $\bar{g}\bar{T} \ll 1$, since, as we can see from the initial equality in Eq. (2.2.57), that condition necessitates that $\bar{\tau} - 1 \ll 1$, as well. In that case, we can write the critical temperature to leading order in $\bar{\tau} - 1$, allowing us to use the zeroth-order term in the expansion of $\mathcal{A}(\bar{\tau})$ in Eq. (2.2.54).

This leading-order relation can be inverted to obtain an expression for the critical compression for buckling at a finite temperature T,

$$\tau_c(T) \simeq \tau_c(0)\left[1 + \frac{3(d-1)}{4}\bar{g}\bar{T}\right]. \tag{2.2.58}$$

This clearly represents a critical compression that is of larger magnitude than the zero-temperature critical value. In other words, the buckling transition is "delayed" by thermal fluctuations.

2.2.4 Effective force

In this analysis, we have utilized the ensemble with fixed end-to-end distance L_0. At $T = 0$, taking the derivative of the Hamiltonian with respect to L_0 yields that the force on the rod is simply $\tau = g(L_0 - L_{\text{rest}})$ in the straight phase (with $\tau < 0$ corresponding to compressional force) and $\tau_c(0)$ in the buckled phase [Eq. (2.2.32)].

At finite T, we determine the effective force f through

$$f = \frac{\partial F}{\partial L_0} = \frac{\partial \tau}{\partial L_0}\frac{\partial F}{\partial \tau} = g\frac{\partial F}{\partial \tau}, \tag{2.2.59}$$

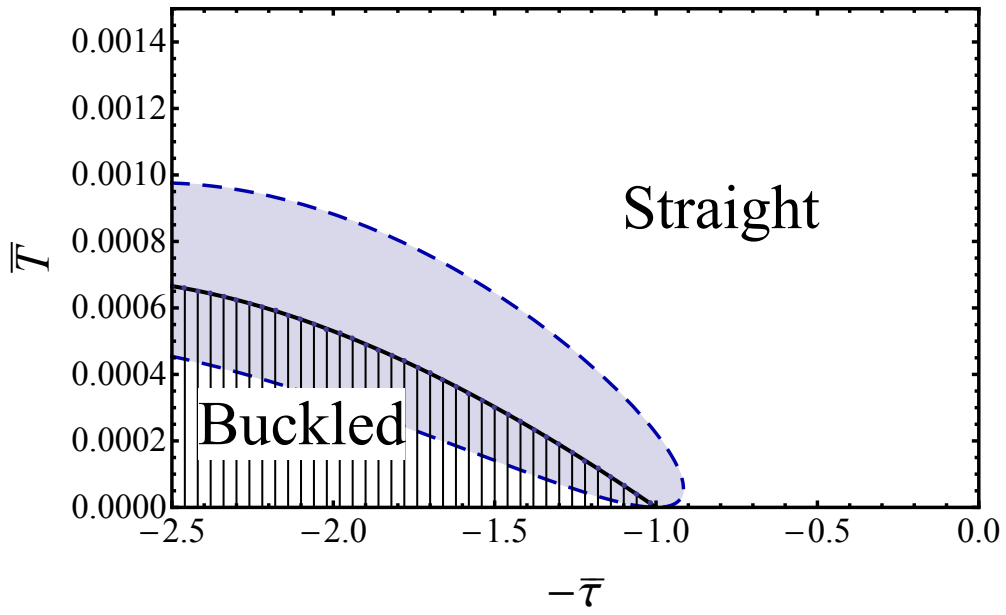

Figure 2.3: Predicted phase diagram for three-dimensional finite-temperature buckling of an extensible rod in the plane of normalized compression and temperature. The thick black curve represents the phase boundary between the straight (unshaded) and the buckled (shaded with vertical lines) phases. The dashed curve denotes the boundary of the critical regime (light blue region) where the thermal-fluctuation correction to the effective force is of $O(\sqrt{T})$.

with the free energy given by

$$F = -T \ln Z = -T \ln \int \mathcal{D}\boldsymbol{\pi}^{<} e^{-F^{<}(\boldsymbol{\pi}^{<})/T}, \tag{2.2.60}$$

where, as defined earlier, $F^{<}$ is the Landau free energy with only $\boldsymbol{\pi}^{>}$ integrated out. It is useful to note that f is calculating by taking the derivative of F with respect to the compression τ, rather than by taking the derivative directly with respect to L_0. This is intentional, as the derivative with respect to L_0 would also act on the prefactors of L_0 in the Fourier transform (or, equivalently, on the integration limits in real space), which would introduce an ultraviolet divergence that scales linearly with the high-momentum cutoff. Strictly speaking, the effective force f obtained via differentiation with respect to τ describes the change of the free energy that occurs with changing the amount of compression τ while keeping L_0 constant.

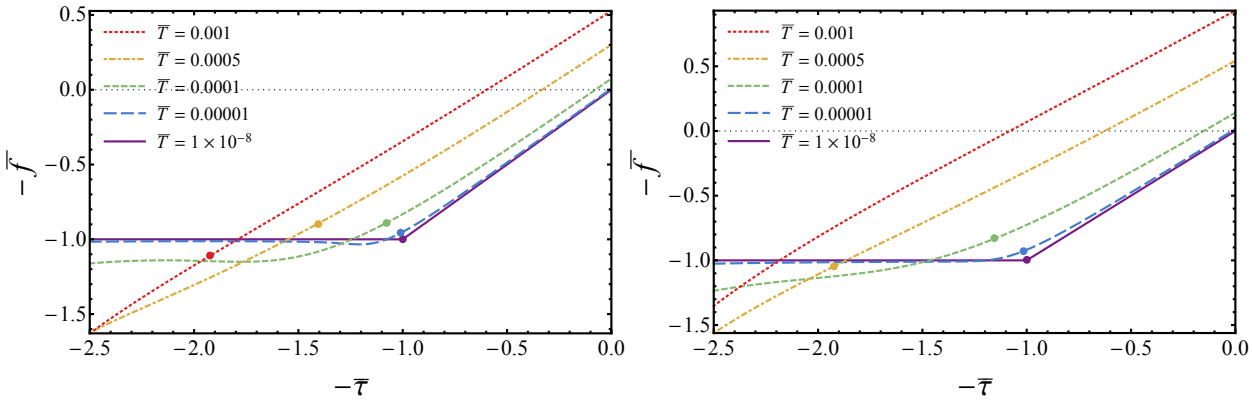

Figure 2.4: Plots of the dimensionless effective force in both two (a) and three (b) dimensions at various values of $\bar{T}$. Note that $-\bar{f} = f/|\tau_c(0)|$. Negative values correspond to a compressive force, while positive values correspond to a stretching force. The dots on each curve indicate the transition point between the straight and buckled phases for each value of $\bar{T}$. The $\bar{T} = 0.001$ curve in three dimensions does not have a dot as there is no phase transition at that temperature; the rod remains in the straight phase.

The Landau free energy $F^<$, as defined in Eq. (2.2.37), can be written to leading order in T as

$$F^< = H_0 - T \ln Z_0^> + b_2 T |\boldsymbol{\pi}_1|^2 + b_4 T |\boldsymbol{\pi}_1|^4, \tag{2.2.61}$$

where $Z_0^>$ is defined in Eq. (2.2.39). The coefficients b_2 and b_4, and the integral over $\boldsymbol{\pi}_1$, are derived in App. A. We have only needed to retain terms to quadratic order in $\boldsymbol{\pi}^>$ in (2.2.61) because $\boldsymbol{\pi}^>$ modes are stable at $\boldsymbol{\pi}^> = \mathbf{0}$; quartic-order terms in (renormalized) $\boldsymbol{\pi}_1$ are necessary, however, because the quadratic-order coefficient, b_2, can become negative for $\boldsymbol{\pi}_1$ – thus, higher-order terms in the potential are needed to evaluate the free energy.

As detailed in App. A, we find that thermal fluctuations reduce the compressional force in the straight phase but enhance it in the buckled phase; these modifications are of order T except very close to the transition for small values of $\bar{g}\bar{T}$, where there is a decrease in the compression of order $\sqrt{T}$, as shown in Fig. 2.4.

2.3 Monte Carlo simulations

We perform Monte Carlo (MC) simulations in two and three dimensions to corroborate our analytical results. The rod is discretized into N segments with fixed vertical length $\ell_0 = L_0/N$ along the x_d-axis. The segments are allowed to have transverse fluctuations $\mathbf{x}_{\perp,j}$ and to, consequently, cause stretching or compression and bending of the rod, as discussed in Sec. 2.2. The fixed boundary conditions necessitate that $\mathbf{x}_{\perp,0} = \mathbf{x}_{\perp,N} = \mathbf{0}$.

The Metropolis algorithm is used in our Monte Carlo simulations, in which, at each MC step, a segment is selected at random, and a random trial displacement in the transverse direction is attempted. For a given rod under a certain compression, runs are performed at various temperatures. We choose the transverse displacement of the middle segment, $|\mathbf{x}_{\perp,\frac{N}{2}}|$, to be our order parameter. In the straight phase $|\mathbf{x}_{\perp,\frac{N}{2}}|$ is governed by a Gaussian distribution with its mean at $\mathbf{0}$, whereas in the buckled phase, the distribution of $|\mathbf{x}_{\perp,\frac{N}{2}}|$ becomes double-well (in $d = 2$) or Mexican-hat ($d = 3$) with minima at

$$|\hat{\mathbf{x}}_{\perp,\frac{N}{2}}| = \frac{1}{\pi}\sqrt{\frac{4L_0(\tau_c(0) - \tau)}{g}}. \tag{2.3.1}$$

At the buckling transition, the distribution sharply deviates from Gaussian. To capture this transition, we calculate the Binder cumulant of the distribution [75],

$$U_L = 1 - \frac{\langle |\mathbf{x}_{\perp,\frac{N}{2}}|^4 \rangle}{3\langle |\mathbf{x}_{\perp,\frac{N}{2}}|^2 \rangle^2}. \tag{2.3.2}$$

The value of U_L decreases as the temperature is lowered and the system experiences the straight-to-buckled phase transition. This decrease becomes increasingly sharp for progressively larger systems, and the simultaneous crossing of Binder cumulant curves for various system sizes determines the location of the critical temperature T_c.

To verify our phase diagrams in Figs. 2.1 and 2.3 via the crossing of the Binder cumulant curves, we simulate rods containing 10, 12, and 14 segments (corresponding to

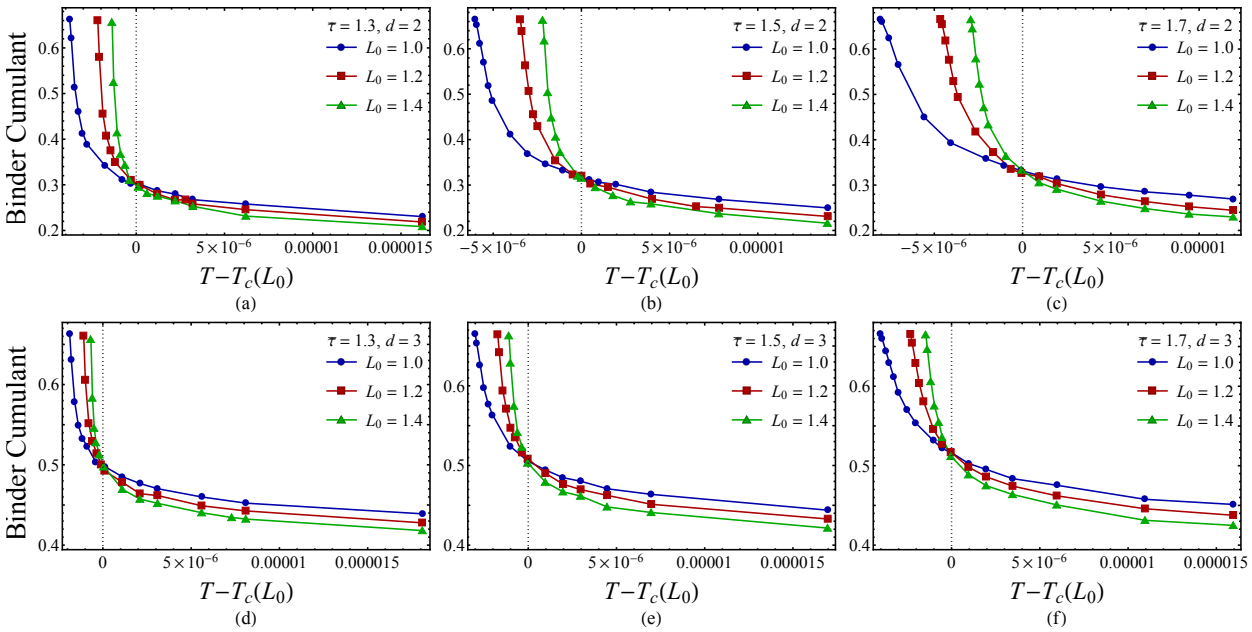

Figure 2.5: Results of Monte Carlo simulations run with $\bar{\tau} = 1.3, 1.5, 1.7$ in both two ((a)-(c)) and three ((d)-(f)) dimensions. For each value of $\bar{\tau}$ and in each dimension, three different lengths were simulated. Each data point corresponds to the combined Binder cumulant value of ten independent simulations run with identical parameters. The lines connecting the data points explicitly illustrate that the Binder cumulant curves do indeed simultaneously cross at, or very close to, the respective critical temperatures.

$L_0 = 1.0, 1.2, 1.4$, respectively, so that $\ell_0 = 0.1$ is kept fixed). As discussed in Sec. 2.2, $g = \pi a^2 E / L_{\text{rest}}$, so to keep a and E constant across the various-sized rods (so that each rod has the same cross-section and is made of the same materials), we take the values of g to be $g = 10.00, 8.34, 7.15$, corresponding to the three choices of length. In addition, in accordance with Eqs. (2.2.1) and (2.2.2), we take $\kappa = 0.01/\pi^2$. With these parameters, for $L_0 = 1$, we have $\tau_c(0) = -0.01$. We take $\bar{\tau} = \tau/\tau_c(0) = 1.3, 1.5, 1.7$ and vary T to observe the transition. For these three $\bar{\tau}$ values, with $d = 2$ and all other elastic parameters corresponding to $L_0 = 1$, $T_c = 3.78 \times 10^{-6}, 6.03 \times 10^{-6}, 8.05 \times 10^{-6}$, satisfying the requirement that the persistence length $l_p \equiv \kappa/T \simeq 10^2$ is much longer than the length of the rod L_0, and, therefore, the transverse fluctuations are small. This justifies the small $\boldsymbol{\pi}$ expansion we make.

The resulting U_L curves from our MC simulations are shown in Fig. 2.5. Because T_c, as given in Eq. (2.2.57), depends on the system size L_0 through $|\tau_c(0)|$, it is necessary to shift

the U_L curves by theoretical predictions of $T_c(\tau)$ to observe the crossing of the three curves for the different system sizes. The crossing of the three U_L curves for all three values of $\bar{\tau}$ in both two and three dimensions verifies our theoretical prediction of the finite-temperature buckling transition.

2.4 Conclusion and discussion

In this chapter, we used both analytic theory and MC simulations to investigate the buckling of an extensible elastic rod at finite temperature. We find that, in both two and three dimensions, buckling is delayed by thermal fluctuations, and near the transition, there is a critical regime in which the fluctuation correction to the average compression force is of order $\sqrt{T}$.

In comparing the two phase diagrams in Figs. 2.1 and 2.3, one can observe that the straight-rod phase is more stabilized in three dimensions than in two dimensions. This can be intuitively attributed to the fact that in higher dimensions, there are an increasing number of transverse, soft directions in which segments in the straight rod can move compared to the when the rod is buckled. Therefore, the straight rod is increasingly entropically protected, as there are a larger number of accessible states.

Our analytic theory is a perturbative theory that applies to small fluctuations. This requires that the dimensionless temperature $\bar{T} \ll 1$. This condition can be written in terms of the persistence length $l_p = \kappa/T$ as $L_{\rm rest}/(\pi^2 l_p) \ll 1$, which is satisfied by stiff ($L_{\rm rest} \ll l_p$) and semiflexible ($L_{\rm rest} \sim l_p$) polymers.

Our predicted phase diagrams can be compared to experimental observations of buckling [55–59]. Physical rods have finite instead of infinitely large stiffness against extension and compression, and our theory directly applies to the experimental setup of controlling the projected (end-to-end rather than contour) length of the rod and observing buckling as the projected length is decreased. Our result of delayed buckling as a result of thermal fluc-

tuations can have interesting applications in many phenomena, e.g., buckling of semiflexible polymers in disordered polymer networks [27, 54, 76].

At lower temperatures, quantum fluctuations also become important. To make a simple estimate of the temperature scale at which this occurs, we include the kinetic energy term

$$H_{\text{kinetic}} = \int dx_d \, \rho \left| \frac{\partial \mathbf{x}_\perp}{\partial t} \right|^2, \tag{2.4.1}$$

where ρ is the linear mass density of the rod. Combining this with the potential energy terms in H, we have a phonon energy given by

$$\hbar\omega \sim \frac{\hbar|q|}{\sqrt{\rho}} \sqrt{\tau + \kappa q^2}. \tag{2.4.2}$$

Therefore, in addition to thermal fluctuation corrections, quantum fluctuations also contribute to the renormalization of $\tilde{\tau}$ and $\tilde{\kappa}$, moving the critical τ to a larger compression value (in magnitude) even at $T = 0$. The significance of such contributions from quantum fluctuations can be estimated by comparing $\hbar\omega$ of generic modes with $k_B T$. For the simple case of stiff polymers of length $10^{-6}\,\text{m}$ and persistence length $10^{-3}\,\text{m}$, we estimate that the characteristic temperature for $\hbar\omega \sim k_B T$ is $T \sim 10^{-6}\,\text{K}$, which is extremely low. Other systems with higher stiffness or shorter lengths may have stronger quantum effects.

Our result that, in both two and three dimensions, the buckling transition is delayed by thermal fluctuations contrasts with previous studies of finite-temperature buckling of polymers using the inextensible worm-like chain model [69, 71]. The extensibility of the rod in our model allows for an additional independent quartic-order term in the Hamiltonian, and this term plays an important role in determining the renormalization of the stability of the first mode, leading to the phase diagram shown in Fig. 2.1. The simple physical reasoning underlying this is the following: buckling of an elastic rod is a result of the competition between compressional energy (which favors the buckled phase) and bending energy (which favors the straight phase). Allowing extensibility and compressibility softens the first effect,

and, thus, the rod is in the straight phase for a wider parameter range.

In addition, while numerous recent studies have focused on zero-temperature mechanical instability in both ordered and disordered systems [18, 28, 77–83], the behavior of these systems at finite temperature remains largely unexplored [13, 46, 61–63, 84, 85]. Our model characterizes a relatively clean system that exhibits a shifted second-order transition, and the results can be compared to those of future studies on finite-temperature mechanical instabilities in various systems.

CHAPTER III

Twisted-untwisted transition of the kagome lattice at finite temperature and the self-assembly of the twisted kagome lattice with Janus particles

3.1 Introduction

In this chapter, we will continue the study of the effects of thermal fluctuations on mechanical systems near the point of instability by considering the structural phase transition between the kagome lattice and the twisted kagome lattice, which are related by a uniform twisting mechanism in which all triangles connecting the three sites in single unit cells are rotated by the same twisting angle α. We determine the phase boundary between these two lattices at both $T = 0$ and at finite temperature to determine the effect of thermal fluctuations on the transition. We then consider a system of self-assembling triblock Janus particles, which consist of two attractive patches separated by an electrically-charged middle band, and show how we can allow for the creation of a twisted kagome structure and, additionally, for the temperature-controlled structural transition between a twisted kagome structure and a kagome structure by synthesizing a triblock Janus particle that has an attractive patch that

is offset with respect to the other patch. This can allow for the automated creation of open structures with novel mechanical and transformable properties.

Recently, the structural phase transition between the square lattice and a system of isoenergetic lattices with rows of rhombus plaquettes (resulting in exponentially-many – $2^{N_x} + 2^{N_y}$, where N_x (N_y) is the number of rows (columns) of plaquettes in the lattice – degenerate lattices with various zigzagged boundaries) was studied [13] using an analogous spring model to the one we will be using in our subsequent analysis of the kagome lattice structural phase transition. It was found that the straight-edge rhombus lattice is favored over all other zigzag configurations due to it having the largest vibrational entropy ("order-by-disorder"), and that the square lattice is stabilized by diverging thermal fluctuations as the system approaches instability. Both of these are due to the coupling of thermal fluctuations and floppy modes near mechanical instability. Another interesting example of the impact of entropic stabilization due to large thermal fluctuations is discussed in the context of disordered systems [60], where it is found that even under-coordinated lattices, with $\langle z \rangle < 2d$, can be stabilized.

The kagome lattice family is also of interest in the rapidly growing field of topological mechanics. Under periodic boundary conditions, the nearest-neighbor (NN) kagome lattice, due to its sets of straight lines of NN bonds running across the lattice in three symmetry directions, has a large number of floppy modes (Fig. 3.3). On the other hand, the twisted kagome lattice, which does not have straight lines, does not have floppy modes other than the two trivial modes at $\mathbf{q} = 0$. Due to the Maxwell counting argument, however, we know that if we cut out a rectangular portion containing N sites of either lattice from a larger periodic version, because the two are Maxwell lattices, $\sqrt{N}$ bonds will be cut and, consequently, $\sqrt{N}$ floppy modes will appear. In the twisted kagome lattice, which does not have any bulk floppy modes, the floppy modes will be localized to the surface – a finite twisted kagome lattice will have surface floppy modes that cannot penetrate into the bulk and are insensitive to local perturbations [86]. Thereafter, this phenomenon of robust floppy edge modes was

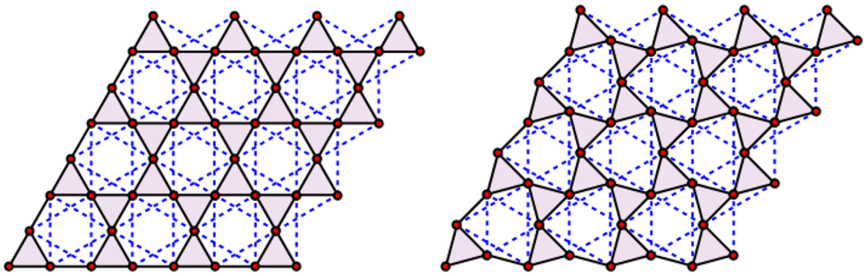

Figure 3.1: (Left) The kagome lattice with lattice sites (red circles), and nearest-neighbor (NN) (solid black lines) and next-nearest-neighbor (NNN) (dashed blue lines) bonds. Note the sets of straight lines of NN bonds in three symmetry directions, which allow for states of self-stress and, consequently, floppy modes under periodic boundary conditions when NNN bonds are not present. (Right) The twisted kagome lattice. Notice that the straight lines no longer exist, so that the states of self-stress as well as floppy modes have been removed.

connected to topology with the introduction of a quantity called topological polarization [18, 87], a vector that points in the direct of topologically-protected floppy edge modes that cannot be destroyed by local perturbations. This led to the proposals (and in some cases, creation) of mechanical metamaterials with novel properties that utilize the kagome connection topology. For instance, joining together a twisted kagome lattice and a deformed kagome lattice (which has the same connection topology as a kagome lattice, but with site positions deformed so that the triangles are no longer equilateral) to create a domain wall allows for the the precise positioning of floppy modes and states of self-stress. Recently, the use of the uniform soft twisting mode of a deformed kagome lattice with two different types of triangles was shown to control transitions between various topological states with differing topologically-protected mechanical properties – for example, the location of stiff and floppy edges [7]. Though we will not address topological aspects of the lattices in this dissertation, the coupling of topological mechanics with thermal fluctuations and/or self-assembly is an avenue that is certainly worth pursuing in the future.

3.2 Kagome lattice preliminaries

The kagome lattice family (see Fig. 3.1 for the two we will be discussing in this chapter) has three sites per unit cell. We take the center of the unit cell to be $(0,0)$; then the basis vectors are given by $\mathbf{d}_1 = \frac{a}{\sqrt{3}}(0,1)$, $\mathbf{d}_2 = a\left(-\frac{1}{2}, -\frac{1}{2\sqrt{3}}\right)$, $\mathbf{d}_3 = a\left(\frac{1}{2}, -\frac{1}{2\sqrt{3}}\right)$, where a is the distance between nearest-neighbor (NN) sites (note that, in this case, $2a$ is the lattice constant. The two primitive lattice vectors are given by

$$\mathbf{a}_1 = 2(\mathbf{d}_3 - \mathbf{d}_2) = (2,0)a, \qquad \mathbf{a}_2 = 2(\mathbf{d}_1 - \mathbf{d}_2) = (1,\sqrt{3})a \tag{3.2.1}$$

There are twelve unique bonds per unit cell – six nearest-neighbor bonds and six next-nearest-neighbor (NNN) bonds. The length of the NN bonds, as stated above, is a, and the length of the NNN bonds is $a\sqrt{3}$.

The twisted kagome lattice is formed by uniformly rotating all the triangular unit cells of the kagome lattice by an angle α. In this case, the basis vectors are given by $\mathbf{d}_1 = \frac{a}{\sqrt{3}}\left(-\sin\alpha, \cos\alpha\right)$, $\mathbf{d}_2 = \frac{a}{\sqrt{3}}\left(-\cos\left(\alpha + \frac{\pi}{6}\right), -\sin\left(\alpha + \frac{\pi}{6}\right)\right)$, $\mathbf{d}_3 = \frac{a}{\sqrt{3}}\left(\cos\left(\alpha - \frac{\pi}{6}\right), \sin\left(\alpha - \frac{\pi}{6}\right)\right)$, and the primitive lattice vectors are

$$\mathbf{a}_1(\alpha) = (1,0)a_L(\alpha), \qquad \mathbf{a}_2(\alpha) = \left(\frac{1}{2}, \frac{\sqrt{3}}{2}\right)a_L(\alpha), \tag{3.2.2}$$

where $a_L(\alpha) = 2a\cos\alpha$ is the lattice constant.

The underlying Bravais lattice of both the kagome lattice and the twisted kagome lattice is the 2-D hexagonal/triangular lattice (which, incidentally, is the underlying Bravais lattice of the honeycomb lattice, as well). The primitive lattice vectors of the reciprocal lattice are given by

$$\mathbf{d}_1 = \frac{2\pi\,\hat{\mathbf{z}} \times \mathbf{a}_2}{(\hat{\mathbf{z}} \times \mathbf{a}_2) \cdot \mathbf{a}_1}, \qquad \mathbf{d}_2 = \frac{2\pi\,\hat{\mathbf{z}} \times \mathbf{a}_1}{(\hat{\mathbf{z}} \times \mathbf{a}_1) \cdot \mathbf{a}_2}. \tag{3.2.3}$$

This yields primitive reciprocal lattice vectors

$$\mathbf{d}_1(\alpha) = \frac{2\pi}{a_L(\alpha)}\left(1, -\frac{1}{\sqrt{3}}\right) = \frac{\pi}{a\cos\alpha}\left(1, -\frac{1}{\sqrt{3}}\right) \tag{3.2.4}$$

$$\mathbf{d}_2(\alpha) = \frac{2\pi}{a_L(\alpha)}\left(0, \frac{2}{\sqrt{3}}\right) = \frac{\pi}{a\cos\alpha}\left(0, \frac{2}{\sqrt{3}}\right) \tag{3.2.5}$$

The resultant reciprocal lattice is also a hexagonal/triangular lattice with a hexagonal first Brillouin zone (1BZ). The volume of the unit cell in the direct lattice, v, and in the reciprocal lattice, v_0, are

$$v = 2\sqrt{3}a^2\cos^2\alpha, \qquad v_0 = \frac{2\pi^2}{\sqrt{3}a^2\cos^2\alpha}. \tag{3.2.6}$$

Points of high symmetry in the 1BZ are

$$\Gamma = (0,0), \quad M = \left(0, \frac{\pi}{\sqrt{3}\cos\alpha}\right), \quad K = \left(\frac{\pi}{3\cos\alpha}, \frac{\pi}{\sqrt{3}\cos\alpha}\right). \tag{3.2.7}$$

3.3 Zero-temperature analysis

Before including the effects of temperature, let us first consider the structural transition that occurs between the untwisted kagome lattice and the twisted kagome lattice at zero temperature. The Hamiltonian for a generic lattice with pairwise central-force potentials is given by

$$H = \sum_b V_b\left(|\mathbf{R}_b| - |\mathbf{R}_{0b}|\right) \equiv \sum_b V_b\left(\Delta R_b\right) \tag{3.3.1}$$

where b labels bonds between lattice sites l and l', V_b is the interaction potential of the bond, and

$$\mathbf{R}_b = \mathbf{R}_{l'} - \mathbf{R}_l \tag{3.3.2}$$

$$\mathbf{R}_{0b} = \mathbf{R}_{0l'} - \mathbf{R}_{0l} \tag{3.3.3}$$

are the bond vectors in the target and reference states, respectively. The reference (target) state describes the lattice before (after) the elastic deformation. For the current problem, to keep full generality initially, we will take the reference state to be a twisted kagome lattice with twisting angle α_0. Later on, we will specialize to the case of $\alpha_0 = 0$, as we will want the reference state to be the untwisted kagome lattice to be able to analyze its stability against twist fluctuations. In general, however, this analysis can be used to study deformations around any particular state picked out from the continuum of twisted kagome lattices generated by the uniform twisting by choosing a specific α_0. In the reference state, the position vector for a lattice site l is given by

$$\mathbf{R}_{0l} = l_1\mathbf{a}_1(\alpha_0) + l_2\mathbf{a}_2(\alpha_0) + \mathbf{d}_{i_l 0}, \tag{3.3.4}$$

where l_1, l_2 are coefficients of the primitive lattice vectors that determine the unit cell that the lattice is contained in, and $\mathbf{b}_{i_l 0}$ is the basis vector corresponding to the lattice site. Note that both the primitive lattice vectors and the basis vectors are determined by the reference-state twist angle, α_0. The target space position vector is given by

$$\mathbf{R}_l = l_1\mathbf{a}_1(\alpha) + l_2\mathbf{a}_2(\alpha) + \mathbf{d}_{i_l}. \tag{3.3.5}$$

Then the bond vectors are given by

$$\mathbf{R}_{0b} = \mathbf{R}_{0l'} - \mathbf{R}_{0l} = \mathbf{l}_b(\alpha_0) + \mathbf{d}_b(\alpha_0) \equiv \mathbf{R}_b^{\alpha_0} \tag{3.3.6}$$

$$\mathbf{R}_b = \mathbf{R}_{l'} - \mathbf{R}_l = \mathbf{l}_b(\alpha) + \mathbf{d}_b(\alpha) \equiv \mathbf{R}_b^{\alpha}. \tag{3.3.7}$$

For nearest-neighbor (NN) bonds, $|\mathbf{R}_b^{\alpha}| = |\mathbf{R}_b^{\alpha_0}|$ for any values of α and α_0 – the uniform twisting mode does not change NN bonds to all orders (hence why it is a floppy mode for

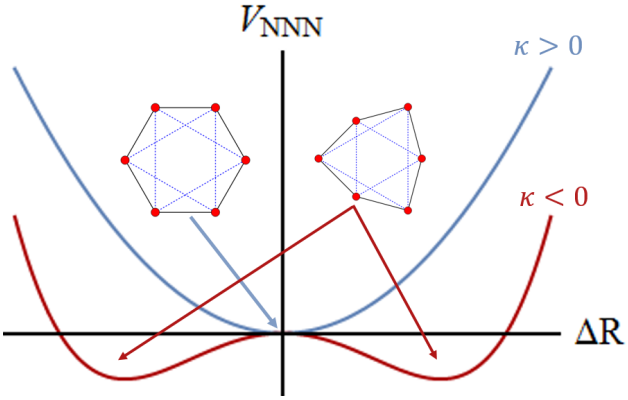

Figure 3.2: The potential energy of next-nearest-neighbor bonds connected by an anharmonic spring as given by Eq. (3.3.9). For $\kappa > 0$, the potential is single-well, so all NNN bonds are the same length – yielding a regular hexagonal cell corresponding to an untwisted kagome lattice. For $\kappa < 0$, the potential is double-well, so the energetically-preferred configuration for the hexagonal cell is one where three NNN bonds are longer than the regular-hexagon NNN bonds, and three NNN bonds are shorter. This yields an irregular hexagonal cell corresponding to a twisted kagome lattice. At zero temperature, this is what governs the structural phase transition between the kagome and twisted kagome lattices.

the NN lattice). Therefore, $\Delta R_{NN} = 0$. Now, the central-force potentials we consider are

$$V_{NN} = \frac{k}{2}(\Delta R)^2 \tag{3.3.8}$$

$$V_{NNN} = \frac{\kappa}{2}(\Delta R)^2 + \frac{g}{4!}(\Delta R)^4 \tag{3.3.9}$$

The NN bond is modeled as a harmonic spring, while the next-nearest-neighbor (NNN) bond is modeled as an anharmonic spring. This is to allow for κ to be negative while still having a bounded potential: $g > 0$. Since $\Delta R_{NN} = 0$, $V_N NN = 0$ at zero temperature. On the other hand, the length of the NNN bonds *do* change as we twist away from the reference state. The total elastic energy in the lattice is then given by

$$H = \sum_{b_i \in NNN} V_{NNN}(\Delta R_i). \tag{3.3.10}$$

For a given twisting angle $-\pi/3 \leq \alpha \leq \pi/3$, three NNN bonds will be longer than the

$\alpha = 0$ untwisted lattice NNN bond length ($a\sqrt{3}$) and three NNN bonds will be shorter:

$$R^{+}_{NNN}(\alpha) = a\sqrt{2 + \cos 2\alpha + \sqrt{3}\sin 2\alpha} = a|\sin\alpha + \sqrt{3}\cos\alpha| \tag{3.3.11}$$

$$R^{-}_{NNN}(\alpha) = a\sqrt{2 + \cos 2\alpha - \sqrt{3}\sin 2\alpha} = a|\sin\alpha - \sqrt{3}\cos\alpha| \tag{3.3.12}$$

Incidentally, the increase and decrease in NNN bond lengths is symmetric only for small twisting angles away from $\alpha = 0$. The change in the NNN length between two states is then given by $\Delta R_{NNN} = R_{NNN}(\alpha) - R_{NNN}(\alpha_0)$; for small $\Delta\alpha \equiv \alpha - \alpha_0$, the results can be expanded in terms of $\Delta\alpha$

$$\begin{aligned}\frac{\Delta R^{\pm}_{NNN}}{a} &= \pm\frac{\sqrt{3}\cos 2\alpha_0 \mp \sin 2\alpha_0}{\sqrt{2 + \cos 2\alpha_0 \pm \sqrt{3}\sin 2\alpha_0}}\Delta\alpha - \frac{1}{2}\sqrt{2 + \cos 2\alpha_0 \pm \sqrt{3}\sin 2\alpha_0}\,\Delta\alpha^2 \\ &\quad \mp \frac{5\sqrt{3}\cos 2\alpha_0 + 4\sqrt{3}\cos 4\alpha_0 \mp 5\sin 2\alpha_0 \pm 4\sin 4\alpha_0 \pm 2\sin 6\alpha_0}{6(2 + \cos 2\alpha_0 \pm \sqrt{3}\sin 2\alpha_0)^{5/2}}\Delta\alpha^3 + \mathcal{O}(\Delta\alpha^4) \\ &= A^{\pm}_1\Delta\alpha - \frac{1}{2}A^{\pm}_2\Delta\alpha^2 - \frac{1}{6}A^{\pm}_3\Delta\alpha^3 + \mathcal{O}(\Delta\alpha^4)\end{aligned} \tag{3.3.13}$$

For $\alpha_0 = 0$, the coefficients are greatly simplified: $A^{\pm}_1 = \pm 1$, $A^{\pm}_2 = \sqrt{3}$, and $A^{\pm}_3 = \pm 1$. We substitute this into our potential and once again do an expansion in terms of $\Delta\alpha$, which yields

$$\begin{aligned}H &= \sum_b \frac{\kappa}{2}(\Delta R_{NNN})^2 + \frac{g}{24}(\Delta R_{NNN})^4 = N\sum_B \frac{\kappa}{2}(\Delta R_{NNN})^2 + \frac{g}{24}(\Delta R_{NNN})^4 \\ &= Na^2\Bigg[\frac{3\kappa}{2}\left((A^{+}_1)^2 + (A^{-}_1)^2\right)\Delta\alpha^2 - \frac{3\kappa}{2}\left(A^{+}_1A^{+}_2 + A^{-}_1A^{-}_2\right)\Delta\alpha^3 \\ &\quad + \left(\frac{3\kappa}{2}\left(\frac{(A^{+}_2)^2 + (A^{-}_2)^2}{4} - \frac{A^{+}_1A^{+}_3 + A^{-}_1A^{-}_3}{3}\right) + \frac{ga^2\left((A^{+}_1)^4 + (A^{-}_1)^4\right)}{8}\right)\Delta\alpha^4 + \mathcal{O}(\Delta\alpha^5)\Bigg]\end{aligned} \tag{3.3.14}$$

Note that, in the first line, b is an index over all NNN bonds in the lattice, where B is an index over only those NNN bonds in a single unit cell. Because the unit cell is a repeating motif in the lattice under periodic boundary conditions, any lattice expression can simply be

computed in the unit cell and then multiplied by the number of unit cells, N. The resultant Hamiltonian is a completely general expression for any α and α_0 such that $\Delta\alpha \ll 1$. As already mentioned, we are interested in the stability of the untwisted kagome lattice, so we take $\alpha_0 = 0$. In this case, $\Delta\alpha = \alpha$, and odd terms vanish, leaving

$$H(\alpha) = Na^2 \left[3\kappa\alpha^2 + \frac{1}{4}(5\kappa + ga^2)\alpha^4 \right]. \tag{3.3.15}$$

Introducing dimensionless couplings

$$\tau \equiv \frac{\kappa}{k}, \quad \lambda \equiv \frac{ga^2}{k}, \tag{3.3.16}$$

we can write a dimensionless Hamiltonian per unit cell,

$$h(\alpha) \equiv \frac{H(\alpha)}{Nka^2} = 3\tau\alpha^2 + \frac{1}{4}(5\tau + \lambda)\alpha^4. \tag{3.3.17}$$

We require λ to be large so that $5\tau + \lambda > 0$ even when $\tau < 0$ and, consequently, the Hamiltonian will have a well-defined minimum.

The extrema, obtained by requiring that $h'(\alpha) = 0$, are

$$\alpha = 0, \qquad \alpha = \pm\sqrt{\frac{-6\tau}{5\tau + \lambda}} \equiv \pm\alpha_0^t. \tag{3.3.18}$$

In order for $\alpha \ll 1$, so that our expansion in small α is justified, $\lambda \gg \tau$ (this is a stronger condition than simply requiring $5\tau+\lambda > 0$). Note that, for $\tau > 0$, $\alpha = 0$ is the stable solution and the latter two are imaginary; for $\tau < 0$, the latter two solutions are the stable solutions and $\alpha = 0$ becomes an unstable equilibrium point (local maximum). Therefore, $\tau = 0$ is the transition point at which the system undergoes a continuous structural transition at $T = 0$; for $\tau > 0$, the untwisted kagome lattice is energetically preferred, whereas for $\tau < 0$, the twisted kagome lattice becomes the preferred state. This is different than the case of the

square lattice transition discussed at the beginning of this chapter, in that there is only a single ground state – the twisted kagome lattice – for $\tau < 0$.

3.4 Finite-temperature free energy calculation

Now that we have obtained the transition point for the structural transition at zero temperature, we want to explore the structural transition at finite temperature. This will allow us to analyze the coupled effect of thermal fluctuations and floppy modes near a point of ostensible instability. The effect of thermal fluctuations on a system can be codified by the introduction of a random displacement field, $\mathbf{u}_l$, which characterizes the instantaneous displacements of lattice site l from its equilibrium position. In this section, we systematically incorporate thermal fluctuations into our lattice theory, expanding the resultant Hamiltonian to second order in $\mathbf{u}$ (we take the fluctuations to be sufficiently small by considering only small temperatures, an assumption that will be validated later). We then integrate out the thermal fluctuations to obtain a free energy in terms of twisting angle α (as in the previous section, we will include α_0 throughout the derivation for full generality, but we will only specifically analyze the $\alpha_0 = 0$ case, as we are considering the stability of the untwisted kagome lattice) and elastic constants τ and λ. We can use the same machinery introduced at the beginning of the previous section, but now the target space must include deformations induced by thermal fluctuations. In order to capture the effect of thermal fluctuations, we define the target space position vector to include the displacement field $\mathbf{u}_l$:

$$\mathbf{R}_l = l_1\mathbf{a}_1(\alpha) + l_2\mathbf{a}_2(\alpha) + \mathbf{d}_{i_l} + \mathbf{u}_l. \tag{3.4.1}$$

Then the bond vectors are given by

$$\mathbf{R}_{0b} = \mathbf{R}_{0l'} - \mathbf{R}_{0l} = \mathbf{l}_b(\alpha_0) + \mathbf{d}_b(\alpha_0) \equiv \mathbf{R}_b^{\alpha_0} \tag{3.4.2}$$

$$\mathbf{R}_b = \mathbf{R}_{l'} - \mathbf{R}_l = \mathbf{l}_b(\alpha) + \mathbf{d}_b(\alpha) + \mathbf{u}_b \equiv \mathbf{R}_b^{\alpha} + \mathbf{u}_b, \tag{3.4.3}$$

where $\mathbf{u}_b \equiv \mathbf{u}_{l'} - \mathbf{u}_l$ has no angular dependence. Note that, for the three intracellular NN bonds, $l_i' = l_i$ and, thus, $\mathbf{l}_b(\alpha) = \mathbf{l}_b(\alpha_0) = 0$.

The length of the bond in the reference state can be expanded for small $\mathbf{u}_b$,

$$\begin{aligned} |\mathbf{R}_b| &= \sqrt{(\mathbf{R}_b^{\alpha} + \mathbf{u}_b) \cdot (\mathbf{R}_b^{\alpha} + \mathbf{u}_b)} = |\mathbf{R}_b^{\alpha}| \sqrt{1 + \frac{2\hat{\mathbf{t}}_b^{\alpha} \cdot \mathbf{u}_b}{|\mathbf{R}_b^{\alpha}|} + \frac{u_b^2}{|\mathbf{R}_b^{\alpha}|^2}} \\ &= |\mathbf{R}_b^{\alpha}| + \hat{\mathbf{t}}_b^{\alpha} \cdot \mathbf{u}_b + \frac{1}{2|\mathbf{R}_b^{\alpha}|} \left(u_b^2 - (\hat{\mathbf{t}}_b^{\alpha} \cdot \mathbf{u}_b)^2 \right) + \mathcal{O}(u_b^3) \\ &= |\mathbf{R}_b^{\alpha}| + \hat{\mathbf{t}}_b^{\alpha} \cdot \mathbf{u}_b + \frac{1}{2|\mathbf{R}_b^{\alpha}|} \mathbf{u}_b \cdot \left(\mathbf{I} - \hat{\mathbf{t}}_b^{\alpha} \hat{\mathbf{t}}_b^{\alpha} \right) \cdot \mathbf{u}_b + \mathcal{O}(u_b^3), \end{aligned} \tag{3.4.4}$$

where

$$\hat{\mathbf{t}}_b^{\alpha} = \frac{\mathbf{R}_b^{\alpha}}{|\mathbf{R}_b^{\alpha}|} \tag{3.4.5}$$

is the unit vector pointing along the bond b where the kagome lattice has been twisted by an angle α (but without considering the random displacements due to thermal fluctuations). Then the change in bond length due to uniform twisting and thermal fluctuations is

$$|\mathbf{R}_b| - |\mathbf{R}_{0b}| = |\mathbf{R}_b^{\alpha}| - |\mathbf{R}_b^{\alpha_0}| + \hat{\mathbf{t}}_b^{\alpha} \cdot \mathbf{u}_b + \frac{1}{2|\mathbf{R}_b^{\alpha}|} \mathbf{u}_b \cdot \left(\mathbf{I} - \hat{\mathbf{t}}_b^{\alpha} \hat{\mathbf{t}}_b^{\alpha} \right) \cdot \mathbf{u}_b + \mathcal{O}(u_b^3). \tag{3.4.6}$$

Next, we expand the potential of a bond in terms of small $\mathbf{u}_b$:

$$\begin{aligned}
&V_b(|\mathbf{R}_b| - |\mathbf{R}_{0b}|) \\
&\quad = V_b(|\mathbf{R}_b^\alpha| - |\mathbf{R}_b^{\alpha_0}|) + V_b'(|\mathbf{R}_b^\alpha| - |\mathbf{R}_b^{\alpha_0}|)\left(\hat{\mathbf{t}}_b^\alpha \cdot \mathbf{u}_b + \frac{1}{2|\mathbf{R}_b^\alpha|}\mathbf{u}_b \cdot \left(\mathbf{I} - \hat{\mathbf{t}}_b^\alpha \hat{\mathbf{t}}_b^\alpha\right) \cdot \mathbf{u}_b\right) \\
&\qquad\qquad + \frac{1}{2}V_b''(|\mathbf{R}_b^\alpha| - |\mathbf{R}_b^{\alpha_0}|)(\hat{\mathbf{t}}_b^\alpha \cdot \mathbf{u}_b)^2 + \mathcal{O}(u_b^3) \\
&\quad = V_{b\alpha} + V_{b\alpha}'\left(\hat{\mathbf{t}}_b^\alpha \cdot \mathbf{u}_b + \frac{1}{2|\mathbf{R}_b^\alpha|}\mathbf{u}_b \cdot \left(\mathbf{I} - \hat{\mathbf{t}}_b^\alpha \hat{\mathbf{t}}_b^\alpha\right) \cdot \mathbf{u}_b\right) + \frac{V_{b\alpha}''}{2}(\hat{\mathbf{t}}_b^\alpha \cdot \mathbf{u}_b)^2 + \mathcal{O}(u_b^3) \\
&\quad = V_{b\alpha} + V_{b\alpha}'\hat{\mathbf{t}}_b^\alpha \cdot \mathbf{u}_b + \mathbf{u}_b \cdot \left[\frac{V_{b\alpha}'}{2|\mathbf{R}_b^\alpha|}\mathbf{I} + \left(\frac{V_{b\alpha}''}{2} - \frac{V_{b\alpha}'}{2|\mathbf{R}_b^\alpha|}\right)\hat{\mathbf{t}}_b^\alpha \hat{\mathbf{t}}_b^\alpha\right] \cdot \mathbf{u}_b + \mathcal{O}(u_b^3) \qquad (3.4.7)
\end{aligned}$$

where $V_{b\alpha} \equiv V_b(|\mathbf{R}_b^\alpha| - |\mathbf{R}_b^{\alpha_0}|)$, $V_{b\alpha}' \equiv V_b'(|\mathbf{R}_b^\alpha| - |\mathbf{R}_b^{\alpha_0}|)$, and $V_{b\alpha}'' \equiv V_b''(|\mathbf{R}_b^\alpha| - |\mathbf{R}_b^{\alpha_0}|)$. The linear term, $\sum_b V_{b\alpha}'\hat{\mathbf{t}}_b^\alpha \cdot \mathbf{u}_b$ vanishes, as it corresponds to the total force on each site, which is equal to zero for any given twisting angle. Thus, the Hamiltonian (exact to $\mathcal{O}(u_b^2)$), becomes $H = H^{(0)} + H^{(2)}$, with

$$H^{(0)} = \sum_b V_{b\alpha} \qquad (3.4.8)$$

and

$$H^{(2)} = \sum_b \mathbf{u}_b \cdot \left[\frac{V_{b\alpha}'}{2|\mathbf{R}_b^\alpha|}\mathbf{I} + \left(\frac{V_{b\alpha}''}{2} - \frac{V_{b\alpha}'}{2|\mathbf{R}_b^\alpha|}\right)\hat{\mathbf{t}}_b^\alpha \hat{\mathbf{t}}_b^\alpha\right] \cdot \mathbf{u}_b \equiv \frac{1}{2}\sum_b \mathbf{u}_b \cdot \mathbf{A}_b \cdot \mathbf{u}_b, \qquad (3.4.9)$$

where

$$\mathbf{A}_b \equiv \frac{V_{b\alpha}'}{|\mathbf{R}_b^\alpha|}\mathbf{I} + \left(V_{b\alpha}'' - \frac{V_{b\alpha}'}{|\mathbf{R}_b^\alpha|}\right)\hat{\mathbf{t}}_b^\alpha \hat{\mathbf{t}}_b^\alpha \qquad (3.4.10)$$

Note that $\sum_b$ is a summation over all bonds in the lattice:

$$\sum_b = \sum_l \sum_{l'}, \qquad (3.4.11)$$

where, for a fixed lattice site l, l' indexes all the lattice sites connected to l by a bond. Thus, for a given lattice site l, we sum over all lattice sites l' that are connected to l by a bond.

Writing the Hamiltonian in terms of individual lattice site displacements,

$$H^{(2)} = \frac{1}{2}\sum_{l}\sum_{l'}(\mathbf{u}_l - \mathbf{u}_{l'})\cdot\mathbf{A}_{l,l'}\cdot(\mathbf{u}_l - \mathbf{u}_{l'}) \tag{3.4.12}$$

$$= \frac{1}{2}\sum_{L}\sum_{l}\sum_{l'}(\mathbf{u}_l - \mathbf{u}_{l'})\cdot\mathbf{A}_{l,l'}\cdot(\mathbf{u}_l - \mathbf{u}_{l'}) \tag{3.4.13}$$

In the second equation, L indexes the unit cells, l indexes the lattice sites in the unit cells ($l \in \{1,2,3\}$) and l' indexes all lattice sites connected by bounds to the lattice sites in the unit cell ($l' \in B(l,l')$).

In order to integrate out the displacement field, it is most convenient to transform to momentum space, where the resultant dynamical matrix will be block diagonal. Writing the displacement vector of site l in momentum space,

$$\mathbf{u}_l = \frac{1}{V}\sum_{\mathbf{q}\in 1BZ} e^{i\mathbf{q}\cdot\mathbf{R}_{L_l}}\mathbf{u}_{i_l,q}, \tag{3.4.14}$$

where $\mathbf{R}_{L_l}$ is the position of the unit cell containing lattice site l and $i_l \in \{1,2,3\}$ indexes the basis sites in a unit cell. Thus,

$$H^{(2)} = \frac{1}{2V^2}\sum_{L}\sum_{l}\sum_{l'}\sum_{\mathbf{q},\mathbf{q}'\in 1BZ}\left(e^{i\mathbf{q}\cdot\mathbf{R}_{L_l}}\mathbf{u}_{i_l,q} - e^{i\mathbf{q}\cdot\mathbf{R}_{L_{l'}}}\mathbf{u}_{i_{l'},q}\right)\cdot\mathbf{A}_{l,l'}\cdot\left(e^{i\mathbf{q}'\cdot\mathbf{R}_{L_l}}\mathbf{u}_{i_l,q'} - e^{i\mathbf{q}'\cdot\mathbf{R}_{L_{l'}}}\mathbf{u}_{i_{l'},q'}\right) \tag{3.4.15}$$

$$= \frac{1}{2V^2}\sum_{L}\sum_{l}\sum_{l'}\sum_{\mathbf{q},\mathbf{q}'\in 1BZ} e^{i(\mathbf{q}+\mathbf{q}')\cdot\mathbf{R}_{L_l}}\left(\mathbf{u}_{i_l,q} - e^{i\mathbf{q}\cdot\mathbf{l}_B}\mathbf{u}_{i_{l'},q}\right)\cdot\mathbf{A}_{l,l'}\cdot\left(\mathbf{u}_{i_l,q'} - e^{i\mathbf{q}'\cdot\mathbf{l}_B}\mathbf{u}_{i_{l'},q'}\right) \tag{3.4.16}$$

$$= \frac{1}{2V^2}\sum_{\mathbf{q},\mathbf{q}'\in 1BZ}\sum_{L} e^{i(\mathbf{q}+\mathbf{q}')\cdot\mathbf{R}_L}\sum_{l}\sum_{l'}\left(\mathbf{u}_{i_l,q} - e^{i\mathbf{q}\cdot\mathbf{l}_B}\mathbf{u}_{i_{l'},q}\right)\cdot\mathbf{A}_{l,l'}\cdot\left(\mathbf{u}_{i_l,q'} - e^{i\mathbf{q}'\cdot\mathbf{l}_B}\mathbf{u}_{i_{l'},q'}\right) \tag{3.4.17}$$

$$= \frac{1}{2Vv}\sum_{\mathbf{q}\in 1BZ}\sum_{l,l'\in B}\left(\mathbf{u}_{i_l,q} - e^{i\mathbf{q}\cdot\mathbf{l}_B}\mathbf{u}_{i_{l'},q}\right)\cdot\mathbf{A}_B\cdot\left(\mathbf{u}_{i_l,-q} - e^{-i\mathbf{q}\cdot\mathbf{l}_B}\mathbf{u}_{i_{l'},-q}\right). \tag{3.4.18}$$

In the second equality, we have written $\mathbf{R}_{L_{l'}} = \mathbf{R}_{L_l} + \mathbf{l}_B$, where $\mathbf{l}_B = (l_1' - l_1)\mathbf{a}_1(\alpha) +$

$(l_2' - l_2)\mathbf{a}_2(\alpha)$ is the lattice vector between the unit cell containing lattice l and the unit cell containing lattice site l'. Note that $\mathbf{l}_B = 0$ for the three intra-cellular NN bonds. In the third equality, we observe that, if we index all bonds associated with a single unit cell by B, such that $(l, l') \in B$, only $\mathbf{R}_L$ varies from one unit cell to the next (also, $\mathbf{R}_{L_l} = \mathbf{R}_L \ \forall l$, since l indexes the basis sites of a single unit cell) – all other quantities are translationally invariant between unit cells. Thus, we can sum over all lattice sites, L, and use

$$\sum_L e^{i(\mathbf{q}+\mathbf{q}')\cdot\mathbf{R}_L} = N\delta_{\mathbf{q},\mathbf{q}'}, \tag{3.4.19}$$

where N is the number of unit cells in the lattice, to yield the final equality.

Finally, since there are 3 basis sites, $i_l \in \{1, 2, 3\}$. Therefore, we can consolidate the two-dimensional displacement vectors into a single six-dimensional vector, $\mathbf{u_q}$:

$$\mathbf{u_q} = (\mathbf{u}_{1,\mathbf{q}}, \mathbf{u}_{2,\mathbf{q}}, \mathbf{u}_{3,\mathbf{q}}) = (u_{1x}, u_{1y}, u_{2x}, u_{2y}, u_{3x}, u_{3y}), \tag{3.4.20}$$

where we have dropped the q for notational convenience. This will allow us to write the Hamiltonian concisely as

$$H^{(2)} = \frac{1}{2Vv} \sum_{\mathbf{q}\in 1BZ} \mathbf{u_q} \cdot \mathbf{D_q} \cdot \mathbf{u_{-q}}, \tag{3.4.21}$$

where v is the volume of the unit cell in the direct lattice, and $\mathbf{D_q}$ can be either the full 6×6 dynamical matrix or the effective/reduced 3×3 dynamical matrix (see the end of this section for relevant discussion).

Then the partition function is given by

$$Z = \int \mathcal{D}\mathbf{u}\ e^{-\beta H(u)} = \frac{1}{A^N} e^{-\beta H^{(0)}} \prod_{\mathbf{q}\in 1BZ} \int d^n u_q \exp\left[-\frac{\beta}{2Vv} \mathbf{u_q} \cdot \mathbf{D_q} \cdot \mathbf{u_{-q}}\right], \tag{3.4.22}$$

where the integration measure is $\mathcal{D}\mathbf{u} = A^{-N} \prod_q d^n u_q$ with N equal to the number of lattice

sites and $n \in \{3, 6\}$, depending on the dimension of the dynamical matrix. Thus, we obtain

$$Z = e^{-\beta H^{(0)}} \prod_{\mathbf{q}} \sqrt{\frac{(2\pi)^n}{A^2(\beta k/Vv)^n \det \widetilde{\mathbf{D}}_{\mathbf{q}}}}, \tag{3.4.23}$$

where $\widetilde{\mathbf{D}}_{\mathbf{q}} \equiv \mathbf{D}_{\mathbf{q}}/k$ is the dimensionless dynamical matrix. This gives us an expression for the free energy of the system:

$$F = H_0 + \frac{T}{2} \sum_{\mathbf{q} \in 1BZ} \ln \det \widetilde{\mathbf{D}}_{\mathbf{q}} - \frac{n}{2} T \sum_{q} \ln \frac{2\pi TVv}{kA^{2/n}}. \tag{3.4.24}$$

We have not yet discussed the specific form of the dynamical matrix, which depends on the form of the potentials used for the bonds. Of course, we are still modeling our lattice bonds using Eqs. (3.3.8) and (3.3.9). For the complete dynamical matrix, which includes the NN and NNN potentials as well as dependence on both α and α_0, each entry in the matrix is very lengthy and is not very illuminating. See App. B for the complete NN dynamical matrix expression as a function of twist angle α (we take $\alpha_0 = 0$, as usual). It is also useful to reduce the dimensionality of the dynamical matrix; from the phonon spectra of the kagome and twisted kagome lattices (Fig. 3.3, we see that there are three high-energy optical branches that are "frozen out". Thus, we can integrate out those higher modes by requiring that they will always be in equilibrium, as determined by Hamiltonian. The result is a 3×3 effective dynamical matrix. More details of this process can be found in App. C.

3.4.1 Asymptotic form of the free energy

In this section, we will derive an asymptotic form of the free energy that is valid for $\tau, \alpha, \lambda\alpha^2 \ll 1$. In this regime, the free energy is dominated by the lowest mode, as is illustrated in the phonon spectra in Fig. 3.3. This allows us to produce an analytic asymptotic theory that can be used to analyze the twisted-untwisted phase transition.

For large lattices, the spacing between modes in the first Brillouin zone becomes in-

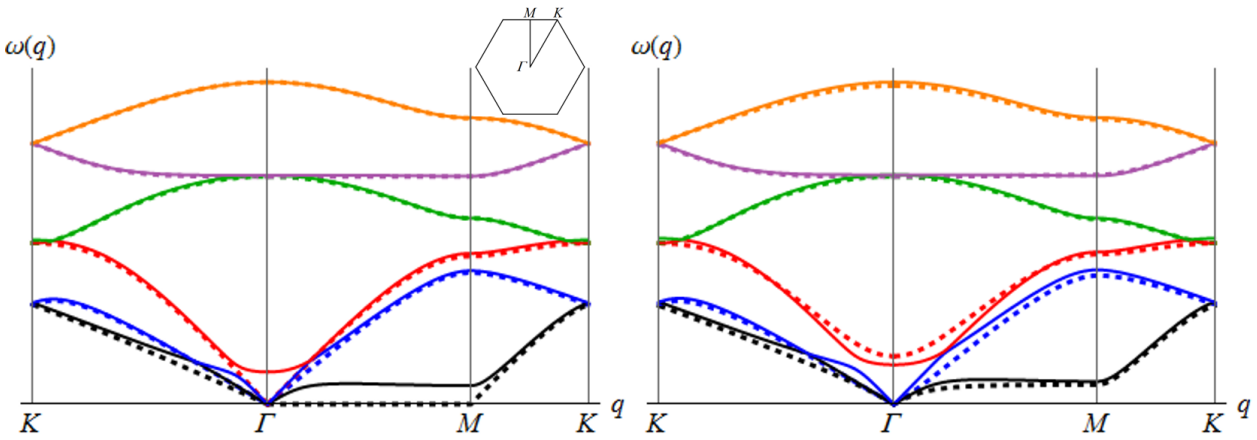

Figure 3.3: (Left) Complete phonon spectrum for the untwisted kagome lattice. Dashed lines depict frequencies at $\tau = 0$ and solid lines at $\tau = 0.01$. The inset shows the first Brillouin zone with high symmetry points Γ, M, and K indicated. There is a line of floppy modes along ΓM when $\tau = 0$ (corresponding to no NNN bonds) that are lifted to finite frequency values for all $\mathbf{q} \neq 0$ for $\tau = 0.01$. (Right) Complete phonon spectrum for the twisted kagome lattice. Dashed lines depict frequencies at $\tau = 0, \lambda = 0, \alpha = 0.15$ (NN lattice) and $\tau = 0.01, \lambda = 100, \alpha = 0.01$ (NNN lattice). Note that the two twisted kagome spectra are relatively similar, though the inclusion of the anharmonic term in the NNN potential is coupled with α necessarily being small. The value of the ω plateau for the lowest mode is well approximated by the value at M given in Eq. (3.4.30).

creasingly small and, ultimately, we can replace the summation in the term involving the dynamical matrix in Eq. (3.4.24) with an integral, using the Poisson summation formula:

$$\frac{1}{V}\sum_{\mathbf{k}} \mathbf{M}(\mathbf{k}) \to \frac{1}{(2\pi)^d}\int d^d k\, \mathbf{M}(\mathbf{k}). \tag{3.4.25}$$

Recall that the volume of the reciprocal lattice primitive cell is given by

$$v_0 = \frac{(2\pi)^d}{v} = \frac{(2\pi)^d N}{V}, \tag{3.4.26}$$

where $v = 2\sqrt{3}a^2 \cos^2\alpha$ is the volume of the direct lattice primitive cell. Thus,

$$v_0 = \frac{2\pi^2}{\sqrt{3}a^2\cos^2\alpha} \tag{3.4.27}$$

and

$$\frac{V}{(2\pi)^d} = \frac{N}{v_0}. \tag{3.4.28}$$

Then

$$\sum_{\mathbf{q}\in 1BZ} \ln\det \widetilde{\mathbf{D}}_{\mathbf{q}} = \frac{V}{(2\pi)^2} \int\limits_{\mathbf{q}\in 1BZ} d^2q \, \ln\det \widetilde{\mathbf{D}}_{\mathbf{q}} = \frac{N}{v_0} \int d^2q \, \ln\det \widetilde{\mathbf{D}}_{\mathbf{q}} \tag{3.4.29}$$

In terms of its eigenvalues, ω_i^2, $\det \widetilde{\mathbf{D}}_{\mathbf{q}} = \omega_1^2\omega_2^2\omega_3^2$, so that $\ln\det \widetilde{\mathbf{D}}_{\mathbf{q}} = \ln\omega_1^2 + \ln\omega_2^2 + \ln\omega_3^2$. Therefore, the integral will be dominated by the near-floppy modes, with a frequency close to zero. The phonon spectrum of the lowest mode of the NN kagome lattice illustrates that there are three symmetry-equivalent lines of zero modes traversing the 1BZ from M to Γ to M; for small values of τ and $\lambda\alpha^2$, the zero modes (other than the two trivial translation modes, of course) are only slightly lifted. The resultant plateau can be approximated, to lowest order in τ and α^2, by the value of the mode at M:

$$\omega_{1\|}^2 = 2\tau + (1+\lambda)\,\alpha^2. \tag{3.4.30}$$

Notice from the form of the expression, which turns out to be valid for both the full 6×6 and the effective 3×3 dynamical matrices, that the line of zero modes is lifted by a non-zero rotation of angle α even when the dimensionless quartic coefficient, λ, is identically zero. Close to the slightly-lifted lines and perpendicular to them, the lowest mode rises quadratically and has the form

$$\omega_1^2 = \omega_{1\|}^2 + \frac{3}{4}q_\perp^2. \tag{3.4.31}$$

Thus,

$$\frac{N}{v_0} \int\limits_{\mathbf{q}\in 1BZ} d^2q \, \ln\det \widetilde{\mathbf{D}}_{\mathbf{q}} \approx \frac{6N}{v_0} \int\limits_0^{\frac{\pi}{\sqrt{3}\cos\alpha}} dq_\| \int\limits_{-q_\|/\sqrt{3}}^{q_\|/\sqrt{3}} dq_\perp \, \ln\left[\omega_{1\|}^2 + \frac{3}{4}q_\perp^2\right]. \tag{3.4.32}$$

To lowest order in τ and α^2, the result of this integral is

$$\frac{N}{v_0}\int\limits_{\mathbf{q}\in 1BZ} d^2q\, \ln\det \widetilde{\mathbf{D}}_{\mathbf{q}} \approx N\left(\mathcal{C}+4\sqrt{3}\sqrt{2\tau+(1+\lambda)\alpha^2}\right), \tag{3.4.33}$$

where $\mathcal{C}=-3+\ln(\pi^2/12)$.

Thus, the dimensionless free energy per unit cell is

$$f(\alpha)\equiv\frac{F(\alpha)}{Nka^2}=H(\alpha)+\frac{\widetilde{T}}{2}\sum_{\mathbf{q}\in 1BZ}\ln\det\widetilde{\mathbf{D}}_{\mathbf{q}} \tag{3.4.34}$$

$$=3\tau\alpha^2+\frac{1}{4}(5\tau+\lambda)\alpha^4+\widetilde{T}2\sqrt{3}\sqrt{2\tau+(1+\lambda)\alpha^2}, \tag{3.4.35}$$

where we have dropped all terms independent of twisting angle α and introduced a reduced, dimensionless temperature,

$$\widetilde{T}\equiv\frac{T}{ka^2}. \tag{3.4.36}$$

This asymptotic form is a good approximation to the true value of the integral using the full 6×6 dynamical matrix for small values of τ and $\lambda\alpha^2$; see Fig. 3.4. Finally, since $F=H-TS$, it should be apparent that the last term in Eq. 3.4.35 is the entropic contribution.

3.4.2 The stability of the kagome lattice

In order to analyze the structural stability of the untwisted kagome lattice against twisting, we will need to compute the twisting modulus

$$\mathcal{K}(\alpha)\equiv\left.\frac{\partial^2 f}{\partial\alpha^2}\right|_{\alpha=\alpha^*}, \tag{3.4.37}$$

which provides a measure of stiffness of the lattice against twisting at equilibrium values of the twisting angle, α^*. Specifically, for the untwisted kagome lattice, we will want to evaluate

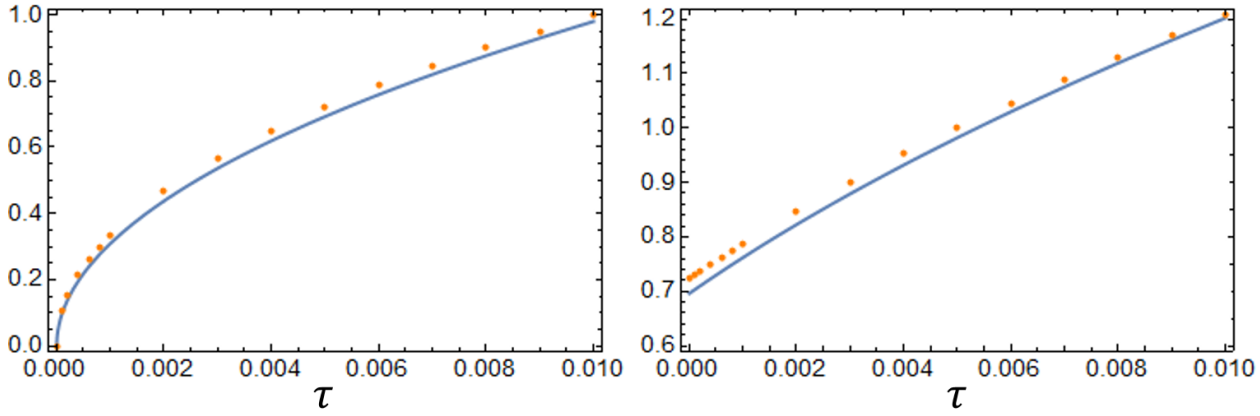

Figure 3.4: Comparisons of the value of the integral of $\ln\det\widetilde{\mathbf{D}}_{\mathbf{q}}/v_0$ over the first Brillouin zone, as computed using two methods: the asymptotic form in Eq. 3.4.33 (blue solid line), and exact values obtained by numerical integration involving the complete dynamical matrix (orange points). (Left) Untwisted kagome lattice, with $\alpha = 0$, $\lambda = 100$; (Right) twisted kagome lattice, with $\alpha = 0.01$, $\lambda = 100$. Both indicate that the asymptotic form is indeed a good analytic approximation for the exact solution.

the twisting modulus at $\alpha = 0$. At zero temperature,

$$\mathcal{K}(\alpha = 0) = 6\tau, \qquad \mathcal{K}(\alpha = \pm\alpha_0^t) = -12\tau. \tag{3.4.38}$$

As expected, there is positive stiffness against twisting away from the untwisted kagome phase ($\alpha = 0$) for $\tau > 0$, and positive stiffness against twisting away from the equilibrium twisted kagome phase ($\alpha = \pm\alpha_0^t$) for $\tau < 0$. For $\tau = 0$, the twisting modulus vanishes in both cases, as there is no energy cost to changing the length of NNN bonds to harmonic order, so the twisting modes are floppy (and this extends to all orders if $\lambda = 0$, as well).

Based on the form of the results in (3.4.38), it is useful to look at the quantity $\mathcal{K}/6$. At finite temperature, this quantity will an effective NNN harmonic coefficient,

$$r \equiv \frac{1}{6}\frac{\partial^2 f}{\partial\alpha^2}\bigg|_{\alpha=\alpha^*}, \tag{3.4.39}$$

where α^* are now equilibrium values of the twisting angle at finite temperature and, in general, are not equal to the equilibrium values obtained at zero temperature. The equilibrium

values are obtained by solving

$$0 = \frac{\partial f}{\partial \alpha} = 6\tau\alpha + (5\tau + \lambda)\alpha^3 + \widetilde{T}\frac{2\sqrt{3}(1+\lambda)\alpha}{\sqrt{2\tau + (1+\lambda)\alpha^2}}. \tag{3.4.40}$$

Even at finite temperature, the untwisted kagome lattice (with $\alpha = 0$) remains an equilibrium solution. Then, for the untwisted phase,

$$r = \tau + \frac{\widetilde{T}}{\sqrt{3}}\frac{1+\lambda}{\sqrt{2\tau}}. \tag{3.4.41}$$

For $\tau < 0$, the effective stiffness is imaginary; in order to rectify this unphysical situation, we use a self-consistent-field approximation where the bare, "tree-level" twisting modulus τ in the phonon Green's function is replaced by its one-loop-order renormalized value. The effect of this in our calculation is to replace τ with r in the entropic contribution to the free energy. Thus, the above equation for r becomes

$$r = \tau + \frac{\widetilde{T}}{\sqrt{3}}\frac{1+\lambda}{\sqrt{2r}}. \tag{3.4.42}$$

Now, for any value of $\tau < 0$, there exists a solution $r > 0$. Since the twisting modulus $\mathcal{K} = 6r > 0$, the untwisted kagome phase is always locally stable (except, of course, at zero temperature). This local stability implies that the transition to the twisted kagome phase must be first order, where the order parameter α will undergo a discontinuous change across the phase boundary determined by

$$\Delta f \equiv f_{\text{tw}} - f_{\text{un}} = 0. \tag{3.4.43}$$

The free energy of the untwisted phase $f_{\text{un}} = 2\sqrt{6}\widetilde{T}\sqrt{r}$, where r is the solution to (3.4.42).

For the twisted phase, the equilibrium twisting angles are determined by solving

$$0 = 6\tau + (5\tau + \lambda)\alpha^2 + \widetilde{T}\frac{2\sqrt{3}(1+\lambda)}{\sqrt{2\tau + (1+\lambda)\alpha^2}}. \tag{3.4.44}$$

The solutions will come as a pair, $\alpha = \pm\alpha_t(\tau, \lambda, \widetilde{T}, r)$. Then the value of r in the twisted phase can be obtained by solving the implicit equation

$$r = \frac{1}{6}\frac{\partial^2 f}{\partial \alpha^2}\bigg|_{\alpha=\alpha_t}, \tag{3.4.45}$$

and f_{tw} is obtained by substituting these solutions into (3.4.35).

In the regime $|\tau| \ll 1 \ll \lambda$, rather simple expressions for the phase boundary and other critical lines can be obtained. In the twisted kagome phase, $r > 0$ solutions to the coupled equations (3.4.44) and (3.4.45) only exist for $\tau < \tau_{c1}$, where

$$\tau_{c1} = -0.6676\left(\lambda\widetilde{T}\right)^{2/3}. \tag{3.4.46}$$

This is where the twisted kagome phase first appears (for decreasing τ or $\widetilde{T}$) as a metastable state, locally stable but with a higher free energy than the untwisted kagome phase. The first-order phase boundary, where $\Delta f = 0$, is given by the equation $\tau = \tau_c$, where

$$\tau_c = -0.9087\left(\lambda\widetilde{T}\right)^{2/3}. \tag{3.4.47}$$

This can be rewritten as $\widetilde{T}_c = 1.1544\lambda^{-1}|\tau|^{3/2}$, which indicates that we are indeed operating in the low-temperature regime, where $\widetilde{T} \sim \widetilde{T}_c \ll |\tau| \ll 1$. Therefore, our assumption of small fluctuations made at the beginning of this analysis was valid.

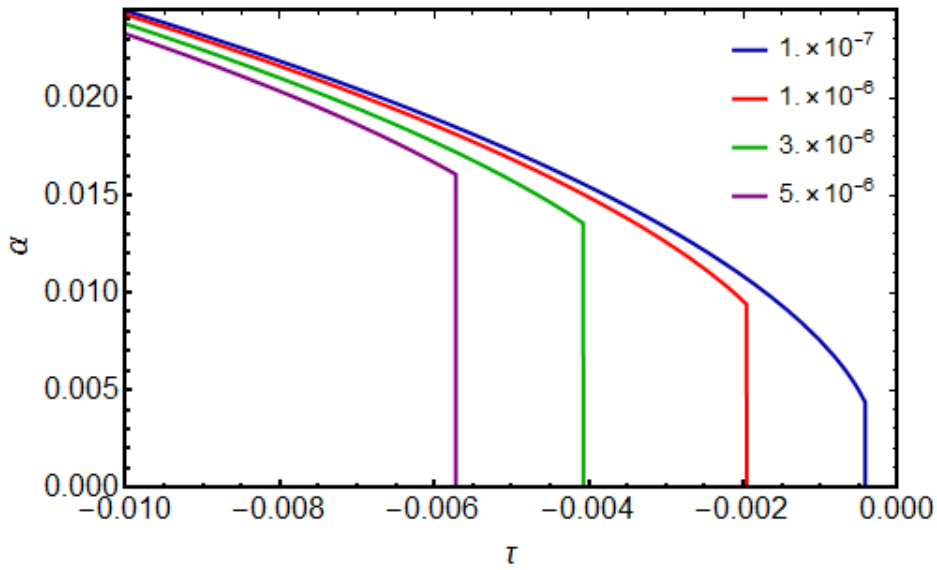

Figure 3.5: Plots of the order parameter, the twisting angle α, as a function of τ for various values of reduced temperature, $\widetilde{T}$ and $\lambda = 100$. The discontinuous jumps in α occur at the transition from the untwisted kagome lattice (where $\alpha = 0$) to the twisted kagome lattice (where $\alpha \neq 0$) and are characteristic of a first-order phase transition.

Along the phase boundary,

$$r_{\mathrm{un},c} = 0.1490 \left(\lambda \widetilde{T}\right)^{2/3} \tag{3.4.48}$$

$$r_{\mathrm{tw},c} = 1.2250 \left(\lambda \widetilde{T}\right)^{2/3}. \tag{3.4.49}$$

Since both are positive, both phases are locally stable at the transition. Furthermore, the order parameter α undergoes a discontinuous jump from zero in the untwisted kagome phase to

$$\alpha_c = 2.0245 \lambda^{-1/6} \widetilde{T}^{1/3} \tag{3.4.50}$$

in the twisted kagome phase (Fig. 3.5). These are all consistent with the first-order nature of the phase transition for $\widetilde{T} > 0$. Finally, note that $\alpha_c \to 0$ as $\widetilde{T} \to 0$, which coincides with the fact that the $\widetilde{T} = 0$ transition is a continuous structural transition.

Looking at the phase diagram (Fig. 3.6), we see that there is a region where $\tau < 0$ but the kagome lattice nevertheless has a lower free energy due to thermal fluctuations. This

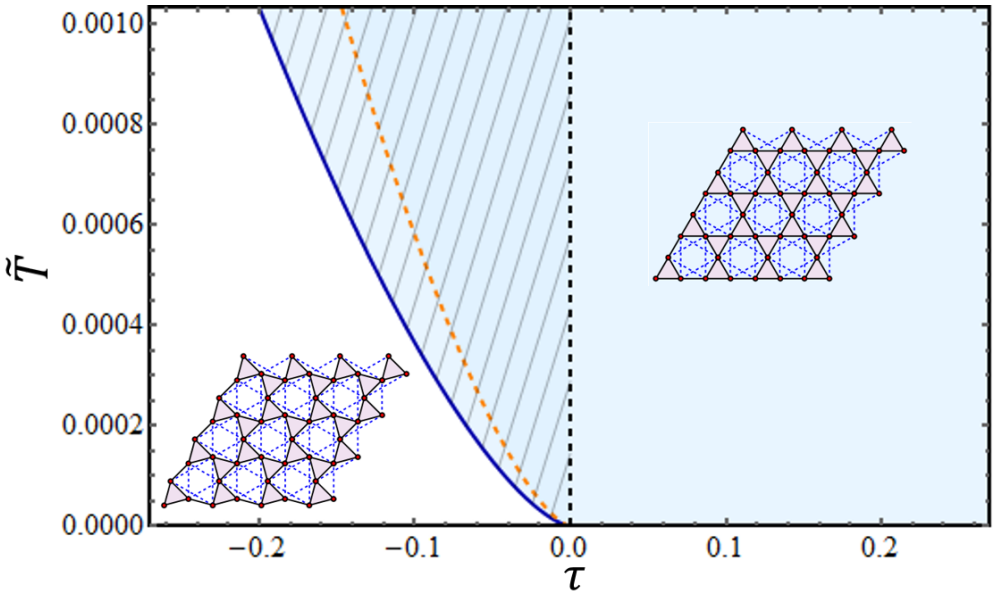

Figure 3.6: The predicted phase diagram for the kagome and twisted kagome lattices. The transition, identified by the solid blue curve, is first order for $T > 0$. The $T = 0$ structural transition is continuous. The orange dashed curve marks where the twisted kagome lattice first appears as a metastable state (for decreasing τ or T). Both critical curves follow $\tau_c \propto -T^{2/3}$. The lined region between $\tau = 0$ and the phase boundary is the region where the kagome lattice is entropically stabilized.

is the region in which the kagome lattice is entropically stabilized – the twisted-untwisted transtion is "delayed" by thermal fluctuations. Ultimately, this is a manifestation of the interplay between floppy modes and thermal fluctuations: the underlying reason that the zero-temperature continuous phase transition has become first order is that the lines of zero modes in the 1BZ in the $\tau \to 0$ limit result in a divergent phonon contribution to the free energy and, thus, the renormalization of the twisting modulus, in a manner analogous to that first explored by Brazovskii in the liquid-to-crystal transition [88].

3.5 Tri-block Janus particles

As we discussed when we first introduced Janus particles, Janus particles have a broad appeal and can be used in a number of different ways for various purposes. Here, we will specifically address their proven versatility in serving as the building blocks for lattice struc-

tures – in particular, open lattices. Triblock Janus particles, which have two attractive patches separated by a central electrostatically-charged band, have already been shown to form two-dimensional lattice structures [45, 46]. When there is no lateral pressure on the system, due to the stabilization of bond angles from a lifting of the potential-well degeneracy ("order-by-disorder") as well as a lack of non-attractive contacts resulting from the open structure of the lattice (both of which will be discussed at length in succeeding sections), the Janus particles are observed to spontaneously form an untwisted kagome lattice. Only with the application of lateral pressure above a minimum threshold value was the close-packed lattice phase observed.

For three-dimensional lattices, a theoretical study exhibited a similar favoring of three-dimensional open structures over the close-packed face-centered cubic lattice [62]. In this case, there are two distinct open lattice topologies, depending on the patch size. For a patch size of 35° or larger (in the context of Janus particles, patch size refers to the angular radius of the circular patch), the patch size is only large enough to support bonds with three neighboring particles per patch, which corresponds to either a pyrochlore or hexagonal tetrastack lattice (the difference is that the successive layers in the latter lattice are twisted by 60°). Above a patch size of 45°, each patch can support four bonds, which results in a perovskite pattice. Again, at low pressures, the open lattices are favored, and it is only with an increase in the pressure (or a decrease in temperature) that the close-packed lattice is obtained. In both the two- and three-dimensional cases, we see the effect of entropy to stabilize the open lattice against mechanical instability as well as to favor open structures over their energetically-equivalent close-packed counterparts.

Thus, it is worthwhile to study the possibility of the self-assembly of the *twisted* kagome lattice from triblock Janus particles restricted to binding in two dimensions (Fig. 3.7). As we will see, even though the two structures are isoenergetic, because of orientational entropy favoring angles between bonds that are consistent with the untwisted kagome lattice, it is not possible to obtain the twisted kagome lattice using regular triblock Janus particles. Instead,

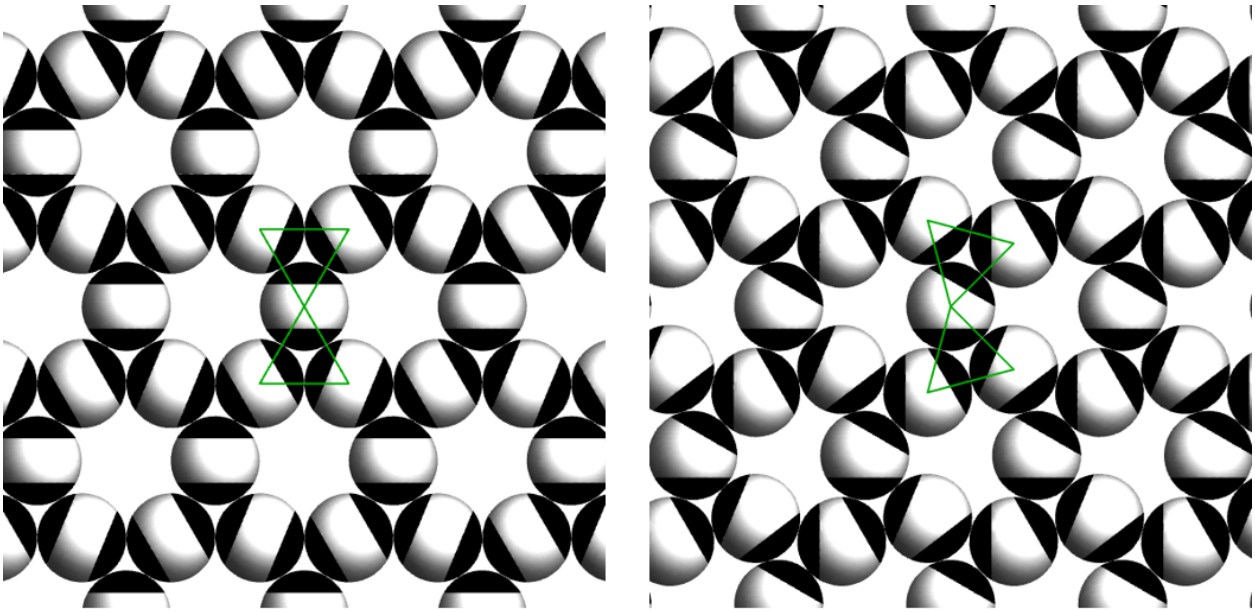

Figure 3.7: Examples of isoenergetic open structures formed by Janus particles. (Left) The kagome lattice, with an angle between triangles (outlined in green) of 120°, formed by Janus particles with non-offset patches. (Right) The twisted kagome lattice, with an angles between triangles deviating from 120°, formed by Janus particles with offset patches. Note that while Janus particles with offset patches can potentially form a kagome lattice, depending on the patch size, offset angle, and temperature, Janus particles with non-offset patches cannot form a twisted kagome lattice, as angles that deviate from 120° are entropically disfavored.

a modification has to be made: one of the patches must be made offset by an angle with respect to the other. After reviewing the derivation of the effective Hamiltonian that is valid for any Janus particles that adhere to a few well-founded assumptions, as initially formulated in [61], we will examine what conditions are necessary for the creation of a twisted kagome lattice.

3.5.1 Derivation of the effective Hamiltonian for Janus particles

The equilibrium statistical mechanics of a set of anisotropic particles such as Janus particles can be described using the partition function

$$Z = \int \prod_j \mathrm{d}\mathbf{r}_j \mathrm{d}\hat{\mathbf{n}}_j \, \exp\left[-\frac{H\left(\{\mathbf{r}_i, \hat{\mathbf{n}}_\mathbf{i}\}\right)}{k_B T}\right], \tag{3.5.1}$$

where the Hamiltonian H depends on the positions $\mathbf{r}_j$ and orientations $\hat{\mathbf{n}}_j$ of all the particles, k_B is the Boltzmann constant, and T is the temperature. For a three-dimensional particle with rotational symmetry around its orientation axis, $\hat{\mathbf{n}}_j$, two parameters – polar angle θ and azimuthal angle φ – are sufficient to fully describe its orientation; for a completely general particle, a third angle ψ is needed.

We consider spherical triblock Janus particles of diameter a with two spherical-cap-shaped attractive patches on (or near) opposite poles separated by a repulsive band such that the particles experience a short-range attraction when the particles are touching and oriented in such a way that their patches have finite overlap and hard-core repulsion when their separation is equal to a diameter. Experimentally, such particles can be fabricated as in [45, 89] via treatments that create two hydrophobic patches and an electrically-charged band, resulting in hydrophobic attraction when placed in a salt solution.

In its most general form, the Hamiltonian of a system of these so-called patchy particles consists of pairwise potential energies of the form

$$V\left(\mathbf{r}_i, \hat{\mathbf{n}}_i, \mathbf{r}_j, \hat{\mathbf{n}}_k\right) = \int \mathrm{d}\Omega_i \mathrm{d}\Omega_j \, \mathcal{V}\left(\hat{\mathbf{n}}_i, \hat{\mathbf{n}}_j, \hat{\mathbf{m}}_i, \hat{\mathbf{m}}_j, \left|\left(\mathbf{r}_i + a\hat{\mathbf{m}}_i/2\right) - \left(\mathbf{r}_j + a\hat{\mathbf{m}}_j/2\right)\right|\right), \qquad (3.5.2)$$

where the potential energy between two patchy particles is equal to the integral of interactions v between all pairings of surface elements between the two particles over the solid angles of both particles. In this expression, $\hat{\mathbf{m}}_i$ and $\hat{\mathbf{m}}_j$ are unit vectors pointing in the directions of the surface elements, and $\left|\left(\mathbf{r}_i + a\hat{\mathbf{m}}_i/2\right) - \left(\mathbf{r}_j + a\hat{\mathbf{m}}_j/2\right)\right|$ is the distance between them.

Eq. (3.5.2) is quite an imposing expression, but we can make a series of assumptions that is well-suited to systems of colloidal patchy particles in order to simplify the calculation of the Hamiltonian. First, we postulate that interactions between surface elements are very short-ranged – hence, the particles must be nearly touching in order to experience an interaction. Furthermore, the integral in (3.5.2) will be dominated by the interaction between the closest pairs of surface elements. For spherical particles, the closest pair corresponds to the two

surface elements crossed by the line joining the centers of the two particles, so that

$$V\left(\mathbf{r}_i, \hat{\mathbf{n}}_i, \mathbf{r}_j, \hat{\mathbf{n}}_k\right) = \mathcal{V}\left(\hat{\mathbf{n}}_i, \hat{\mathbf{n}}_j, \hat{\mathbf{e}}_{ij}, -\hat{\mathbf{e}}_{ij}, \left|\left(\mathbf{r}_i + a\hat{\mathbf{e}}_{ij}/2\right) - \left(\mathbf{r}_j - a\hat{\mathbf{e}}_{ij}/2\right)\right|\right), \tag{3.5.3}$$

where $\hat{\mathbf{e}}_{ij}$ is the unit vector lying along the line joining the centers.

Second, we need only consider small fluctuations around the equilibrium lattice configuration. This is due to the fact that the potential well of the attractive patches is relatively deep compared to thermal energy ($\sim 10k_BT$, as determined in [45]), and the boundaries of the well are quite sharply defined by the extent of the attractive patches, so thermal fluctuations will not tend to break nearest-neighbor bonds radially or rotationally. Thus, for a given lattice of patchy particles, which will have both *attractive bonds*, where particles contact each other through their overlapping attractive patches, and *non-attractive bonds*, where particles are forced to contact each other outside of their attractive patches due to the lattice structure, any configurations of particle orientations that break any attractive bonds will have negligible Boltzmann weight. Therefore, the pairwise potential can be simplified even further. Attractive bonds have the form

$$V\left(\mathbf{r}_i, \hat{\mathbf{n}}_i, \mathbf{r}_j, \hat{\mathbf{n}}_k\right) = \mathcal{V}_a\left(\left|\mathbf{r}_i - \mathbf{r}_j\right|\right) w\left(\hat{\mathbf{e}}_{ij}, \hat{\mathbf{n}}_i\right) w\left(-\hat{\mathbf{e}}_{ij}, \hat{\mathbf{n}}_j\right), \tag{3.5.4}$$

where $\mathcal{V}_a$ is the central-force interaction with three regimes: hard-core repulsion for $|\mathbf{r}_i - \mathbf{r}_j| < a$; attraction over a small distance, $a < |\mathbf{r}_i - \mathbf{r}_j| < a + \delta$, where $\delta \ll a$; and vanishing interaction for $|\mathbf{r}_i - \mathbf{r}_j| > a + \delta$. The weight factors, given by

$$w\left(\hat{\mathbf{e}}_{ij}, \hat{\mathbf{n}}_i\right) = \begin{cases} 1 & \text{if } \hat{\mathbf{e}}_{ij} \text{ passes through the attractive patch of particle } i \\ \infty & \text{otherwise,} \end{cases} \tag{3.5.5}$$

ensure that only unbroken attractive bonds contribute to the Boltzmann factor. Because a non-attractive contact will not turn into an attractive contact unless other attractive bonds

are broken, the potential for a non-attractive bond is simply $V\left(\mathbf{r}_i, \hat{\mathbf{n}}_i, \mathbf{r}_j, \hat{\mathbf{n}}_k\right) = \mathcal{V}_r\left(|\mathbf{r}_i - \mathbf{r}_j|\right)$, where $\mathcal{V}_r$ only entails hard-core repulsion for $|\mathbf{r}_i - \mathbf{r}_j| < a$ and vanishes otherwise.

Note that the weight factors w for a particular particle only depend on the directions of the bonds (which, in turn, only depend on the set of particle positions $\{\mathbf{r}_i\}$) and the orientation of *that* particle. Any orientations of that particle that result in broken attractive bonds will set $w \to \infty$, yielding a zero Boltzmann weight for that orientation. This happily allows for the orientational degrees of freedom of different particles to be completely decoupled. More explicitly, the partition function in (3.5.1) becomes

$$Z = \int \prod_j \mathrm{d}\mathbf{r}_j \mathrm{d}\hat{\mathbf{n}}_j \, \exp\left[-\frac{1}{k_B T} \sum_{\langle mn \rangle} V\left(\mathbf{r}_m, \hat{\mathbf{n}}_\mathbf{m}, \mathbf{r}_n, \hat{\mathbf{n}}_\mathbf{n}\right)\right] \tag{3.5.6}$$

$$= \int \prod_j \mathrm{d}\mathbf{r}_j \mathrm{d}\hat{\mathbf{n}}_j \, \exp\left[-\frac{1}{k_B T}\left(\sum_{\langle mn \rangle_a} \mathcal{V}_a\left(|\mathbf{r}_i - \mathbf{r}_j|\right) w\left(\hat{\mathbf{e}}_{mn}, \hat{\mathbf{n}}_m\right) w\left(-\hat{\mathbf{e}}_{mn}, \hat{\mathbf{n}}_n\right) + \sum_{\langle mn \rangle_r} \mathcal{V}_r\left(|\mathbf{r}_i - \mathbf{r}_j|\right)\right)\right] \tag{3.5.7}$$

$$= \int \prod_j \mathrm{d}\mathbf{r}_j \mathrm{d}\hat{\mathbf{n}}_j \Psi_j\left(\{\mathbf{r}_i\}, \hat{\mathbf{n}}_j\right) \exp\left[-\frac{H_{\mathrm{CF}}\left(\{\mathbf{r}_i\}\right)}{k_B T}\right], \tag{3.5.8}$$

where the sum in the first line is over all nearest-neighbor bonds $\langle mn \rangle$, and the sums in the second line are over all nearest-neighbor attractive $\langle mn \rangle_a$ and non-attractive $\langle mn \rangle_r$ bonds. In the final line, the particle orientations have been decoupled: the factor $\Psi_j\left(\{\mathbf{r}_i\}, \hat{\mathbf{n}}_j\right) = 1$ if all of the attractive bonds of particle j remain within its attractive patches for a given orientation $\hat{\mathbf{n}}_j$, and vanishes if any of the attractive bonds are broken. The remaining central-force portion of the Hamiltonian depends only on the positions of the particles,

$$H_{\mathrm{CF}}\left(\{\mathbf{r}_i\}\right) = \sum_{\langle mn \rangle_a} \mathcal{V}_a\left(|\mathbf{r}_i - \mathbf{r}_j|\right) + \sum_{\langle mn \rangle_r} \mathcal{V}_r\left(|\mathbf{r}_i - \mathbf{r}_j|\right). \tag{3.5.9}$$

Because of the decoupling of orientations, we can integrate out the orientational degrees

of freedom of each particle individually, resulting in a degeneracy factor

$$\Omega_j\left(\{\mathbf{r}_i\}\right) = \int \mathrm{d}\hat{\mathbf{n}}_j\, \Psi_j\left(\{\mathbf{r}_i\}, \hat{\mathbf{n}}_j\right) \tag{3.5.10}$$

that is proportional to the number of allowed orientations – all of which share the same potential energy, due to the flatness of the attractive patches' potential well. Therefore, we can define an orientational entropy for a particle,

$$s_j = k_B \ln \Omega_j \tag{3.5.11}$$

so that the partition function can ultimately be written as

$$Z = \int \prod_j \mathrm{d}\mathbf{r}_j\, \exp\left[-\frac{H_{\mathrm{eff}}\left(\{\mathbf{r}_i\}\right)}{k_B T}\right], \tag{3.5.12}$$

where the effective Hamiltonian depends only on particle positions,

$$H_{\mathrm{eff}}\left(\{\mathbf{r}_i\}\right) = H_{\mathrm{CF}}\left(\{\mathbf{r}_i\}\right) - T\sum_j s_j\left(\{\mathbf{r}_i\}\right). \tag{3.5.13}$$

3.5.2 Two-dimensional triblock Janus particles

It is instructive to begin with the case of two-dimensional disk-shaped particles, with orientations specified by a single angle, θ_i, confined to a plane so that they assemble into two-dimensional lattices. The particles have two attractive patches with equal angular radii of ϕ_0 (we will hereafter refer to this as the patch size), one of which has a central axis that is offset from the central axis of the other patch by an angle β. Without loss of generality, we take the central axis of the patch lying in the southern hemisphere of the particle (the "bottom" patch) to point through the south pole of the particle (and, consequently, through the north pole on the opposite side); the northern ("top") patch is considered the offset patch.

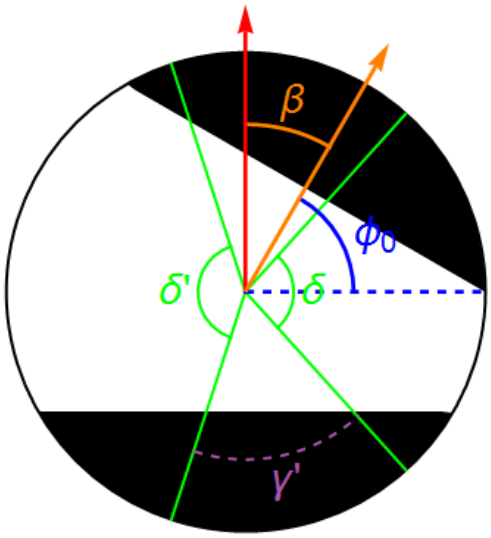

Figure 3.8: A two-dimensional triblock Janus particle with one attractive patch (of angular radius ϕ_0) offset by an angle β. The four green solid lines represent the four attractive bonds of the particle separated by angles $\delta, \delta', \gamma, \gamma'$. The red arrow points to the "north" pole of the particle, defined without loss of generality to be opposite the non-offset bottom patch. The orange arrow bisects the offset patch. The black portions represent the attractive patches.

The triblock Janus particle supports four attractive bonds in two dimensions, two in each patch. These bonds define four angles (see Fig. 3.8), two between attractive bonds in the same patch, γ and γ' and two between attractive bonds in different patches, α and α' such that

$$\delta + \delta' + \gamma + \gamma' = 2\pi. \tag{3.5.14}$$

In the equilibrium state at zero temperature, the values of these angles are fixed at

$$\delta = \delta' = \frac{2\pi}{3}, \quad \gamma = \gamma' = \frac{\pi}{3}; \tag{3.5.15}$$

at finite temperature, fluctuations cause deviations from these values. It is important to note that the pairs of bonds separated by angles γ and γ' connect to triblock Janus particles that are themselves nearest-neighbor pairs; therefore, fluctuations in γ and γ' correspond to fluctuations in the bond length between nearest neighbors. It has been determined in

experimentally-produced lattices of triblock Janus particles that the stiffness against fluctuations in NN bond length is much stronger than the stiffness against fluctuations in angles between bonds that does not change any NN bond lengths [46]. Thus, the fluctuations in γ and γ' are much smaller than those in δ and δ', and we can reasonably ignore fluctuations in the former. Therefore,

$$\delta + \delta' = \frac{4\pi}{3}, \tag{3.5.16}$$

so there is only one independent variable remaining, which we select to be δ.

For given values of δ and β, we need to determine the allowed orientations – ranges of θ – in order to obtain the orientational entropy, as discussed previously. To this end, we orient the particle such that the central axis through the north pole (and hence, where polar angle $\theta = 0$) is perpendicular to the axis across which the bonds separated by δ and δ' have reflection symmetry. Then four conditions – one for each attractive bond – can be derived by comparing the angular position of each bond to that of its closest patch boundary to ensure that, for a given orientation θ of the particle, each bond remains in its corresponding attractive patch:

$$\begin{aligned}
\frac{\pi - \delta}{2} &\leq \theta + \beta + \phi_0 && \text{(top right)} \\
\frac{\pi + \delta}{2} &\geq \theta + \pi - \phi_0 && \text{(bottom right)} \\
\frac{5\pi}{6} + \frac{\delta}{2} &\leq \theta + \pi + \phi_0 && \text{(bottom left)} \\
\frac{13\pi}{6} - \frac{\delta}{2} &\geq \theta + \beta + 2\pi - \phi_0 && \text{(top left)}
\end{aligned} \tag{3.5.17}$$

Before proceeding, it is useful to introduce the quantity

$$\alpha \equiv \delta - \frac{2\pi}{3}, \tag{3.5.18}$$

which measures the fluctuation of δ from its zero-temperature equilibrium value. Since $\delta + \delta' = 4\pi/3$, $\alpha > 0$ means that the two bonds separated by angle δ are further apart than

the two bonds separated by angle δ', and vice versa for $\alpha < 0$. Note that this definition of α is the same as in the lattice theory when $\alpha_0 = 0$ (i.e., when the reference state is the untwisted kagome lattice) – when $\alpha = 0$, $\delta = 2\pi/3$, which corresponds to the untwisted kagome lattice. Depending on whether the rotation is clockwise or counterclockwise, two out of the four bonds will be the constraining bonds in the sense that they will be the first bonds to leave an attractive patch, resulting in a broken attractive bond, during a rotation. For a clockwise rotation (which corresponds to $\theta > 0$), the upper left and lower right bonds are the constraining bonds. For a counterclockwise rotation (which corresponds to $\theta < 0$, the upper right and lower left bonds are the constraining bonds. In each pair, the bond that ends up being the most constraining depends on the sign of the quantity $\alpha + \beta$. Therefore, in order to obtain the orientational weight, we can pair the conditions in (3.5.17) together in integrals over all possible orientations – values of θ – as Heaviside step functions to ensure that only the configurations that keep all bonds within the bounds of the attractive patches are counted. For $\alpha + \beta < 0$,

$$\Omega_j = \int_{-\pi}^{\pi} \mathrm{d}\theta\, \Theta\left(\theta + \frac{\delta - \pi}{2} + \phi_0 + \beta\right) \Theta\left(\frac{\delta - \pi}{2} + \phi_0 - \theta\right) = 2\left(\phi_0 - \frac{\pi}{6}\right) + \alpha + \beta \quad (3.5.19)$$

while for $\alpha + \beta > 0$,

$$\Omega_j = \int_{-\pi}^{\pi} \mathrm{d}\theta\, \Theta\left(\theta + \frac{\pi}{6} - \frac{\delta}{2} + \phi_0\right) \Theta\left(\frac{\pi}{6} - \frac{\delta}{2} + \phi_0 - \beta - \theta\right) = 2\left(\phi_0 - \frac{\pi}{6}\right) - \alpha - \beta. \quad (3.5.20)$$

Both of these expressions can be combined into a single result,

$$\Omega_j = 2\left(\phi_0 - \frac{\pi}{6}\right) - |\alpha + \beta|\,, \quad (3.5.21)$$

so that the orientational entropy for a single particle is

$$s_j = k_B \ln\left[2\left(\phi_0 - \frac{\pi}{6}\right) - |\alpha + \beta|\right] \quad (3.5.22)$$

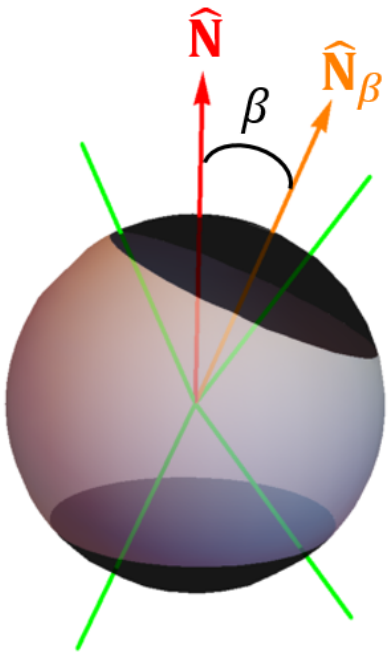

Figure 3.9: A three-dimensional triblock Janus particle with one attractive patch (of angular radius ϕ_0) offset by an angle β. The four green solid lines represent the four attractive bonds of the particle. The red arrow points to the "north" pole of the particle, defined without loss of generality to be opposite the non-offset bottom patch. The orange arrow, which points to the center of the offset patch, provides the third angle needed to fully specify the orientation of the particle. The black circular portions represent the attractive patches.

The orientational entropy is maximized when $\alpha = -\beta$.

3.5.3 Three-dimensional triblock Janus particles

Next, we consider the case of three-dimensional spherical particles confined to a plane (which we take to be the $y = 0$ plane in the following analysis) so that they form two-dimensional lattices. The particles have two circular attractive patches with equal angular radii (patch size) of ϕ_0, one of which has a central axis that is offset from the central axis of the other patch by an angle β (Fig. 3.9). Just as in the case of two-dimensional particles, we take the central axis of the patch lying in the southern hemisphere of the particle (the "bottom" patch) to point through the south pole (and, consequently, through the north pole on the opposite side); the northern ("top") patch is considered the offset patch. The

orientation of the particle requires, in general, three angles to be fully specified: polar angle θ and azimuthal angle φ, which specify the direction of the bottom patch (in our convention), and a third angle ψ, which specifies the direction of the offset top patch as an extra azimuthal angle around the central axis through the north pole. Therefore, the direction of the north pole of the particle is given by the unit vector

$$\hat{\mathbf{N}} = \big(\sin\theta\cos\phi, \sin\theta\cos\phi, \cos\theta\big), \tag{3.5.23}$$

while the direction of the top patch and, hence, the complete orientation of the particle, is specified by the unit vector

$$\begin{aligned}\hat{\mathbf{N}}_\beta = \big(&\cos\beta\sin\theta\cos\phi + \sin\beta\left(\cos\theta\cos\phi\cos\psi - \sin\phi\sin\psi\right),\\ &\cos\beta\sin\theta\sin\phi + \sin\beta\left(\cos\theta\sin\phi\cos\psi - \cos\phi\sin\psi\right),\\ &\cos\beta\cos\theta - \sin\beta\sin\theta\cos\psi\big)\end{aligned} \tag{3.5.24}$$

The angle between $\hat{\mathbf{N}}$ and $\hat{\mathbf{N}}_\beta$ is indeed β: $\hat{\mathbf{N}}\cdot\hat{\mathbf{N}}_\beta = \cos\beta$.

Just as in the case of the two-dimensional triblock disk, we can orient the triblock sphere such that the central axis through the north pole is perpendicular to the plane across which the bonds separated by δ and δ' have reflection symmetry. In this case, the unit vectors in the directions of the four attractive bonds are

$$\mathbf{M}_1 = \left(\cos\frac{\delta}{2}, 0, \sin\frac{\delta}{2}\right) \qquad \mathbf{M}_2 = \left(\cos\frac{\delta}{2}, 0, -\sin\frac{\delta}{2}\right) \tag{3.5.25}$$

$$\mathbf{M}_3 = \left(-\cos\frac{\delta'}{2}, 0, \sin\frac{\delta'}{2}\right) \qquad \mathbf{M}_4 = \left(-\cos\frac{\delta'}{2}, 0, -\sin\frac{\delta'}{2}\right) \tag{3.5.26}$$

The top two bonds will remain in the offset top attractive patch provided that

$$\mathbf{N}_\beta\cdot\mathbf{M}_i \geq \cos\phi_0, \quad i\in\{1,3\}, \tag{3.5.27}$$

while the bottom two bonds will remain in the bottom attractive patch if

$$-\mathbf{N}\cdot\mathbf{M}_i \geq \cos\phi_0, \quad i \in \{2,4\}. \tag{3.5.28}$$

Thus, the number of allowed orientations for a single particle is proportional to

$$\Omega_j = \frac{1}{2\pi}\int_0^{\pi} \mathrm{d}\theta\, \sin\theta \int_{-\pi}^{\pi} \mathrm{d}\varphi \int_{-\pi}^{\pi} \mathrm{d}\psi \prod_{i=2,4} \Theta\left(\left|\hat{\mathbf{N}}\cdot\hat{\mathbf{M}}_i\right| - \cos\phi_0\right) \prod_{i=1,3} \Theta\left(\left|\hat{\mathbf{N}}_\beta\cdot\hat{\mathbf{M}}_i\right| - \cos\phi_0\right). \tag{3.5.29}$$

The orientational entropy, as before, is then given by $s_j = k_B \ln\Omega_j$ and is plotted as a function of twisting angle α for various patch sizes ϕ_0 and patch offset angles β in Fig. 3.10. As expected, when there is no offset ($\beta = 0°$), untwisted bonds ($\alpha = 0$) are entropically preferred (note that we are considering only a single particle at this time, not the entire lattice), as discussed in [46, 61]. For intermediate values of β, the untwisted configuration is still entropically preferred, though the entropic "well" becomes increasingly flat. At sufficiently large values of β, however, a non-zero twisting angle ultimately becomes entropically advantageous, which is a new phenomenon not exhibited by triblock Janus particles with no offset patches, for any patch size.

The entropy profile is highly dependent on patch size, as well; for a given value of β, larger patch sizes will allow for greater variation in the twisting angle, so that it is more likely that the untwisted bond configuration will still be favorable, and the crossover to a non-zero twisting angle bond configuration being preferred will occur at a higher threshold value of β. For smaller patch sizes, the twisting angle is constrained to follow the offset patch very closely, so that the value of the twisting angle with maximal orientational entropy α^* is approximately equal to β (Fig. 3.11). In all cases, the value of α^* converges towards β as β increases.

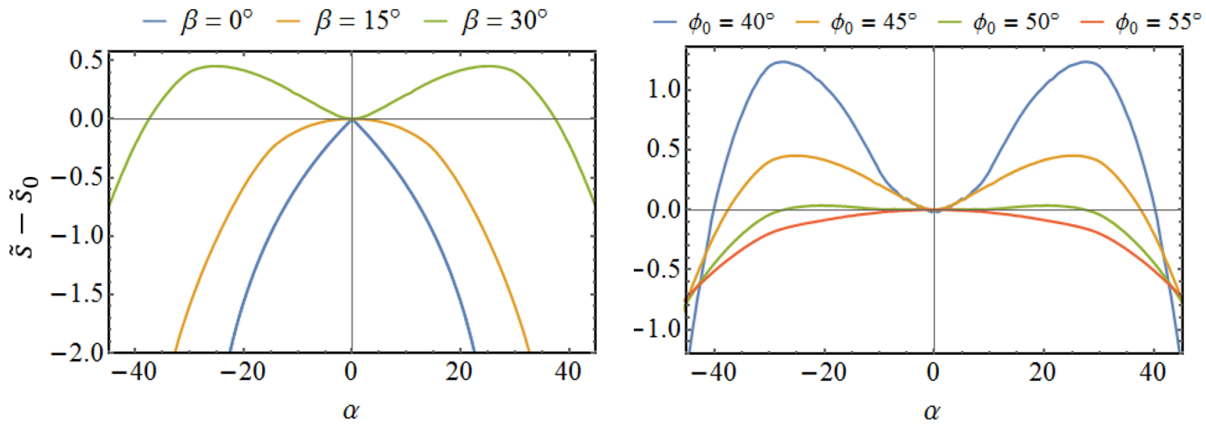

Figure 3.10: The orientational entropy of a three-dimensional triblock Janus particle as a function of twisting angle α for various patch sizes ϕ_0 and patch offset angles β. $\alpha = 0$ corresponds to bonds with nearest neighbors, yielding an untwisted kagome lattice. (Left) Orientation entropy for particles with a patch size of $\phi_0 = 45°$ offset at $\beta = 0°, 15°, 30°$. (Right) Orientational entropy for particles with patch sizes of $\phi_0 = 40°, 45°, 50°, 55°$ at a single offset angle $\beta = 30°$.

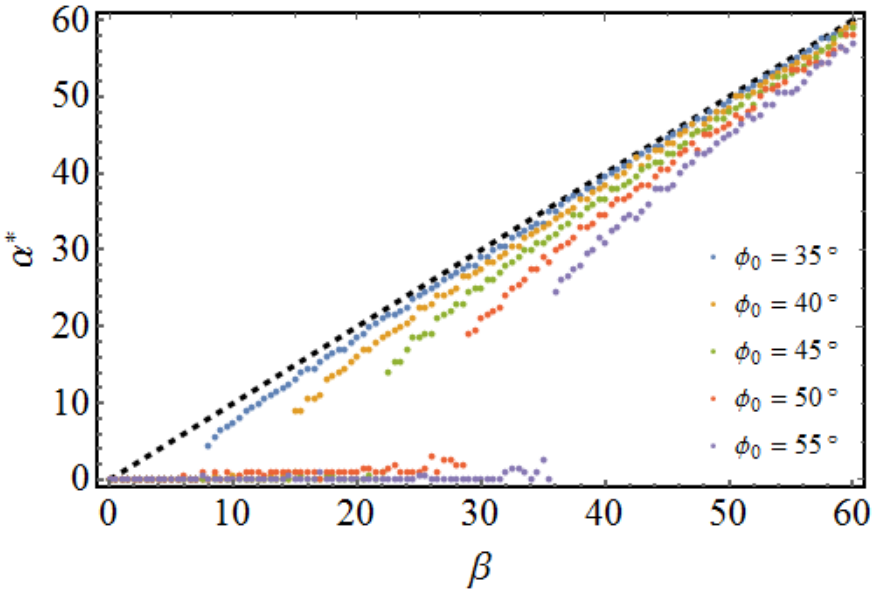

Figure 3.11: Values of α^*, the value of the twisting angle α with maximal entropy, as a function of the offset angle β for five different patch sizes. The black dashed line is $\alpha^* = \beta$; for all patch sizes, the value of α^* converges to this line as β increases; expectedly, the smaller the patch size, the earlier the convergence, as the twisting angle is more constrained for a smaller patch size.

3.5.4 Effective Hamiltonian and the phase diagram

In order to ultimately connect these results for a three-dimensional triblock Janus particle to those obtained in the lattice theory portion of this chapter, we need to construct an expression for the effective Hamiltonian governing the patchy-particle system. The central-force component of the Hamiltonian is obtained by treating the nearest-neighbor attractive bonds (recall that there are no non-attractive bonds for the kagome lattice) as harmonic springs, so that

$$h_{\mathrm{CF}} = \sum_{b \in NN} v_b \left(|\mathbf{R}_b| - |\mathbf{R}_{0b}| \right) = \frac{1}{2} \sum_{b \in NN} \frac{\left(|\mathbf{R}_b| - |\mathbf{R}_{0b}| \right)^2}{|\mathbf{R}_{0b}|^2}, \tag{3.5.30}$$

as in Section 3.4.

The next-nearest-neighbor quartic-order potential is realized as an approximation to the orientational entropy calculated previously. It is important to note that this NNN contribution is not of energetic origin, as it was in the lattice theory, where we explicitly placed anharmonic springs between next-nearest-neighboring sites, but rather is purely entropic in nature – thermal fluctuations have lifted the flatness of the potential well of the attractive patch via another manifestation of the "order-by-disorder" effect. The shape of the orientation entropy, in particular for intermediate values of offset angle β, is seemingly well-approximated by a quartic-order function. In order to fit such a function and obtain two elastic coefficients, τ_{eff} and λ_{eff}, we need two quantities: the second-order and fourth-order moments of α,

$$m_2(\beta) \equiv \langle \alpha^2 \rangle = \frac{\int \mathrm{d}\alpha \, \alpha^2 \Omega(\beta, \alpha)}{\int \mathrm{d}\alpha \, \Omega(\beta, \alpha)} \tag{3.5.31}$$

$$m_4(\beta) \equiv \langle \alpha^4 \rangle = \frac{\int \mathrm{d}\alpha \, \alpha^4 \Omega(\beta, \alpha)}{\int \mathrm{d}\alpha \, \Omega(\beta, \alpha)}. \tag{3.5.32}$$

We can then generate a quartic-order fit for the entropy

$$\tilde{s} \simeq -\frac{b_2}{2}\alpha^2 - \frac{b_4}{4!}\alpha^4 \tag{3.5.33}$$

by requiring that the quartic approximation have the same second and fourth moments.[1] Note that the dependence on offset angle and patch size are carried in the coefficients b_2 and b_4. Then the effective Hamiltonian, which is the sum of the central-force component and the orientational-entropy component, is

$$h_{\text{eff}} = \frac{1}{2}\sum_{b\in NN}\frac{\left(|\mathbf{R}_b| - |\mathbf{R}_{0b}|\right)^2}{|\mathbf{R}_{0b}|^2} + \frac{b_2\widetilde{T}}{2}\sum_i \alpha_i^2 + \frac{b_4\widetilde{T}}{4!}\sum_i \alpha_i^4. \tag{3.5.34}$$

In order to determine the relationship between b_2, b_4 and τ, λ, we will need to compare this effective Hamiltonian with that in Eq. (3.3.17). Before that ultimate step, however, we should recall that we are considering the uniform twisting mechanism; therefore, $\alpha_i = \alpha\,\forall i$. Additionally, in comparing Hamiltonians, we need not concern ourselves with fluctuations and, hence, just as in the zero-temperature lattice theory, the nearest-neighbor summation in our effective Hamiltonian vanishes. We can finally compare the two Hamiltonians, and by equating the coefficients of α^2 and α^4, we obtain expressions for the effective elastic constants,

$$\tau_{\text{eff}} = \frac{b_2\widetilde{T}}{6} \tag{3.5.35}$$

$$\lambda_{\text{eff}} = \frac{b_4\widetilde{T}}{6} - 5\tau_{\text{eff}} = \frac{\widetilde{T}}{6}\left(b_4 - 5b_2\right). \tag{3.5.36}$$

Now that we have obtained the effective elastic constants, we can proceed to determine the phase boundary. Before doing so, let us consider a few regimes that require no further

[1] Alternatively, the entropy can be fit to a quartic approximation using a least squares algorithm. It turns out that the resulting approximation coefficients are rather similar to those obtained using the moment-constraint method employed in the main text over the ranges of β that are important to the discussion of the phase transition for various patch sizes ϕ_0.

analysis. From our lattice theory considerations, we know that $\tau_{\text{eff}} < 0$ is a necessary condition for the twisted-untwisted phase transition. Thus, for values of $\tau_{\text{eff}} > 0$, we know that the Janus particles will form an untwisted kagome lattice, regardless of temperature. Similarly, for a given patch size, there is a threshold offset angle β_0, above which the orientational weight (degeneracy factor) of the untwisted bond configuration, $\Omega_0 \equiv \Omega(\alpha = 0)$, vanishes. In this case, it is clear that the untwisted kagome lattice cannot form, as the necessary bond configuration would result in the energetically-costly breaking of attractive bonds. Thus, in this region, the Janus particles necessarily form a twisted kagome lattice. Finally, there is a region between these two, in which $\tau < 0$, but $\Omega_0 > 0$, where the temperature-dependent phase transition will occur. This requires the subsequent further analysis. A plot of these regions in the $\beta - \phi_0$-plane is given in Fig. 3.12.

Finally, now that we have our effective constants, the results from the lattice theory calculations can be applied. If we assume the same conditions, $\tau_{\text{eff}} \ll 1 \ll \lambda_{\text{eff}}$, we can directly use the equation for the phase boundary, Eq. 3.4.47.[2] Substituting in for τ_{eff} and λ_{eff} and solving for $\widetilde{T}_c$, we obtain a critical phase boundary in terms of b_2 and b_4 (which, again, contain the dependence on β and ϕ_0),

$$\widetilde{T}_c = \frac{c^2 \left|b_2\right|^3}{6\left(b_4 - 5b_2\right)^2}, \tag{3.5.37}$$

where $c = 1.1544$, the coefficient of the phase boundary in the lattice calculation. The resulting phase diagram is presented in Fig. 3.13 for five patch sizes. For all patch sizes, there is a minimum offset angle beyond which the Janus particles should spontaneously form a twisted kagome lattice. Naturally, the phase boundary shifts to larger values of β for larger patch sizes, as it requires a larger offset angle to create an entropic disadvantage for the untwisted bond configuration, $\alpha = 0$. Furthermore, for a range of offset angles for

[2]One point of caution here is that this may not be satisfied for Janus particles with large patch sizes and/or large offset angles, since that allows for large twisting angles. One aspect of our lattice theory was that the twisting angle should remain small. Nonetheless, this provides for an initial formulation of the phase diagram and can subsequently be studied further.

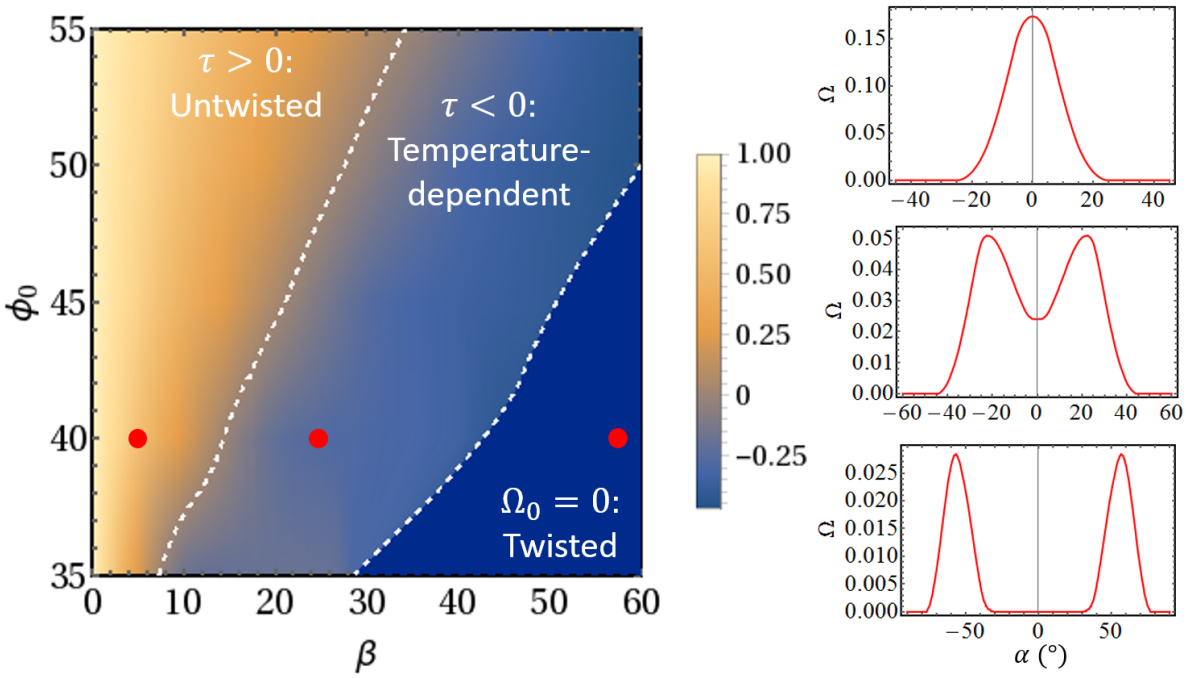

Figure 3.12: A plot of $\tau/(\tau_0\widetilde{T})$ as a function of offset angle β and patch size ϕ_0, where $\tau_0 = \tau(\beta = 0)$ for a given patch size. The left white dashed curve is $\tau = 0$, while the right dashed curve marks where the weight for untwisted bonds $\Omega_0 = \Omega(\alpha = 0)$ first vanishes (for increasing β). The leftmost region, where $\tau > 0$, will necessarily yield an untwisted kagome lattice, whereas the rightmost region, where $\Omega_0 = 0$, yields a twisted kagome lattice. The middle region is where the temperature-dependent phase transition occurs. The three red dots correspond to the plots of the orientational weights (degeneracy factors) on the right for a patch size of $\phi_0 = 40°$. The values of β were chosen to illustrate the profile of the weight function in each of the three regions discussed above.

each patch size, the transition between the untwisted kagome lattice and the twisted kagome lattice can be traversed simply by manipulating the temperature of the colloidal solution. It will quite interesting to see the manifestation of such a transition in a lab setting.

3.6 Discussion

In this chapter, we have studied the structural phase transition between the kagome lattice and the twisted kagome lattice and have found that the structural transition, which is continuous at $T = 0$, becomes first order at finite temperature due to the renormalization of the twisting modulus of the untwisted kagome lattice from the near-divergent contribution

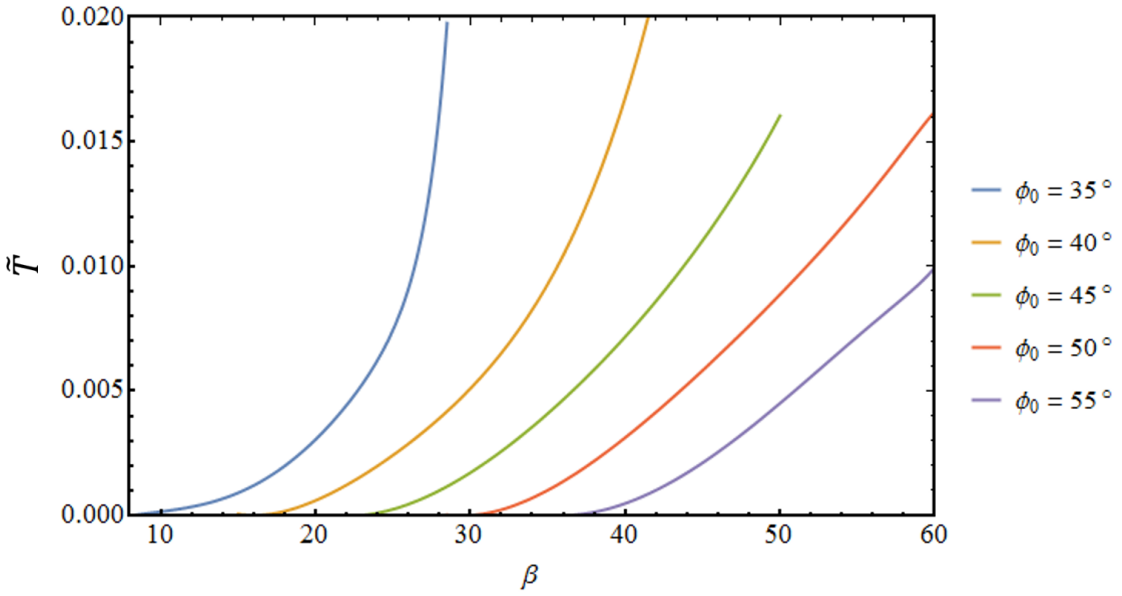

Figure 3.13: The Janus particle phase diagram as a function of offset angle β and temperature $\widetilde{T}$ for five different patch sizes. To the left of, and above, each corresponding phase boundary is the untwisted kagome phase, while to the right of, and below, is the twisted kagome phase.

of near-floppy modes to the free energy. The transition also occurs at critical values of $\tau_c < 0$, meaning that there is a region in the phase diagram where the kagome lattice is stabilized by these entropic contributions. To ensure that this does not simply remain an intellectual pursuit, we then explored the experimental system of triblock Janus particles, in which the effects of entropic stabilization can be observed in the formation of self-assembled open structures such as the kagome lattice. We showed that the same entropic effect that leads to directional bonding favoring the kagome lattice over a close-packed structure can result in directional bonding favoring the twisted kagome lattice over even the kagome lattice, for Janus particles fabricated with a sufficiently-offset attractive patch. It will be interesting to see if this can lead to the experimental realization of a stable twisted kagome lattice and, furthermore, if a structural transition between a kagome structure and a twisted kagome structure can indeed be induced by control of the ambient temperature.

CHAPTER IV

Self-assembly of thin triangular prisms via capillary interactions

4.1 Introduction

In this chapter, we investigate the possibility of using a hexapolar-like capillary interaction generated between pairs of thin, triangular microprisms to self-assemble rigid, space-spanning open networks at low particle concentrations. Thin prisms – quasi-two-dimensional shapes with finite, but small, thicknesses – can generate capillary interactions at fluid-fluid interfaces if sufficient interface deformation is induced at the prism sides. The symmetry of thin, triangular prisms indicates that the interaction will be similar to that of capillary hexapoles when these prisms are not too close. This interaction may lead to binding of the triangles at their vertices and yield ordered open structures such as the kagome and the twisted kagome lattices, which consist of a recurring motif of two tip-sharing inverted triangles. Based on the angle between these two triangles, an entire family of lattice sharing the kagome connection topology can be generated, as shown in Fig. 4.1. Open structures such as the kagome lattice family have intriguing properties including negative Poisson's ratio, negative thermal expansion, and, as discussed at the beginning of Chapter III, interesting topological properties. However, open structures also have inherent instability, which make

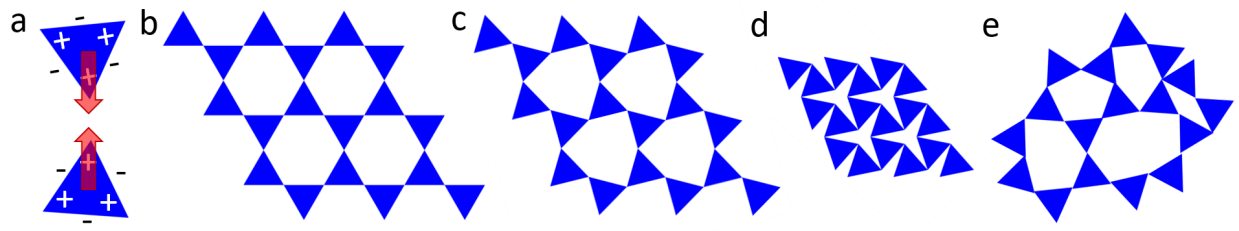

Figure 4.1: Hexapole-like capillary interaction between triangles may lead to the self-assembly of kagome lattices. (a) Hexapole-like interactions between two bowed triangles (positive at tips and negative at edges) cause tip-to-tip binding. (b) The kagome lattice where edges of triangles form straight lines. (c,d) two twisted kagome lattices with different twisting angle. These different versions of the kagome lattice are related by a soft deformation which only changes the angle between the triangles, which leads to a negative Poisson's ratio. (e) Depending on the strength of the hexapole-like interaction, disordered assemblies of triangles may also occur.

it difficult to synthesize such structures and to keep them stable against deformations that will lead to collapse. Therefore, to improve the prospects of assembling such complex open structures – either ordered or disordered – the long-range and potentially highly-directional capillary pair-binding behavior of thin homogenous microprisms at interfaces should be investigated. Better understanding of the resultant transient and steady-state binding can identify conditions for which ordered and/or disordered open structures might occur; both possibilities can yield interesting mechanical properties [90, 91].

In this work, we observe capillary-driven binding of thin, triangular prisms, with edge lengths of $\sim$120 μm and thicknesses between 2.5 and 20 μm, at an air-water interface. The particles are produced by polymeric photolithography and are found to undergo an unexpected bowing deformation during synthesis. The observed anisotropic, directional interactions are due to the resultant generation of a capillary hexapole, which arises due to the triangular shape and the bowing-induced curvature of the three-phase contact line (air, water, and particle). Different types of binding events occur between the tips and the sides of the interacting prisms, with the specific type of binding predictable from the up/down polarity of particle attachment to the interface. From the particle shape and the radius of

curvature of the bowing, we can compute the interface geometry and the resulting capillary interaction numerically. We find that the capillary interaction is similar to the ideal hexapolar interaction in the far field, but that it deviates from the ideal hexapole interaction in the near field due to a focusing of interfacial deformation near the tips of the prisms. This leads to a majority of binding events that proceed through initial binding involving one or two tips (with the exact number dictated by the relative polarity of the prisms). We also simulate trajectories of particle binding events numerically using the numerically-calculated potential, and we obtain good qualitative agreement with the experimental results. These results inform the structural design of complex open networks from simple interfacial building-blocks.

4.2 Theory of capillary interactions

4.2.1 Analytic interface height solutions

The pressure difference across an interface between two stationary, immiscible fluids is given by the Young-Laplace equation,

$$\Delta p = p_1 - p_2 = -\gamma \nabla \cdot \mathbf{n}, \tag{4.2.1}$$

where γ is the surface tension and $\mathbf{n}$ is the unit vector pointing from the lower fluid (2) to the upper fluid (1). Note that $-\nabla \cdot \mathbf{n} = 2H$, where H is the mean curvature of the interface. Suppose that the height of the interface is given by $h(\mathbf{x})$, where the far-field equilibrium height of the interface is $h = 0$ (the interface is flat and, consequently, the pressure difference across the interface is zero). Then, from hydrostatic equilibrium, we know that

$$p_i = p_0 - \rho_i g h, \tag{4.2.2}$$

where p_0 is the far-field equilibrium pressure at $h = 0$ and ρ_i is the density of the ith fluid. Upon substitution, the Young-Laplace equation becomes

$$(\rho_2 - \rho_1)\, gh = -\gamma \nabla \cdot \mathbf{n}. \tag{4.2.3}$$

Now, the unit normal to the surface, $\mathbf{n}$, can be written in terms of gradients of the height field:

$$\mathbf{n} = \frac{\nabla(z-h)}{|\nabla(z-h)|} = \frac{\hat{\mathbf{e}}_\mathbf{z} - \nabla h}{\sqrt{1+|\nabla h|^2}}. \tag{4.2.4}$$

The divergence of the first term vanishes, as it entails the partial derivative with respect to z of a function of only planar variables (e.g., x and y). Thus, the Young-Laplace equation in terms of the height field is

$$\nabla \cdot \frac{\nabla h}{\sqrt{1+|\nabla h|^2}} = \kappa^2 h \tag{4.2.5}$$

where

$$\kappa = \ell_c^{-1} \equiv \sqrt{\frac{(\rho_2 - \rho_1)g}{\gamma}}. \tag{4.2.6}$$

is the inverse capillary length. The capillary length is a characteristic length scale arising from comparing the relative strengths of gravitational acceleration and the surface tension; for length scales much smaller than the capillary length, the effects of gravity can be neglected. The capillary length of an air-water interface is 2.7 mm.

We can simplify the governing equation of the interface height h by making two assumptions that are typically satisfied by micron-sized particles. First, the interface slope is taken to be small: $|\nabla h|^2 \ll 1$. Second, we consider length scales that are much smaller than the capillary length, $a \ll \ell_c$. In this case, the Bond number is vanishingly small, $\mathrm{Bo} = (\kappa a)^2 \ll 1$, and the Young-Laplace equation simplifies to the 2-D Laplace's equation,

$$\nabla^2 h = 0 \tag{4.2.7}$$

Let us consider the case of a solid particle adsorbed to the interface such that the contact

line between the interface and the particle surface is undulating. This can be due to particle shape (anisotropies, corners, and edges) and surface roughness/irregularities. These undulations can be decomposed into a multipole expansion such that this differential equation can be solved analytically, for particles with circular cross-sections, using polar coordinates (r, θ). The solution for the interface height profile is

$$h(r,\theta) = H_0 \ln(\kappa r) + \sum_{m=1}^{\infty} H_m \left(\frac{r_0}{r}\right)^m \cos\left[m(\theta - \theta_{m,0})\right] \tag{4.2.8}$$

where H_m is the amplitude of the mth moment at the surface/circumference of the particle's circular projection, r_0. $m \in \mathbb{Z}^+ \cup \{0\}$ is the multipole moment, and $m = 0, 1, 2, 3$ correspond to the monopole/charge, dipole, quadrupole, and hexapole moments, respectively (Fig. 4.2). If the particle adsorbed to the interface is sufficiently light, the monopole moment vanishes; if the particle is allowed to spontaneously rotate about a horizontal axis, then the dipole moment also vanishes. Therefore, the quadrupole moment ($m = 2$) is typically the leading non-zero term in the multipole expansion.

For two particles with circular cross-sections, it is convenient to use bipolar coordinates (ω, τ) to obtain a solution to (4.2.7). They are defined implicitly via

$$x = \frac{a \sinh \tau}{\cosh \tau - \cos \omega}, \qquad y = \frac{a \sin \omega}{\cosh \tau - \cos \omega} \tag{4.2.9}$$

where $\tau \in \mathbb{R}, \omega \in [0, 2\pi)$ (or, equivalently, $\omega \in [-\pi, \pi)$). Curves of constant ω and τ are circles that intersect at right angles in the xy-plane.

The parameter a can be written entirely in terms of the particle radii R_1, R_2 and their separation distance r as

$$a^2 = \frac{1}{4r^2}\left[r^2 - (R_1 + R_2)^2\right]\left[r^2 - (R_1 - R_2)^2\right]. \tag{4.2.10}$$

Note that, in the bipolar coordinate system, the circular projections of the contact lines on

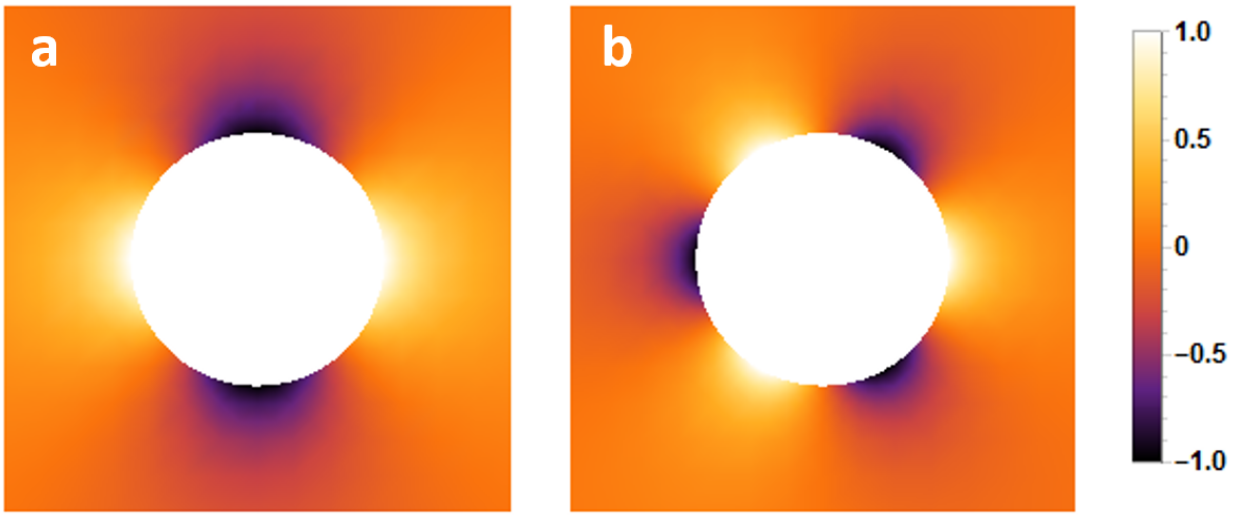

Figure 4.2: Theoretical interface height profiles for particles with circular cross-sections and contact lines undulating according to prescribed multipole moments. (a) A capillary quadrupole ($m = 2$), with four alternating regions of positive and negative interface height (the equilibrium interface height far from any particles is taken to be zero), and (b) A capillary hexapole ($m = 3$) with six alternating regions of positive and negative interface height.

the xy-plane are curves of constant τ, $\tau = -\tau_1$ and $\tau = \tau_2$, where

$$\tau_1 = \cosh^{-1}\left(\frac{r^2 + R_1^2 - R_2^2}{2rR_1}\right) \tag{4.2.11}$$

$$\tau_2 = \cosh^{-1}\left(\frac{r^2 + R_2^2 - R_1^2}{2rR_2}\right). \tag{4.2.12}$$

Rewriting Laplace's equation in terms of bipolar coordinates ultimately yielding a deceptively simple partial differential equation of the form

$$\frac{\partial^2 h}{\partial \omega^2} + \frac{\partial^2 h}{\partial \tau^2} = 0. \tag{4.2.13}$$

The derivation can be found in [92]; the resultant interface solution is

$$\begin{aligned} h(\omega,\tau) = H_1 \sum_{n=1}^{\infty} A(n,m_1,\tau_1)\cos(n\omega - m_1\phi_1)\frac{\sinh[n(\tau_2-\tau)]}{\sinh[n(\tau_1+\tau_2)]} \\ + H_2 \sum_{n=1}^{\infty} A(n,m_2,\tau_2)\cos(n\omega - m_2\phi_2)\frac{\sinh[n(\tau_1+\tau)]}{\sinh[n(\tau_1+\tau_2)]} \end{aligned} \tag{4.2.14}$$

where

$$A(n,m_i,\tau_i) = m_i \sum_{k=0}^{\min(m_i,n)} \frac{(-1)^{m_i-k}(m_i+n-k-1)!}{(m_i-1)!(n-k)!k!}\exp[-(m_i+n-2k)\tau_i]. \tag{4.2.15}$$

4.2.2 Interaction energy between two capillary multipoles

The capillary interaction energy between two particles is a function of their orientations and separation distance. It is given by

$$U_{12} = \gamma(\delta S_{12} - \delta S_1 - \delta S_2), \tag{4.2.16}$$

where δS_{12} is the excess area created at the interface in the full two-particle system, and $\delta S_i\,(i=1,2)$ is the excess area in an isolated one-particle system (i.e., the separation distance $r \to \infty$). The excess area is defined as the difference between the actual surface area Σ^* and the projected surface area Σ (the interface would be planar without the deformation caused by the particle) [93].

In order to calculate the excess surface area, we first consider an infinitesimal element of the actual surface area, $dS^* = dx^*dy^*$, and use a local rotated coordinate system such that the slope is maximum along the y coordinate. Then the slope is zero perpendicular to that direction, at least for an infinitesimal length element, so $dx = dx^*$. For dy^*,

$$dy^* = \sqrt{dy^2+dh^2} \approx dy\sqrt{1+\left(\frac{dh}{dy}\right)^2} = dy\sqrt{1+|\nabla h|^2}, \tag{4.2.17}$$

where we have generalized to a coordinate-independent expression in the last equality, using the fact that $dh/dx = 0$. Using the small-slope approximation, we can expand in $|\nabla h|$, so that

$$dy^* \approx dy \left(1 + \frac{1}{2}|\nabla h|^2\right). \tag{4.2.18}$$

Then

$$\delta(dS) = dS^* - dS = \frac{1}{2}|\nabla h|^2 dx dy, \tag{4.2.19}$$

and so the formula for excess surface area in the small-slope regime becomes

$$\delta S = \frac{1}{2} \iint_{\Sigma} \mathrm{d}S \, |\nabla h|^2. \tag{4.2.20}$$

From these preceding equations, it is apparent that minimization of the capillary interaction potential coincides with the minimization of excess area beyond that created by two isolated particles. This favors the adoption of particle configurations such that the slope of the resultant interface is reduced. For particles with fixed orientations, the interaction between the two will be attractive if moving the particles closer together will reduce the overall slope of the interface (and, thus, decrease the amount of excess interfacial area) and repulsive if moving the particles further apart will reduce the overall slope.

For a single particle with a circular cross-section, the formula for excess area can be written in polar coordinates as

$$\delta S = \frac{1}{2} \int_{R}^{\infty} \int_{0}^{2\pi} r \mathrm{d}r \mathrm{d}\theta \, |\nabla h|^2, \tag{4.2.21}$$

where R is the cross-sectional radius of the particle. The height of the interface around such a particle with a contact line that is undulating with multipole moment m is given by

$$h(r, \theta) = H \left(\frac{R}{r}\right)^m \cos\left[m\left(\theta - \theta_0\right)\right]. \tag{4.2.22}$$

so that

$$|\nabla h|^2 = m^2 H^2 \frac{R^{2m}}{r^{2m+2}} \tag{4.2.23}$$

Thus, we find that the excess surface area is

$$\delta S_i = \frac{\pi}{2} m H_i^2. \tag{4.2.24}$$

For two capillary multipoles, the excess surface area is [92]

$$\delta S_{12} = \pi \left[H_1^2 S_1 + H_1^2 S_2 - H_1 H_2 G \cos(m_2 \theta_2 - m_1 \theta_1) \right] \tag{4.2.25}$$

where

$$S_i = \sum_{n=1}^{\infty} \frac{n}{2} \coth\left[n(\tau_1 + \tau_2)\right] A^2(n, m_i, \tau_i) \tag{4.2.26}$$

$$G = \sum_{n=1}^{\infty} \frac{n A(n, m_1, \tau_1) A(n, m_2, \tau_2)}{\sinh\left[n(\tau_1 + \tau_2)\right]} \tag{4.2.27}$$

and

$$A(n, m_i, \tau_i) = m_i \sum_{k=0}^{\min(m_i, n)} \frac{(-1)^{m_i - k}(m_i + n - k - 1)!}{(m_i - 1)!(n-k)!k!} \exp[-(m_i + n - 2k)\tau_i]. \tag{4.2.28}$$

Here, it is important to realize that, for two capillary multipoles of the same order, such that $m_1 = m_2$, the interaction energy reduces to a two-dimensional function of their separation distance, r, and their relative orientation, $|\theta_1 - \theta_2|$. The capillary interaction potential between two capillary hexapoles is shown in Fig. 4.3.

4.2.3 Contact-line boundary conditions

The solution to the Young-Laplace equation is subject to two boundary conditions: one at the three-phase (solid, liquid, and fluid, with the latter oftentimes a gas) contact line and

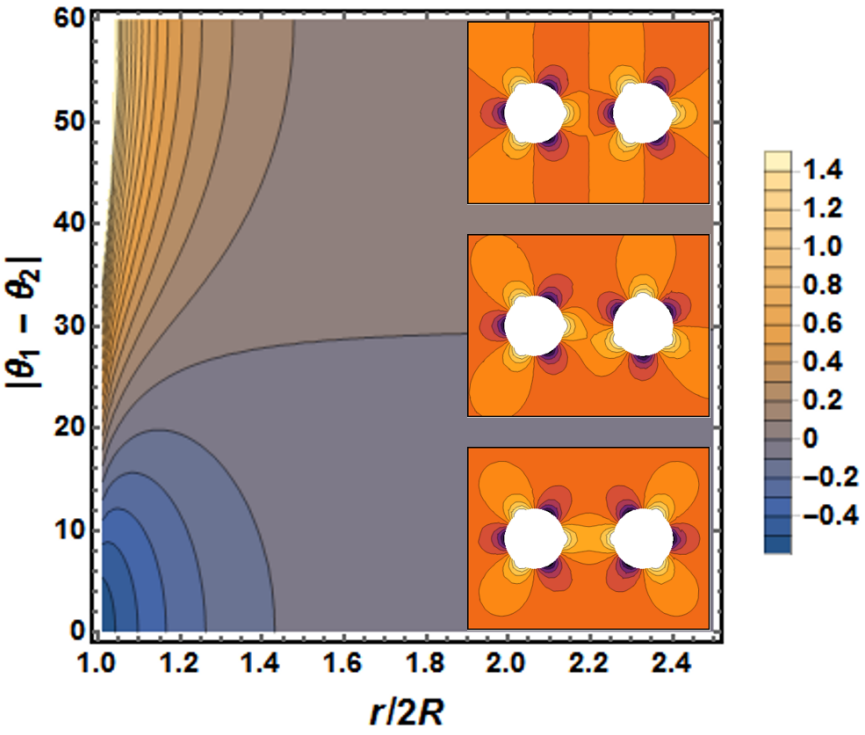

Figure 4.3: Theoretical capillary interaction potential between two capillary hexapoles as a function of separation distance, r, scaled by the diameter of the particles' circular projection, $2R$, and the particles' relative orientation, $|\theta_1 - \theta_2|$. The three insets show the interface height profile of three configurations corresponding to relative orientations of 0°, 30°, and 60° at a distance of $r/2R = 1.8$.

one at the far boundary of the interface, infinitely far away. The latter is typically taken to be the condition of a flat interface. The boundary condition at the contact line, however, can be more complicated. In the simplest case, in which the surface of the solid phase (e.g., a wall or a particle) is energetically homogeneous, the contact line is determined such that the *equilibrium* contact angle, θ_c, between the solid surface and the surface of the interface is constant and satisfies the Young equation [94, 95],

$$\gamma \cos\theta_c = \gamma_{\mathrm{SG}} - \gamma_{\mathrm{SL}}, \tag{4.2.29}$$

where $\gamma, \gamma_{\mathrm{SG}}, \gamma_{\mathrm{SL}}$ are the liquid-gas, solid-gas, and solid-liquid surface tensions, respectively. Eq. (4.2.29) can be simply derived by considering the change in free energy per unit breadth, df, that results from moving the contact line by a distance dx, as shown in Fig. 4.4; at

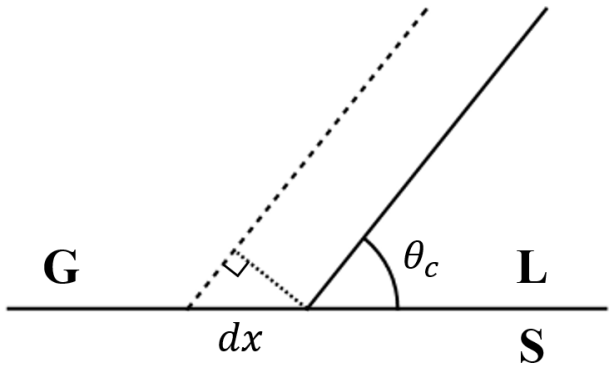

Figure 4.4: Cross-section showing the movement of a three-phase contact line between solid (S), liquid (L), and gas (G) phases with contact angle θ_c by an amount dx. The solid (dotted) line represents the initial (resultant) interface. Used in the derivation of the Young equation.

equilibrium, the change in free energy should be equal to zero:

$$0 = df = (\gamma_{\mathrm{SG}} - \gamma_{\mathrm{SL}})\, dx - \gamma \cos\theta_c\, dx. \tag{4.2.30}$$

For a single, isolated solid particle at a liquid-fluid interface with a energetically-homogeneous surface and an axisymmetric body with a vertical symmetry axis, such as a sphere or vertical cylinder, the contact line should therefore be flat by symmetry [96]. Moreover, for a small spherical particle of radius R and negligible weight (the particle Bond number is vanishingly small), the interface should also be entirely planar; the depth of the particle immersed in the liquid is $d = R(1 + \cos\theta_c)$, with θ_c adhering to the equilibrium value specified by the Young equation [97]. Contrastingly, a small cylindrical particle with negligible Bond number oriented vertically necessarily results in a non-equilibrium contact angle, as will be discussed below.

For a solid particle with a convoluted shape and, thus, contact line, it is not immediately obvious how to specify the contact angle. To facilitate such a determination, we define $\hat{\mathbf{t}}$ as the unit tangent vector to the contact line, $\hat{\mathbf{n}}$ as the unit normal vector to the surface of the particle, and $\hat{\mathbf{b}} \equiv \hat{\mathbf{t}} \times \hat{\mathbf{n}}$ as the unit binormal vector (Fig. 4.5). Then the liquid-gas surface tension unit vector $\hat{\boldsymbol{\gamma}}$ lies in the plane spanned by the vectors $\hat{\mathbf{n}}$ and $\hat{\mathbf{b}}$, and the contact angle is

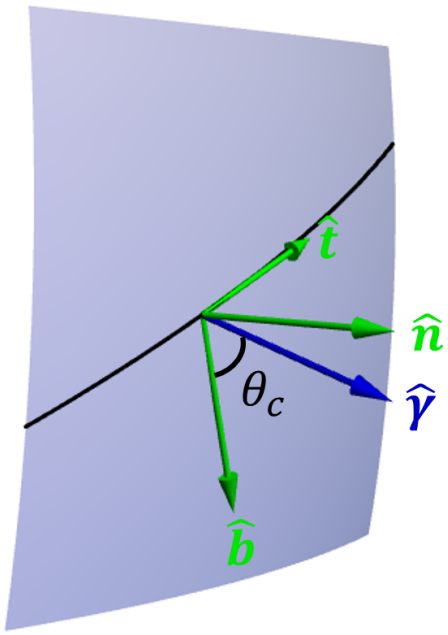

Figure 4.5: Close-up schematic of the surface of an arbitrary particle at an interface. $\hat{\mathbf{t}}$ is the unit tangent vector to the contact line, $\hat{\mathbf{n}}$ is the unit normal vector to the surface of the particle, and $\hat{\mathbf{b}}$ is the unit binormal vector. $\hat{\boldsymbol{\gamma}}$ is tangent to the interface and lies in the plane spanned by the vectors $\hat{\mathbf{n}}$ and $\hat{\mathbf{b}}$. The angle between $\hat{\boldsymbol{\gamma}}$ and $\hat{\mathbf{b}}$ is the contact angle, θ_c.

given by $\hat{\mathbf{b}} \cdot \hat{\boldsymbol{\gamma}} = \cos\theta_c$ [98]. Nonspherical particles, such has ellipsoids [99, 100] and cylinders [101] with respective symmetry axes oriented horizontally, have been shown experimentally and numerically to generate nonplanar contact lines with constant equilibrium contact angles due to the varying curvatures of the particles. Additionally, distortions and undulations in contact lines can occur in particles of any shape due to surface roughness or chemical heterogeneities, which lead to an energetically-inhomogeneous surface [93].

In this chapter, due to the specific shape of the particles used in the experiment – triangular prisms – we will focus on a final form of boundary condition in which the contact line is kinetically trapped, or pinned, at sharp corners and edges of a particle. This pinning results in a non-equilibrium contact angle that can deviate significantly from the equilibrium contact angle discussed above and can also vary along the contact line. As shown by Gibbs in an extension to the Young equation [102, 103], the non-equilibrium contact angle, θ_g, at

a pinned edge can be any value in the range

$$\theta_c \leq \theta_g \leq \pi - \delta + \theta_c, \tag{4.2.31}$$

where δ is the wedge angle of the particle. For example, the wedge angle of the top or bottom edges of a cube is $\pi/2$. Note that the limiting angles of the Gibbs' inequality or criterion are simply the equilibrium contact angles for each of the two surfaces that join together to form the edge with a wedge angle of δ; when θ_g extends beyond the bounds of the inequality, the contact line becomes unpinned and begins to slide along one of the two surfaces, as dictated by which bound was violated [104]. This phenomenon of contact-line pinning has been observed in various experimental systems consisting of solid particles or substrates containing sharp edges [105–107]. For example, returning to the case of a small cylindrical particle with negligible Bond number oriented vertically, a preferred equilibrium contact angle of $\theta_c \neq \pi/2$ cannot be achieved anywhere along the side of the cylinder; therefore, the contact line will either move up (if the preferred contact angle $\theta_c > \pi/2$) or down (if $\theta_c < \pi/2$) until either the top or bottom face, respectively, of the cylinder coincides with the interface [108]. In this case, the contact line is pinned to the edge of the cylinder with non-equilibrium contact angle $\theta_g = \pi/2$, and the surrounding interface is completely planar.

4.3 Experimental system

In this section, we summarize the work and findings (except for dilute binding events, which can be found in Section 4.6) of our experimental collaborators, Joseph Ferrar and Michael Solomon (see [109] for additional details). Four types of triangular prisms are fabricated via SU-8 photolithography. All prisms have an edge length of 120 μm, and thickness of: (a) 2.5 μm, (b) 5 μm, (c) 12 μm, and (d) 20 μm. The ratio of the thickness (T) to length (L) of the prisms is a characteristic parameter; we hereafter refer to each type of prism, as needed,

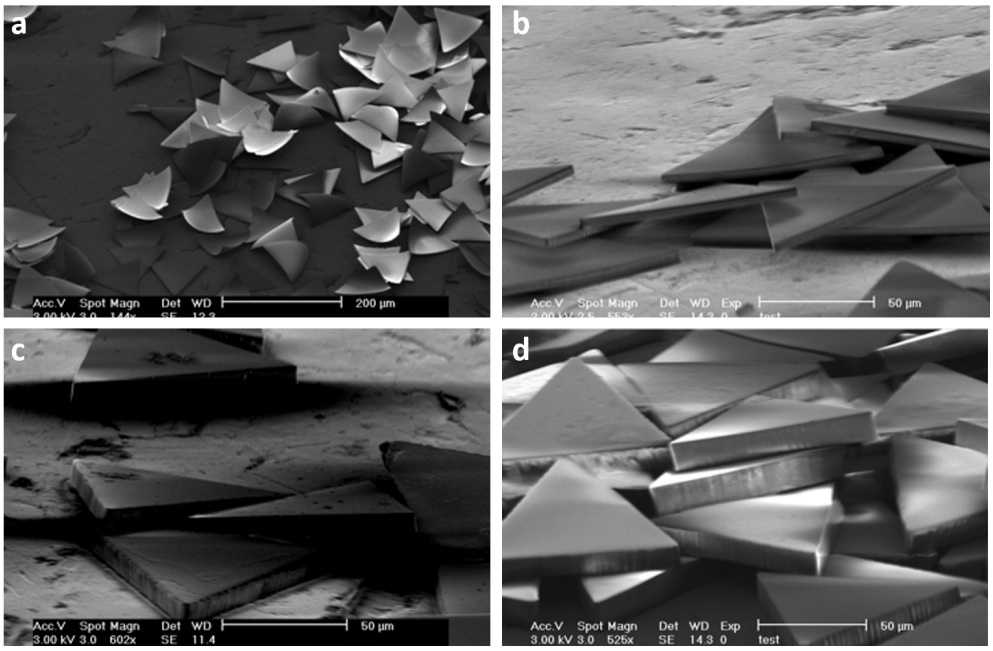

Figure 4.6: SEM images of thin, equilateral triangular microprisms from SU-8 epoxy resin. Equilateral triangle (edge length, $L = 120\,\mu$m) prisms of varying thickness (T) a) $T \sim 2.5\,\mu$m, $T/L = 1/50$, b) $T \sim 5\,\mu$m, $T/L = 1/25$, c) $T \sim 12\,\mu$m, $T/L = 1/10$, d) $T \sim 20\,\mu$m, $T/L = 1/5$. Reprinted from [109] with permission.

as: (a) $T/L = 1/50$, (b) $T/L = 1/25$, (c) $T/L = 1/10$, and (d) $T/L = 1/5$. SEM images of the synthesized particles (Fig. 4.6) show that the thinnest particles, $T/L = 1/50$, $1/25$ have observable bowing prior to deposition on the interface.

The particles are placed on a flat air-water interface, whereupon prisms of all T/L ratios undergo lateral capillary-driven particle-particle binding at the interface. Over a period of about one hour, the prisms self-assemble into open structures of progressively increasing size. The networks span several millimeters in space and are visible to the eye and contain a mix of dense, close-packed regions (with numerous prisms bound edge-to-edge), long strands, and large voids (Fig. 4.7).

Interestingly, the $T/L = 1/50$, $1/25$ and $1/10$ prisms are adsorbed to the interface in such a way that their centers-of-mass either sit slightly above or below the interface. This "positional" polarity (center-of-mass above or below the interface) is perfectly correlated with the "bowing" polarity (bowed upwards or bowed downwards), in that out of all prisms whose

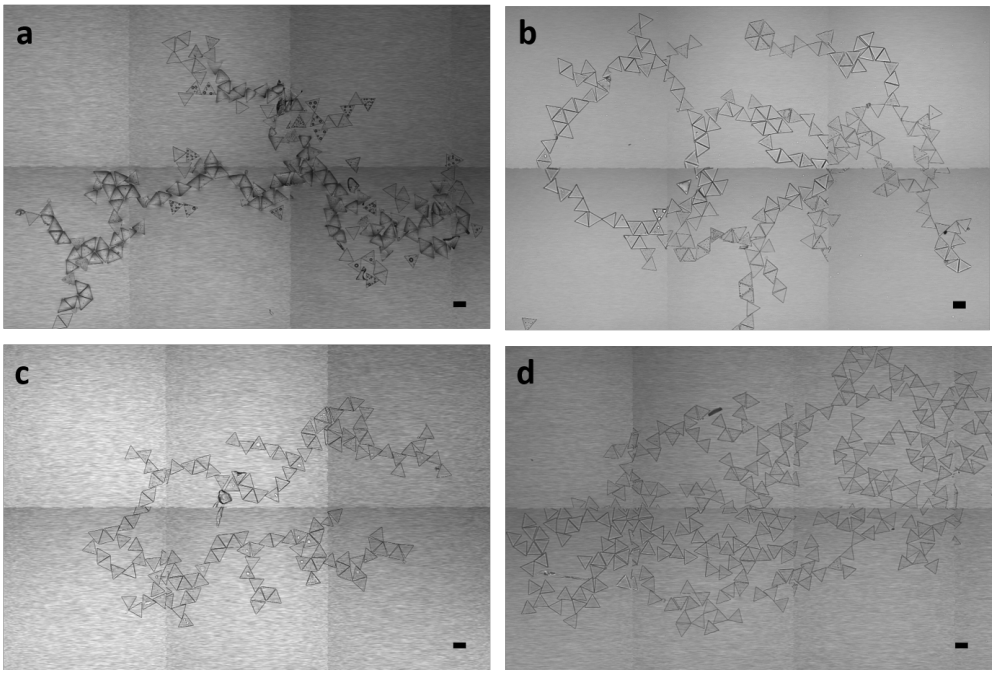

Figure 4.7: Self-assembled open networks from capillary-driven binding of thin triangular microprisms. (a) $T/L = 1/50$, (b) $T/L = 1/25$, (c) $T/L = 1/10$, and (d) $T/L = 1/5$ equilateral triangular microprisms. Scale-bars are $100\,\mu$m. Reprinted from [109] with permission.

positional polarity can be determined via optical microscopy (see Fig. 4.9), all occurrences of bonding between prisms with the same positional polarity are tip-to-tip or edge-to-edge, and all occurrences of bonding between prisms with opposite positional polarities are tip-to-edge or offset edge-to-edge.

Recall that interface contact lines can become kinetically-trapped, or "pinned" at sharp corners and edges of particles. For bowed prisms, a pinned contact line that follows the edges consequently specifies a curved boundary condition for the interface at the prism surface, which is experimentally observed (Fig. 4.8). The resultant deformation of the interface adhering to such a boundary condition in turn determines the capillary-driven attraction between the prisms – the interface curvature at the tips and edges of the triangular prism is opposite for bowed-up and bowed-down prisms, so that like geometrical features will attract for the same bowing polarity and will repel for opposite bowing polarities. Thus, there is a direct correspondence between relative bowing polarity and binding location and, hence, positional polarity.

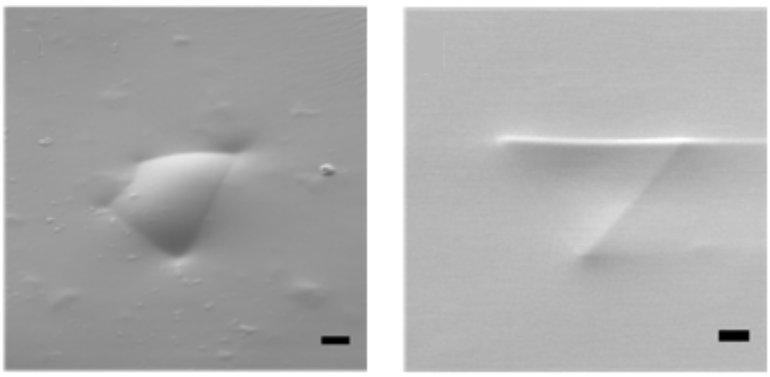

Figure 4.8: Environmental SEM images of $T/L = 1/50$ triangular prisms, fixed at an air-gellan/water, illustrating interfacial deformation that follows the bowing of the prism due to contact-line pinning. (a) Positive "positional" polarity, corresponding to downward bowing. (b) Negative "positional" polarity, corresponding to upward bowing. Scale bars are 20 μm. Adapted from [109] with permission.

Therefore, when we subsequently refer to particles as having the same polarity, we mean that their centers-of-mass are either both above the far-field, equilibrium height of the interface (in which case the particles are both bowed down) or both below the equilibrium height of the interface (in which case the particles are both bowed up); particles with the opposite polarity have centers-of-masses that are on either side, vertically, of the equilibrium interface height (and, thus, the particles are bowed in opposite directions).

4.4 Methods for numerical analysis

4.4.1 Pairwise modeling of the interaction potential using Surface Evolver

In this work, we consider the capillary interaction potential between triangular prisms, for which an analytic solution to Laplace's equation – especially close to the prisms, where simplifying assumptions cannot be made – is not obtainable. Therefore, we use Surface Evolver [110], a program widely utilized to model the shape of liquid surfaces and interfaces, to numerically calculate the shape of the interface. The final solution is achieved by an algorithmic succession of steps involving gradient and conjugate gradient descent iterations

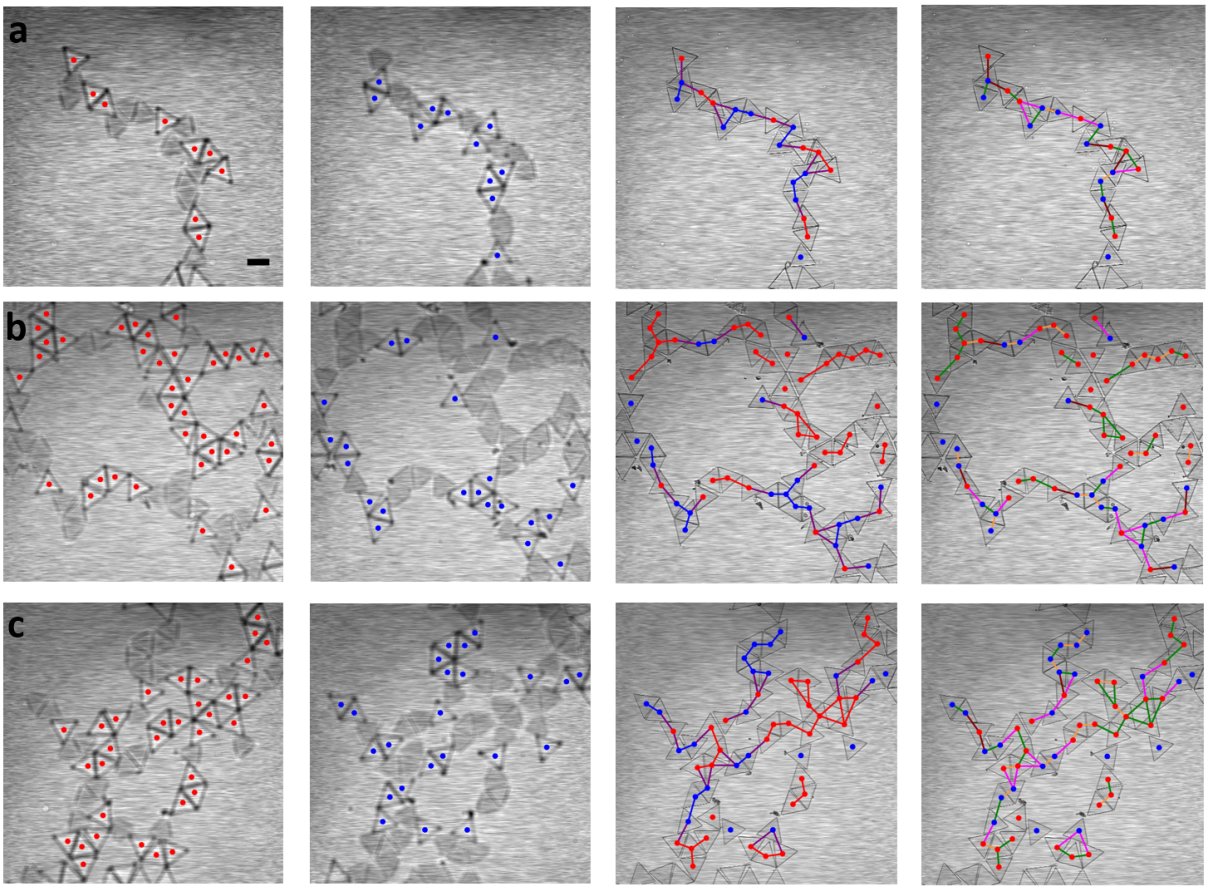

Figure 4.9: Identification of triangular prism binding states ($T/L = 1/25$). Each row of images (a)-(c) represents a different location within a network structure. The relative position of the microscope's focal plane to the air-water interface is varied by column as follows: Column (1): Microscope focal plane is $\sim$200 μm below the interface. In-focus prisms are identified with red markers. Column (2): Microscope focal plane is $\sim$200 μm above the interface. In-focus prisms are identified with blue markers. Column (3): Microscope focal plane is at the interface. Bonds between prisms with the same positional polarity are identified with blue and red connecting lines, bonds between prisms with the opposite positional polarity are identified with purple connecting lines. Column (4): Microscope focal plane is at the interface. Prism-prism bonds are identified by their positional-polarity-independent orientation: side-side (orange connecting lines), tip-tip (green connecting lines), side-side offset (brown connecting lines), tip-side (pink connecting lines). Scale-bar is 100 μm. Reprinted from [109] with permission.

and interface mesh refinements to minimize the interfacial energy subject to specific boundary conditions.

As we will discuss further in Section 4.5, we compute the interface shape given a pinned contact line around a bowed equilateral triangle of side length 120. In particular, this triangle is formed by the intersection of three planes containing great circles with a thin spherical shell. Specifying the behavior of the contact lines yields one set of boundary conditions; the far-field boundary condition is that the interface is flat. To allow for the condition of mechanical equilibrium to be satisfied, we do not explicitly fix the height of the far-field boundary, which, in effect, allows for the relative height between the prisms and the equilibrium, unperturbed height of the interface to change as needed.

In order to generate a potential energy landscape of a pair of interacting triangles, we run Surface Evolver simulations on a regularly-spaced grid in (r, θ_1, θ_2) configuration space, where r is the distance between the centers of the two triangles, θ_1, θ_2 are the orientations of the two triangles (see Figure 11 for their definitions). The parameter ranges are $132 \leq r \leq 360$ and $0^\circ \leq \theta_1, \theta_2 < 360^\circ$, with grid spacing of 12 in distance and 5° in orientation. The actual number of simulations needing to be run is substantially reduced by symmetries inherent in the system. Simulations are run for both particles with the same bowing polarity and opposite bowing polarities.

4.4.2 Computing particle trajectories leading to pair binding

For a particle moving through a fluid at relatively slow speeds and at a low Reynolds number, Re, the drag force is given by $\mathbf{F}_d = -\eta_r \dot{\mathbf{r}}$. Analogously, a particle rotating in a fluid at slow speeds experiences a drag torque, $\tau_d = \eta_\theta \dot{\theta}$. In these equations, η_r and η_θ are the viscous damping coefficients for the center-of-mass and rotational degrees of freedom of the triangular prisms, respectively.

Assuming a quasistatic force balance on the particles, we can equate the corresponding drag and capillary forces to obtain the following system of differential equations of motion

for the pair of prisms. This is a valid assumption to make, as both the Reynolds number $\mathrm{Re} = \rho v a/\mu$, which is a ratio of inertial forces to viscous forces within a fluid, and the capillary number $\mathrm{Ca} = \mu v/\gamma$, which is a ratio of viscous forces to surface tension of an interface, where ρ is the density of the liquid, v is the velocity of the particle, and μ is the dynamic viscosity of the liquid, are quite small[1], so that both inertia and viscous deformation of the interface can be neglected, as in [99, 101]. In this case, hydrodynamic interactions can safely be ignored, and the force balance equations are

$$\eta_r \partial_t r(t) = -\partial_r U(\theta_1, \theta_2, r) \tag{4.4.1}$$

$$\eta_\theta \partial_t \theta_1(t) = -\partial_{\theta_1} U(\theta_1, \theta_2, r) \tag{4.4.2}$$

$$\eta_\theta \partial_t \theta_2(t) = -\partial_{\theta_2} U(\theta_1, \theta_2, r) \tag{4.4.3}$$

Discretizing the time derivative of our desired quantities allows us to iteratively solve for the trajectories of the prisms via

$$r\left(t_i\right) = r\left(t_{i-1}\right) - \frac{1}{\eta_r}\frac{\partial U}{\partial r}\Delta t \tag{4.4.4}$$

$$\theta_I\left(t_i\right) = \theta_I\left(t_{i-1}\right) - \frac{1}{\eta_{\theta_I}}\frac{\partial U}{\partial \theta_I}\Delta t \tag{4.4.5}$$

where $i, i-1$ correspond to the $i^{\text{th}}, (i-1)^{\text{th}}$ time-step, respectively, and $I = 1, 2$ corresponds to the particle. The partial derivatives are taken of an interpolated interaction potential using the potential values determined via Surface Evolver on the regular grid, as discussed previously.

The viscous damping coefficients are not independent constants. They both originate from the interaction between the particle and the surrounding fluid. The center of mass drag η_r actually depends on the particle orientation and the direction of center-of-mass

[1]For a set of characteristic values $\rho = 10^3\,\mathrm{kg/m}^3$, $a = 120\,\mu\mathrm{m}$, $\mu = 1.002 \times 10^{-3}\,\mathrm{Pa\ s}$, $\gamma = 72 \times 10^{-3}\,\mathrm{N/m}$, and $v \sim 4 \times 10^{-4}\,\mathrm{m/s}$, which is representative of the upper range of velocities observed in the dilute binding events, $\mathrm{Re} \approx 0.048$ and $\mathrm{Ca} \approx 5.6 \times 10^{-6}$, both of which are small compared to unity.

motion. To our knowledge there is no literature on fluid drag of triangular prisms, so in this study we make a simplifying assumption that both η_r and η_θ are constants, and we estimate their magnitude by considering the following first-principles calculation: The work done over a small linear translation of Δr due to the drag force is $W_l = F_d \Delta r$, while the work done over a small rotation by $\Delta\theta$ (in radians) due to the drag torque is given by $W_r = \tau_d \Delta\theta$. We can attribute the work done by each drag to the energy required to move the fluid due to the particle's motion. If we keep the small distance traversed by a single tip of the (equilateral) triangle the same in both cases, Δr, then the amount of rotation associated with that movement is given by $\Delta\theta = \Delta r/c$, where c is the distance from the centroid to the tip. If the equilateral triangle has a side length of s, then $c = s/\sqrt{3}$. Comparing these two cases, the amount of fluid that is moved is of the same order, which means that we can equate the two works. We also assume that these two motions took the same amount of time, Δt. In this case,

$$\eta_r \frac{\Delta r}{\Delta t}\Delta t = \eta_\theta \frac{\Delta\theta}{\Delta t}\Delta t \tag{4.4.6}$$

so that the ratio between the two drag coefficients is

$$\frac{\eta_\theta}{\eta_r} = \left(\frac{\Delta r}{\Delta\theta}\right)^2 = c^2. \tag{4.4.7}$$

For angles measured in degrees, the associated drag coefficient is $\eta_{\tilde{\theta}} = \eta_\theta(\pi/180)^2$, and the ratio becomes

$$\frac{\eta_{\tilde{\theta}}}{\eta_r} = \left(\frac{\Delta r}{\Delta\tilde{\theta}}\right)^2 = c^2\left(\frac{\pi}{180}\right)^2. \tag{4.4.8}$$

For a side length of $s = 120$, $c = 69.3$ and, thus, $\eta_{\tilde{\theta}}/\eta_r = 1.46$.

4.4.2.1 Theoretical power-law relation for dilute binding trajectories

For an experimental system exhibiting pairwise binding due to capillary interactions, a useful method to characterize the resultant trajectory is to record the separation distance r as a function of time-to-contact, $t_c - t$, where t_c is the first instance where the particles

touch. If the trajectory obeys a power-law relation such that

$$r = (t_c - t)^{\beta}, \tag{4.4.9}$$

the value of the exponent β gives insight into the order of the capillary interaction, as we will presently show.

The capillary interaction energy between two ideal multipoles is $U_{12} \sim r^{-\alpha}$, where $\alpha = 4$ for an interaction between two ideal quadrupoles and $\alpha = 6$ between two ideal hexapoles (and, in general, $\alpha = 2m$ for an interaction between two multipoles of order m). Thus, the capillary force, for fixed orientations, is

$$F_{12} = -\frac{\partial U_{12}}{\partial r} \sim r^{-(\alpha+1)}. \tag{4.4.10}$$

Equation the capillary force to the viscous drag force $F_d = \dot{r}(t)$, as we did in the previous section, yields a simple first-order differential equation

$$\frac{dr}{dt} \sim r^{-(\alpha+1)}. \tag{4.4.11}$$

Solving this differential equation gives $t_c - t \sim r^{\alpha+2}$; comparing this to Eq. (4.4.9) yields the result that, for a capillary interaction between two capillary multipoles of order m, the power-law exponent is

$$\beta = \frac{1}{\alpha+2} = \frac{1}{2(m+1)} = \begin{cases} 1/6 & \text{quadrupole} \\ 1/8 & \text{hexapole} \end{cases} \tag{4.4.12}$$

4.5 Capillary interactions of triangular prisms

The triangular prisms in this experiment have flat, nearly vertical side surfaces. This lack of curvature of side surfaces leads to a different interface attachment than that of ellipsoids

and cylinders. As discussed in [99, 101, 111, 112], interfaces around the ellipsoids and cylinders either rise or depress as a result of the differing curvatures of the side surface of the particle, maintaining a constant contact angle and zero total force and torque on an isolated particle.

For these triangular prisms with vertical side surfaces, the preferred contact angle of the material cannot be reached, as that would correspond to a uniform rise of the interface around the triangular prism, yielding a net force pointing up on the particle that is not consistent with mechanical equilibrium. Therefore, instead of an equilibrium contact line in the middle of the side surface of the triangular prisms, the interface is pinned to either the top or the bottom edges of the triangular prisms, as discussed more generally in Sec. 4.2.3.

To characterize the interface shape and the resulting capillary interaction between the triangular prisms, we use Surface Evolver to compute the interface with a contact line pinned to the edges of a bowed triangle. To match the observed curvature of the thinnest particles, we use an radius-of-curvature-to-edge-length ratio of 0.9 (thus, for an edge length of 120 μm, we take the radius of curvature to be 108 μm). The resulting interface around isolated particles (Figs. 4.10a,b) closely resembles that observed in the eSEM images of the thinnest $T/L = 1/50$ particles (Fig. 4.8).

It is worth noting that the only input into the Surface Evolver computation is the pinned contact line, and no information regarding the particle thickness is involved. Our computations show that, for a bowed-up particle (Fig. 4.10a), the particle center of mass is below the infinitely-far interface height by 7.45 μm (for the above-specified curvature), whereas the center of mass of a bowed-down particle is the same amount above the far interface height. This depth is greater than the particle thickness (2.5 μm for $T/L = 1/50$ and 5 μm for $T/L = 1/25$), and helps explain the perfect correlation between the polarity and the direction of the particle bowing of the thinnest particles. The relation between the interface attachment and the bowing direction of the thicker particles may involve more complicated mechanisms that need further investigation.

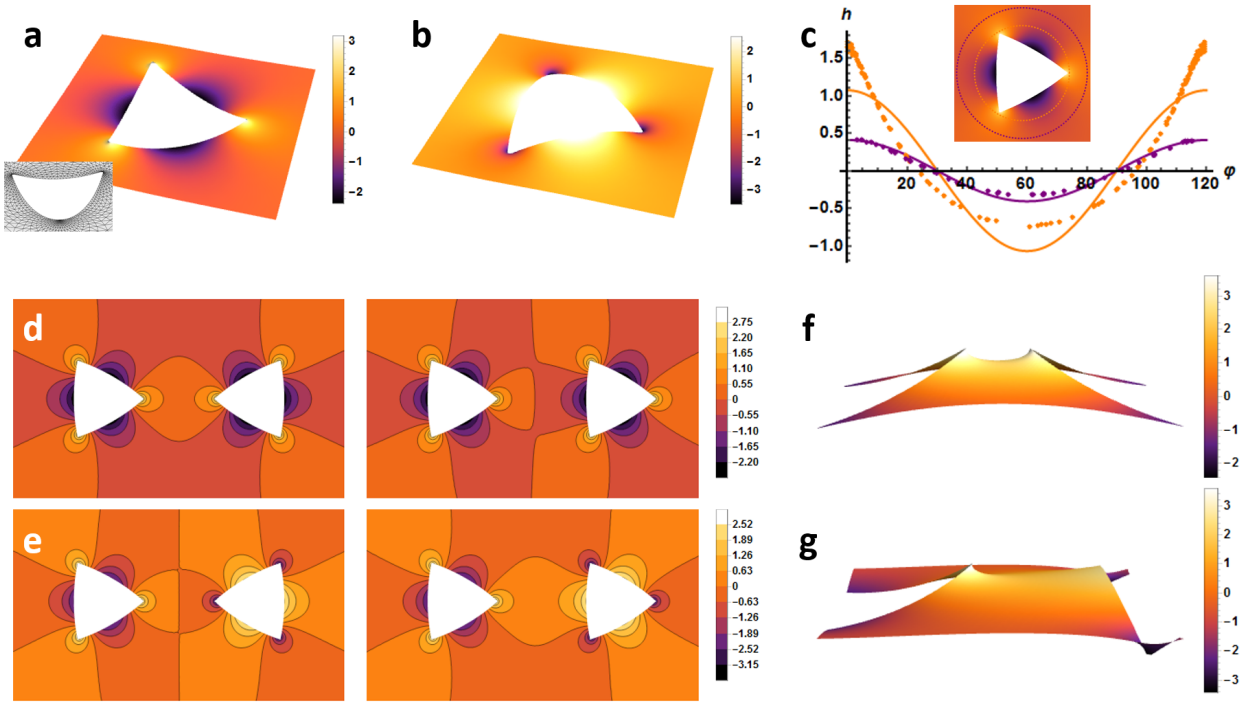

Figure 4.10: Interface height profile for a (a) bowed-up triangular prism and a (b) bowed-down triangular prism, where the zero value is set by the equilibrium interface height at large distances from the prism. The inset in (a) is a close-up of the Surface Evolver simulation output. (c) A comparison of the interface height profile around a bowed-up triangular prism (data points) and an ideal hexapole (solid curves) as a function of angle at two different distances from the triangular prism, shown in the inset. Simulated interface height profiles for (d) two bowed-up triangular prisms and (e) one bowed-up and one bowed-down prism for both tip-to-tip and tip-to-side configurations. Zoomed-in rendering of simulated interface height profile for (f) a tip-to-tip configuration for two bowed-up prisms; and (g) a tip-to-side configuration for one bowed-up and one bowed-down prisms, illustrating the existence of a capillary bridge in both cases.

The interface geometry around the triangular prisms is similar to that of the capillary hexapole in that there are six distinct regions of alternating positive- and negative-height interface values (where the equilibrium, unperturbed height of the interface at far distances is taken to be zero). However, important differences exist between the ideal hexapole field and the interface around the triangular prisms at distances close to the particle. The ideal hexapole, with a interface height profile governed by Eq. (4.2.22), has the symmetry that the positive and negative regions are of equal width. The interface around the triangular prisms, in contrast, has much narrower positive (negative) regions around the tip of the bowed-up

(-down) triangles (Fig. 4.10c). As a result, the focusing of excess area around the tips of the triangles induces stronger capillary interactions at the tips than along the triangle edges. Note that, as one would expect, the height of the interface around a bowed triangular prism increasingly conforms to the profile of a capillary hexapole as the distance from the prism increases. Indeed, the effect of tips, edges, and other sharp particle features, which are quite prominent in the near-field behavior of the interface, becomes increasingly diminished and smoothed out at these larger distances (Fig. 4.10c).

We then study the capillary interaction potential between triangular prisms by computing the interface geometry around a pair of triangular prisms using Surface Evolver. Once the numerical interface solution has been obtained, we can subsequently determine the capillary interaction energy using Eq. (4.2.16). There are, of course, two cases that are simulated: the first is when both prisms have the same bowing polarity (by symmetry, we need only consider the case where both particles are bowed up), and the second is when the two particles have opposite polarities (here again we can simplify matters and consider only the case where the particle on the left is bowed up and the particle on the right is bowed down). Examples of the interface in the vicinity of two triangular prisms with the same and opposite polarities are shown in Figs. 4.10d,e.

It is already evident from these plots – even before further analysis – that the tip-tip configuration for prisms with the same polarity and the tip-edge configuration for prisms with opposite polarities are attractive, while the opposite configurations are repulsive – the former will result in decreased excess area as the particles move towards each other, while the latter will result in increased excess area (the overall slope of the interface will increase between the bowed-up and bowed-down components as they are brought closer together). Figs. 4.10f,g show the underlying mechanism that reduces the excess area between regions with the same capillary charge: the formation of a capillary bridge.

The capillary interaction potential U depends on both the distance between the centers of the two triangular prisms, r, and their orientations relative to the line connecting their

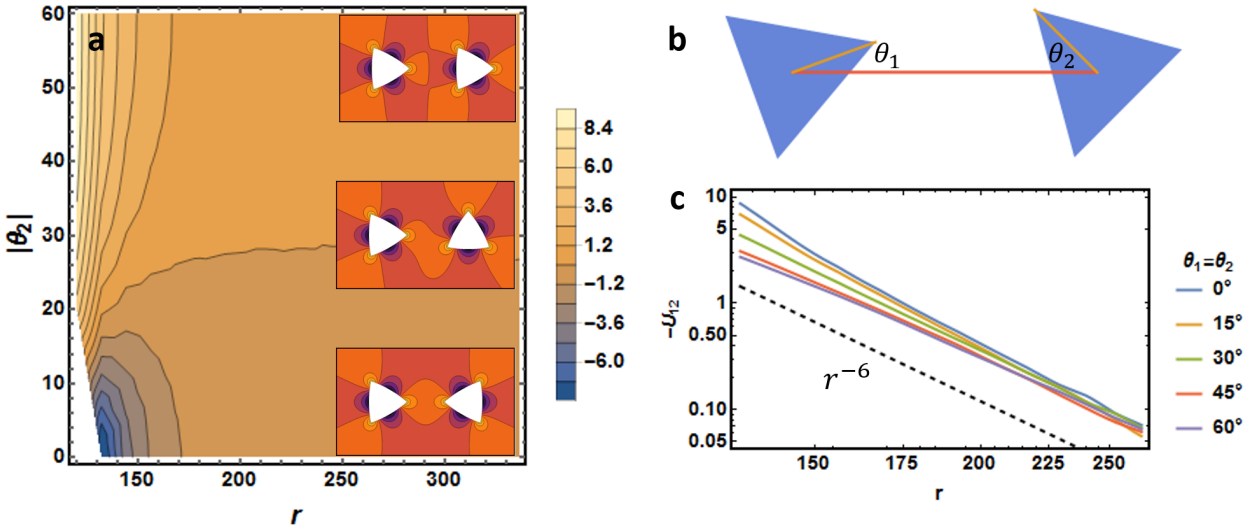

Figure 4.11: Numerically-simulated capillary interaction potential between two bowed-up triangular prisms, with the left prism held at 0°. This two-dimensional slice of the full three-dimensional configuration space is directly comparable to the theoretical interaction potential in Fig. 4.3. (b) All orientation angles for the triangular prism system are defined according to the convention shown: the orientations are defined by the angle a specific tip of the prism makes with the line connecting the centers of the two prisms. (c) The capillary interaction potential for two-bowed up triangular prisms in mirror-symmetric configurations as a function of the separation distance, r, on a log scale, for various orientation angle values. A dashed reference line, corresponding to the theoretical interaction potential for two ideal hexapoles, $U \sim r^{-6}$, is shown for comparison.

centers, θ_1, θ_2 (see Fig. 4.11b for an illustration of the convention used). This is a configuration space that has one extra dimension beyond that of the capillary hexapolar theory, in which only the relative orientation of the two particles mattered. In order to be able to directly compare the theoretical case with that of two bowed-up triangular prisms, we fix the orientation of the left particle to be 0° and allow r and θ_2 to vary. The resultant potential, shown in Fig. 4.11a, is very similar to that of the ideal hexapoles; even the general shape of the interface, as shown in a few select cases as insets in both plots, shares similar features.

The similarities extend beyond this, as well: in Fig. 4.11c, when comparing potential curves for various mirror-symmetric configurations in the triangular-prisms system with that of the mirror-symmetric curve in the ideal-hexapoles system, which has a $U \sim r^{-6}$ dependence, we see that all the curves approach the theoretical ideal-hexapole curve at long

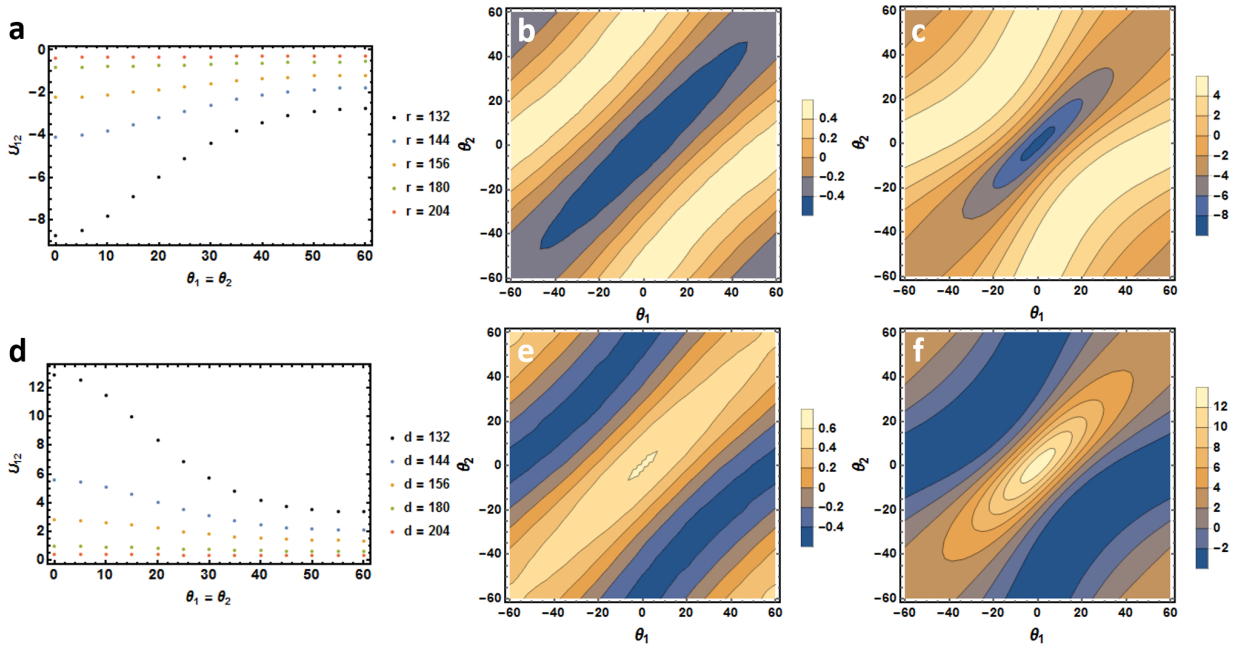

Figure 4.12: (a) Interaction energy potential values for two bowed-up triangular prisms in mirror-symmetric configurations at various separation distances. 0° corresponds to a tip-to-tip configuration, while 60° corresponds to a side-to-side configuration. Interaction energy potentials plotted as a function of orientation angles for (b) $r = 192$ and (c) $r = 132$. (d)-(f) The corresponding figures for the case of one bowed-up and one bowed-down triangular prism.

distances. Again, this makes sense: as noted before, the interface shape around an isolated triangular prism approaches that of a pure hexapole as the distance from the prism increases; as the distance between two triangular prisms increases, the interaction increasingly becomes that of between two capillary hexapoles. Deviations from the pure-hexapole curve and from each other occur at short inter-particle distances, where the anisotropic tips become increasingly prominent. Note that the $\theta_1 = \theta_2 = 0°$ tip-tip mirror symmetric configuration is favored for these smaller distances.

This deviation from an ideal hexapole is further portrayed in Fig. 4.12. In the case of pure ideal hexapoles, since the interaction energy depends only on the relative orientations of the particles, the interaction energy for all mirror symmetric configurations, in which $\theta_1 = \theta_2$, for a given distance is perfectly degenerate. As shown in Figs. 4.12a,d, for the system of triangular prisms, however, the tip-tip mirror symmetric configuration (corresponding to

$\theta_1 = \theta_2 = 0°$) is strongly favored (disfavored) compared to the edge-edge mirror symmetric configuration (corresponding to $\theta_1 = \theta_2 = 60°$) for smaller values of inter-particle distances, r, in the same- (opposite-) polarities system. In the case of opposite polarities, even though the edge-edge configuration is preferred over the tip-tip configuration, it is important to realize that it is *not* the global preferred state, which is a non-mirror-symmetric configuration, as will be discussed further subsequently. Once again, in both cases, the expected ideal-hexapole behavior of degenerate energies for all mirror symmetric configurations is recovered as the inter-particle distance is increased.

As shown in 4.12b,c, the potential for a pair of bowed-up triangular prisms shows a clear well for the mirror symmetric configuration, $\theta_1 = \theta_2$, which becomes increasingly deep for smaller inter-particle distances. It is clear in 4.12b, as well, that for two bowed-up triangular prisms, the potential is relatively flat for all mirror symmetric configurations at a given large distance, which is the same as the ideal hexapole interaction. When the two prisms are close to each other, however, the tip-to-tip configuration is much more preferred, in contrast to the ideal hexapole interaction.

The above results indicate that when two bowed-up particles approach one another, in general, they first rotate into mirror-symmetric configurations, and then rotate to a tip-to-tip configuration when they are very close to each other. The case of two bowed-down triangular prisms is very similar to the above discussion for the bowed-up case, with the simple addition of a minus sign to the interface height, which results in the same interface energy.

The case of one bowed-up triangular prism and one bowed-down triangular prism is quite different. At large distances, the capillary interaction is close to that between two hexapoles but with one hexapole rotated by 60° degrees (or, equivalently, the "+" and "−" capillary charges interchanged). Interestingly, at small distances, instead of favoring a particular configuration (such as tip-to-tip for the bowed-up pairs), the potential energy valley appears curved in (θ_1, θ_2)-space while slightly favoring the offset edge-edge configuration (4.12e). As we will see below, this leads to different binding trajectories for bowed-up pairs and bowed-

up-bowed-down pairs.

4.6 Dilute binding events

4.6.1 Experimental results

Seven dilute-binding trajectories (five for $T/L = 1/25$ and two for $T/L = 1/50$) were collected (see Fig. 4.13 for representative optical microscopy time lapses and see Figs. 4.14 and 4.15 for visualization of all trajectory data). Four of the trajectories resulted in bindings consistent with same-polarity prisms, while three trajectories resulted in bindings consistent with opposite-polarity prisms. Qualitative features apparent in the dilute binding trajectories are: (i) same-polarity particles, in a first stage, adopt mirror-symmetric configurations and slowly move toward each other; in a second stage, particles rapidly close into a tip-tip binding; and in a third, some particles subsequently rotate into an edge-edge configuration; (ii) opposite-polarity particles also initially show a mirror symmetric orientation; particles then later approach to a tip-edge-midpoint configuration; the pair finally collapsed into an offset edge-edge bond.

The power-law exponent associated with particles approaching each other in these binding events, $r \sim (t_c - t)^{\beta}$, where t_c is the time of contact, defined as the first image frame in which the two prisms touch, displays similarity with the exponent from ideal hexapole-hexapole interactions, $\beta_0 = 1/8$ (Fig. 4.14). The small deviation comes from the difference between the actual capillary interactions between the triangles and the ideal hexapolar interaction. In particular, at far distances, β appears to be closer to 1/6, indicating that at far-field, quadrupolar interactions (due to higher-order contact-line undulations generated from surface roughness and other potential variations in the prism edges) may be the dominant far-field capillary attraction mechanism.

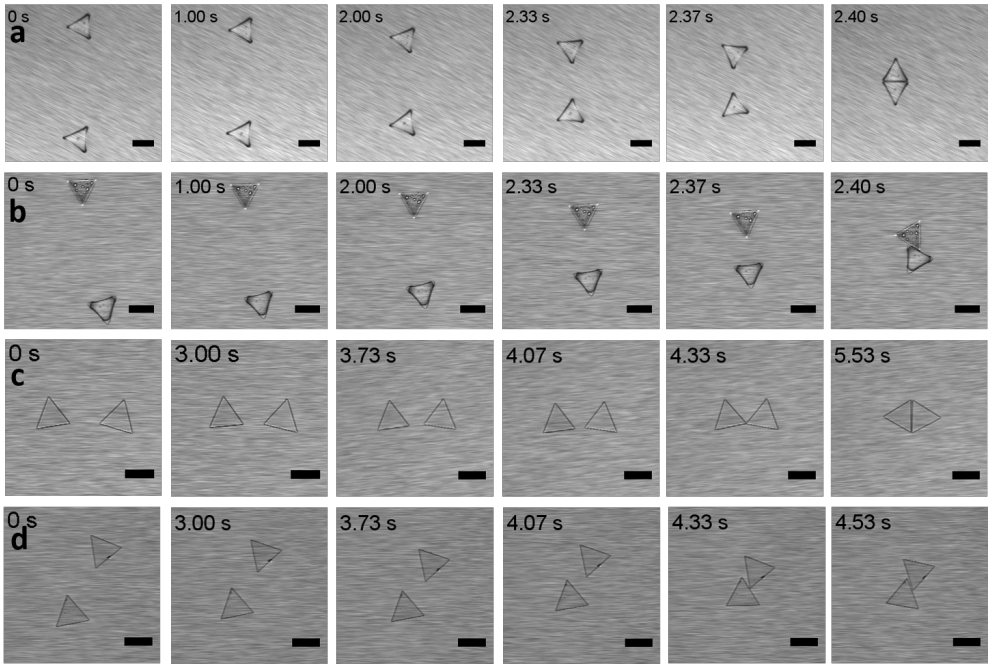

Figure 4.13: Optical microscopy images of the 2 types of binding trajectories observed for polar prisms ($T/L \leq 1/10$), shown for $T/L = 1/50$ (rows (a) and (b)) and $T/L = 1/25$ (rows (c) and (d)). For prisms of $T/L = 1/50$ (rows (a) and (b)), contact occurs between the 5th and 6th images of each row. For prisms of $T/L = 1/25$ (rows (c) and (d)), contact occurs in the 5th image of each row. Rows (a) and (c), tip-to-tip binding trajectory: the prisms approach and first contact occurs at the tips. The prisms then rotate into a collapsed, fully flush edge-to-edge orientation. Rows (b) and (d), tip-to-midpoint edge binding trajectory: the prisms approach and contact one another in an orientation such that the tip of one prism binds at the midpoint of the other prism's edge. The prisms then rotate into an edge-to-edge orientation in which the two edges are offset from each other by $L/2$. Scale bars are $100\,\mu$m. Reprinted from [109] with permission.

4.6.2 Simulation results

To compare to these experimental results, we simulated pair-binding events using the interaction potential (interface energy) $U(\theta_1, \theta_2, r)$ obtained by interpolating a grid of Surface Evolver-calculated potential values at regular intervals as described above. Details of the trajectory simulations are described in Section 4.4.

Examples of our simulation results for same-polarity (both bowed up in our calculation) and opposite-polarity prisms are shown in Fig. 4.14 and Fig. 4.15, respectively. Initial conditions were chosen to be close to those observed in experiment. The ratio of the two

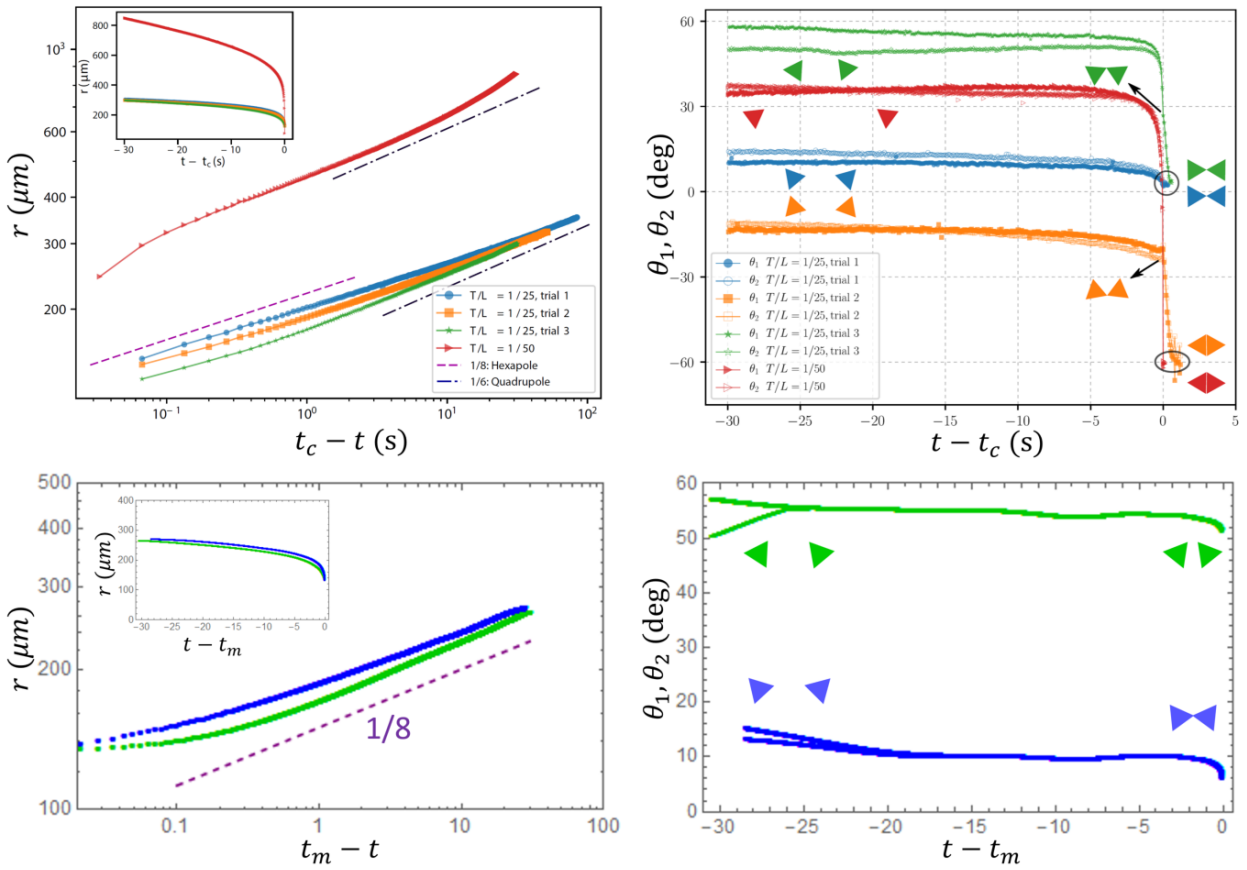

Figure 4.14: Comparison of experimentally observed and simulated trajectories for a pair of triangular prisms of the same polarity. Top row: observed r vs. $t_c - t$ curves in log-log scale (left) and linear scale (inset), where t_c is taken to be the first frame in which the two prisms touch in each event; and observed θ_1, θ_2 vs $t - t_c$ curves (right). Four events are shown as explained in the legend, and lines showing $\beta = 1/8$ (consistent with hexapolar interaction) and 1/6 (consistent with quadrupolar interaction) are added. Illustrations of the prism configurations are added in the θ_1, θ_2 plot to show the geometry. Configurations at the time of contact ($t = t_c$) are pointed to by arrows, and the points at $t - t_c > 0$ show prism rotations after contact, with final configurations marked by circles. Bottom row: counterparts of the r and θ_1, θ_2 plots from simulation. Instead of contact time, t_m is the time where the separation distance reaches $r_m = 132\,\mu$m (the lower bound of r in our computation), at which the prisms touch if $\theta_1 = \theta_2 = 0$. We have chosen initial conditions that are close to two experimental trajectories.

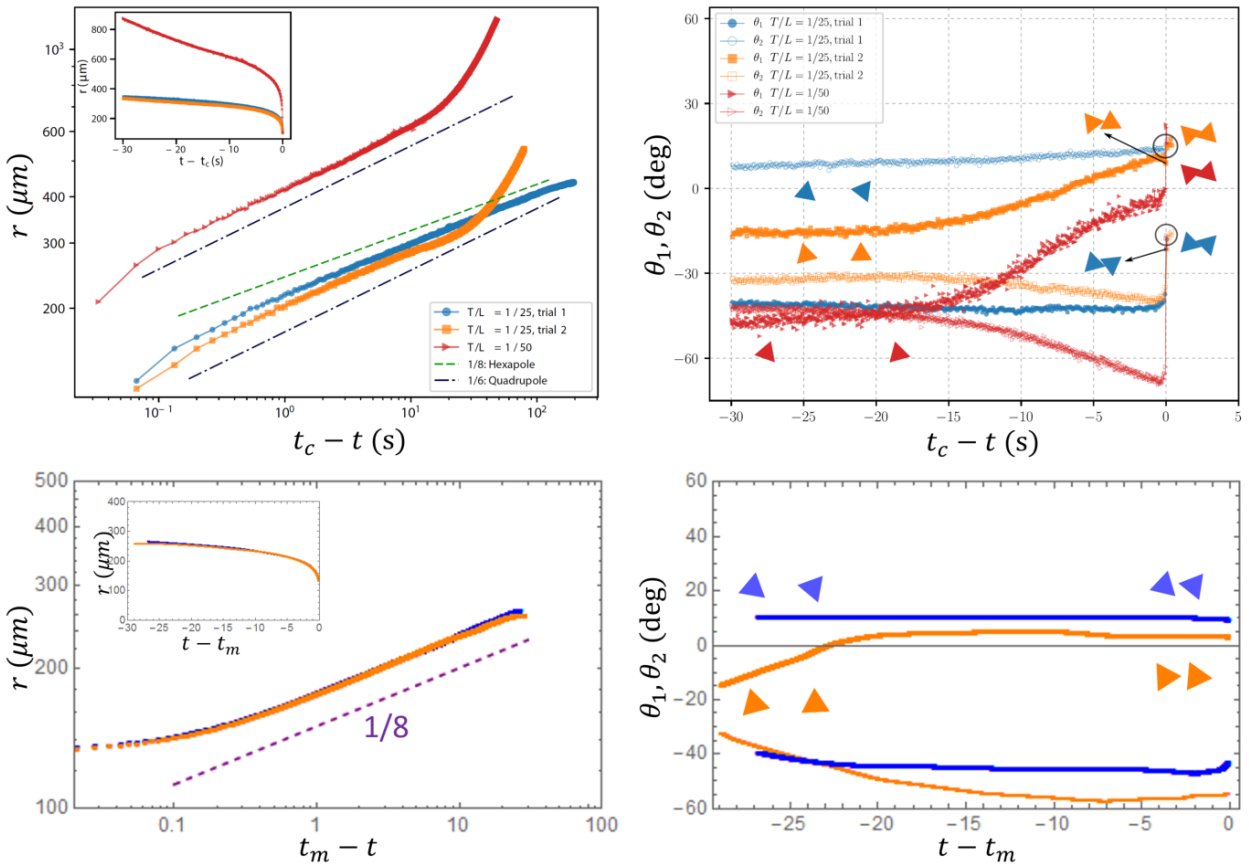

Figure 4.15: Comparison of experimentally observed and simulated trajectories for a pair of triangular prisms of opposite polarities. Top row: experimental observations. Bottom row: simulation results. All conventions are the same as in Fig. 4.14. Note that in two experimental events, the prisms approach faster in the far-field regime than quadrupolar interactions would dictate, which we believe to be due to some accidental drift of the interface.

viscous-damping coefficients is taken be to $\eta_{\tilde{\theta}}/\eta_r = 1.46$ (see Section 4.4), and η_r is chosen to rescale time such that the arbitrary time scale in the simulation is similar to the experimental time scale in the unit of seconds. These simulations terminate at $r_m = 132\,\mu$m, the distance at which the two prisms would touch if they faced one another tip-to-tip. A reference line of $r \sim (t_c - t)^\beta$, where $\beta = 1/8$, is also plotted. In all cases, the trajectories are roughly consistent with that of the ideal hexapole-hexapole case, with the expected deviations occurring as the separation distance decreases.

It is also useful to see the effect of various viscous-damping ratios, $\eta_{\tilde{\theta}}/\eta_r$. Three representative initial conditions, corresponding to configurations close to (but purposefully not

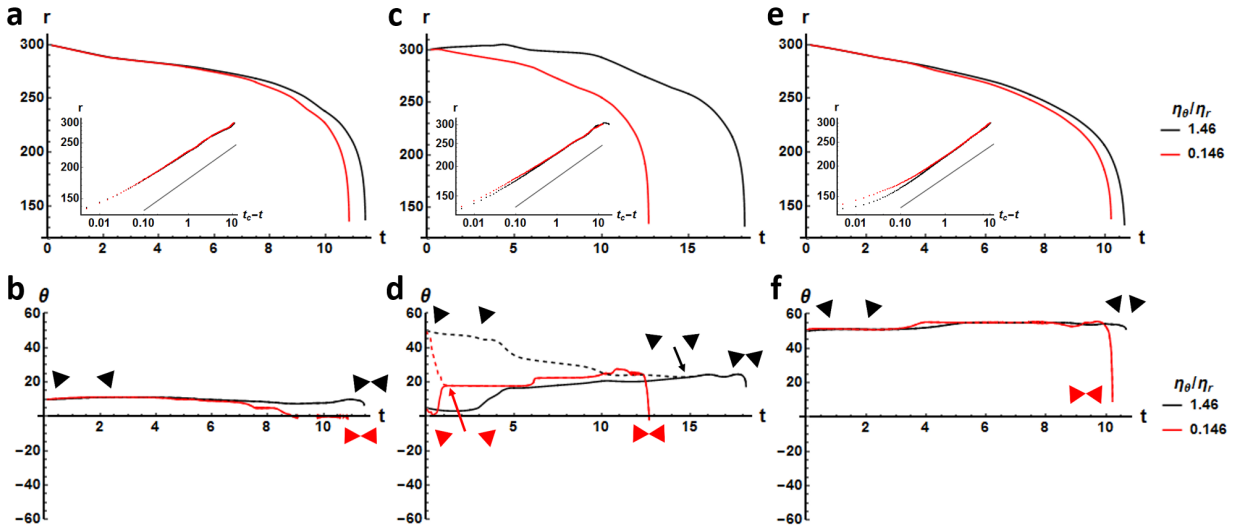

Figure 4.16: Configuration trajectories for three representative initial conditions (close to (a),(b) tip-to-tip, (c),(d) tip-to-edge, and (e),(f) edge-to-edge) and two different viscous-damping coefficient ratios. The top row shows the separation distance as a function of simulation time, with insets plotting separation distance values as a function of time-to-contact on a log scale. The gray reference line corresponds to the theoretical case of two ideal hexapoles approaching each other in a mirror-symmetric configuration. The bottom row shows the orientation angles of the triangular prisms as a function of simulation time.

exactly) tip-to-tip, tip-to-side, and side-to-side were selected, and the resultant simulated trajectories are shown in Fig. 4.16 for two different viscous-damping coefficient ratios, $\eta_{\tilde{\theta}}/\eta_r = 1.46, 0.146$. In all three sets of trajectories, it is clear that mirror symmetric configurations are preferred – for cases where the initial configuration is already mirror symmetric, the subsequent configurations remain mirror symmetric; otherwise, the particles will first rotate to a mirror symmetric configuration. For smaller ratios and fixed η_r, $\eta_{\tilde{\theta}}$ becomes correspondingly smaller, meaning that it is easier for the particles to rotate. This accounts for the fact that, in all cases, the $\theta_1 = \theta_2 = 0^\circ$ tip-tip mirror-symmetric configuration is more easily achieved for the smaller ratio value.

To obtain statistics of how the triangular prisms bind together, we ran simulations for all initial angles of prism pairs at an initial distance of $r_0 = 264\,\mu$m; our results are summarized, for the two different ratio values, $\eta_{\tilde{\theta}}/\eta_r = 1.46, 0.146$, in Figs. 4.17a,b. The first ratio is chosen according to the simple estimate discussed above. The second ratio, which is 10 times

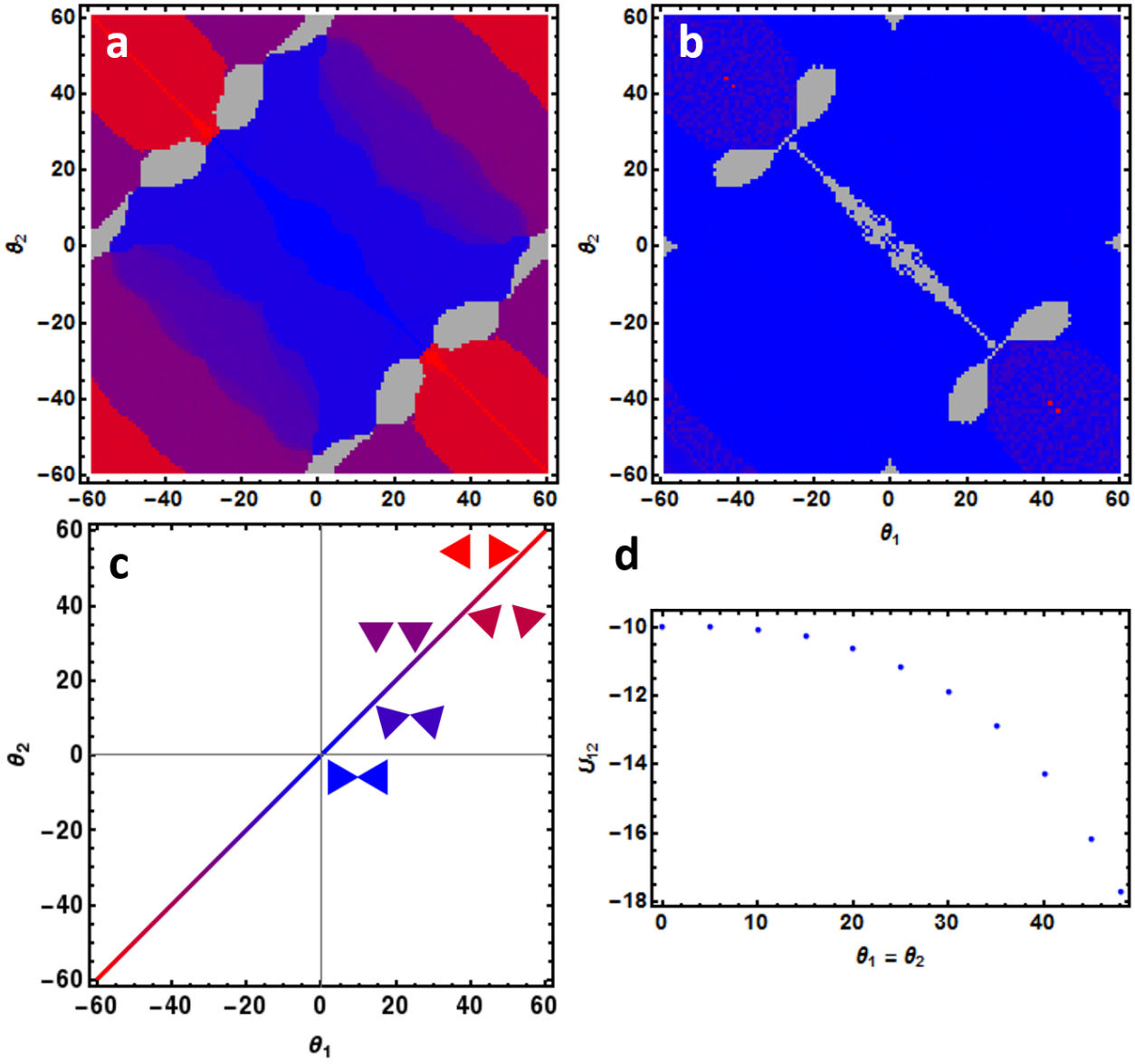

Figure 4.17: "Phase" diagrams illustrating the final configurations ($r = 132\,\mu$m) for all possible initial orientations for two bowed-up triangular prisms at $r = 264\,\mu$m for two different viscous-damping coefficient ratios, (a) $\eta_{\tilde{\theta}}/\eta_r = 1.46$ and (b) $\eta_{\tilde{\theta}}/\eta_r = 0.146$. The final configurations are all mirror-symmetric and lie somewhere along the line in (c), with blue corresponding to tip-to-tip final configurations, red corresponding to side-to-side final configurations, and gray denoting initial conditions that lead to trapped configurations which are due to artificial kinks in the computed pair potential. (d) Capillary interaction potential values for mirror-symmetric configurations with two tips of the triangular prisms remaining in contact (thus, the separation distance, r, decreases below $132\,\mu$m as $\theta_1 = \theta_2$ increases. The potential indicates a tendency for tip-to-tip configurations to ultimately collapse to side-to-side configurations.

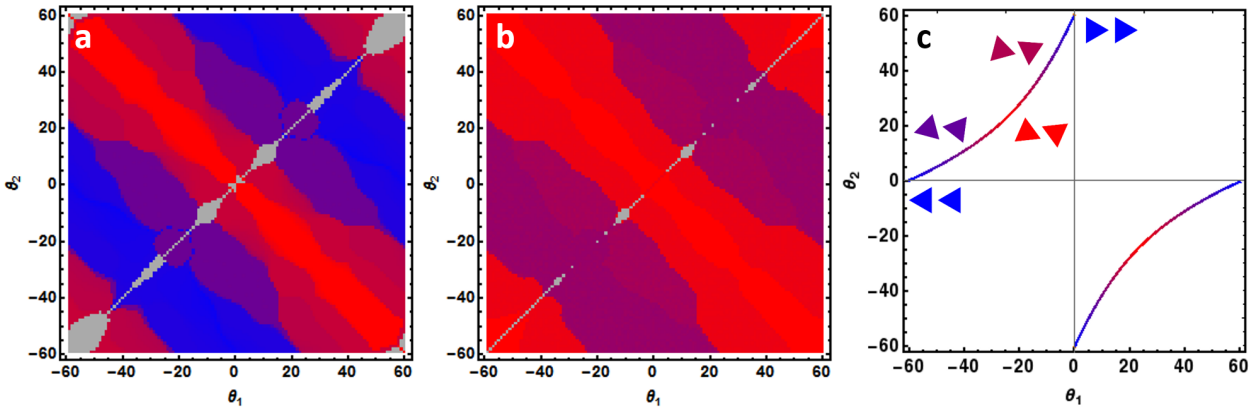

Figure 4.18: "Phase" diagrams illustrating the final configurations ($r = 132\,\mu$m) for all possible initial orientations for one bowed-up and one bowed-down triangular prism at $r = 264\,\mu$m for two different viscous-damping coefficient ratios, (a) $\eta_{\tilde{\theta}}/\eta_r = 1.46$ and (b) $\eta_{\tilde{\theta}}/\eta_r = 0.146$. The final configurations lie somewhere along the curve in (c), with blue corresponding to tip-to-edge final configurations and red corresponding to offset-edge-to-edge final configurations.

smaller, allows the prisms to rotate faster relative to their center-of-mass motion, and shows interesting contrast to the first case. In both cases, a significant majority of configurations end up in, or close to, the $\theta_1 = \theta_2 = 0°$ tip-tip mirror-symmetric configuration. For the case of $\eta_{\tilde{\theta}}/\eta_r = 1.46$, some trajectories end up along a continuum of mirror symmetric configurations ranging from tip-to-tip to edge-to-edge, as the prisms did not have enough time to finish the rotation before they contact. Contrastingly, in the second case with $\eta_{\tilde{\theta}}/\eta_r = 0.146$, almost all trajectories end up tip-to-tip, because rotational drag is smaller, leading to faster rotation. A small fraction of initial conditions (gray in the figure) ended up in random configurations coming from small kinks in the pair potential due to numerical error.

In order to investigate what happens after the two prisms touch at their tips, we calculated the pair potential for two prisms with their tips touching but at different orientations (mirror symmetric configurations $\theta_1 = \theta_2$ with the angles ranging between 0 and 60), as shown in Fig. 4.17c. The lower potential for larger angles indicates that, after the initial tip-to-tip contact, the pair of triangular prisms will rotate and "collapse" into an edge-to-edge configuration. It is worth pointing out that although, after collision, the prisms ultimately collapse into the edge-to-edge configuration, a majority of trajectories still first go through an initial tip-tip

binding. This is in good agreement with our experimental observations.

For bowed-up-bowed-down pairs, a similar set of simulations yield results shown in Figs. 4.18a,b for the two viscous-damping coefficient ratios. In this case, it is important to note that the final configurations are not mirror symmetric; Fig. 4.17c shows the final orientation values for the two triangular prisms. The curves of final orientation lie along the minimum-energy regions of the opposite-polarity interaction potential in Fig. 4.12. Similar to the same polarity case, the second case with the smaller drag coefficient ratio, $\eta_{\tilde{\theta}}/\eta_r = 0.146$, leads to a more uniform phase diagram where all initial conditions have enough time to rotate to the offset edge-to-edge configuration, which is of lower energy. The first case with the ratio as determined from our geometric estimation, $\eta_{\tilde{\theta}}/\eta_r = 1.46$, yields a continuum of final configurations. As before, our simulation terminates at $r_m = 132\,\mu$m, the distance at which the two prisms would touch if they faced one another tip-to-tip. The opposite-polarity prisms, however, are in non-tip-to-tip configurations such that the prisms are not touching yet. Our additional computations of the interface energy shows that, at smaller distances, the offset edge-to-edge configurations exhibit lower energy, leading to the final collapsed offset edge-to-edge configurations as observed in experiment.

4.7 Discussion

In this work, we have observed experimentally and corroborated numerically that bowing in triangular prisms can create a hexapolar-like interaction that favors highly-directional binding events involving a tip of at least one particle. Specifically, for two particles of the same polarity, a significant majority of binding events are found to first bind via a tip-to-tip interaction in our simulations before ultimately collapsing to a lower-energy edge-to-edge state. This is due to the fact that the focused deformation of the interface near the tips of the prisms yields a strong pathway for rapidly reducing excess interfacial area – that is, the steepest gradient generally can be found in the direction of tip-to-tip binding. Even with the

final collapse, which should be conducive to the formation of close-packed structures, large-scale disordered networks are nevertheless quite successfully formed. This is most likely due to geometric frustration from neighboring prisms, which is partly caused by differing preferred binding sites between particles with the same polarity and particles with opposite polarities. Perhaps a sample of particles all with the same polarity would more efficiently collapse and form a close-packed structure.

In attempting to create an *ordered* open network such as the kagome lattice, isolating particles of a single polarity is undoubtedly the first step. However, as just alluded to, a barrier to collapse needs to be introduced to stabilize the tip-to-tip contact. One potential way to do this would be to slightly truncate the the tips of the triangles, which would create a (shallow) stabilizing local minimum in the profile of the interaction potential as a function of collapse angle. Of course, the truncation cannot be too large so as to destroy the hexapolar interaction, as that is crucial to the prominence of the tip-to-tip binding pathway. Ultimately, it seems as though the self-assembly of triangular particles through capillary interactions is a promising direction towards efficiently creating open structures with novel properties.

CHAPTER V

Conclusion

In this dissertation, we have explored a number of topics related to critical mechanical structures and their inherent mechanical instability. We have shown how characteristics of mechanical instability, manifesting in the form of floppy modes, can interact with thermal fluctuations to create intriguing and sometimes somewhat unexpected mechanical properties, especially at small scales. We have also examined a few different experimental systems that can yield open structures, which are intimately related to critical mechanical structures in that their openness leads to accessible deformations that are manifestations of instability. Our study of various aspects of self-assembly can help to improve the likelihood of engineering long-lasting open structures that have novel and useful properties.

In Chapter II, we explored the finite-temperature buckling of an extensible rod, and showed that thermal fluctuations delay the buckling transition, stabilizing the straight-rod phase. In Chapter III, we studied the structural phase transition between two open structures, the kagome lattice and the twisted kagome lattice, and showed that thermal fluctuations entropically stabilize the kagome phase due to a large number of near-floppy modes that give a near-divergent contribution to the free energy and, thus, renormalize the twisting modulus of the kagome lattice, which also drives the transition to be first-order, in contrast with the continuous nature of the zero-temperature structural transition. We also proposed an experimental manifestation of this transition in the form of self-assembling triblock Janus

particles with one offset attractive patch. For an expedient choice of attractive patch size and offset angle, a twisted kagome assembly can be spontaneously formed rather than a kagome assembly, though there is a region of the phase diagram in which a transition between the two can be controlled via temperature.

It is worthwhile to note that the buckling transition of Chapter II remained second-order at finite temperature, whereas the twisting transition of Chapter III became first-order. The reason for this difference is that, in the former case, only a single mode became floppy, whereas in the latter case, a sub-extensive number of modes became floppy. A similar driving mechanism to a first-order transition is encountered in the square lattice transition in [13], which also has a sub-extensive number of floppy modes.

Finally, in Chapter IV, we analyzed the pairwise binding and self-assembly into an open structure of thin, triangular prisms, created in the lab of our experimentalist collaborators, Joseph Ferrar and Michael Solomon. We found that these prisms, which undergo bowing (in both directions) during synthesis, generate capillary interactions that are similar to hexapole in nature due to contact-line pinning that follows the bowing of the particles. These interactions lead to highly-directional pairwise binding in which particles with the same bowing polarity bind together tip-to-tip, while particles with opposite bowing polarities bind together tip-to-edge. In both instances, collapse to a shared-edge configure typically occurs; nonetheless, the resultant large-scale disordered structures that form from this self-assembly are open structures.

5.1 Future directions

When trying to fabricate mechanical metamaterials and open structures at small scales, thermal fluctuations are necessarily prominent and top-down production can be difficult and tedious – hence, an automated, bottom-up process such as self-assembly is highly desirable. Therefore, there are certainly future directions in which research can continue in these areas.

As discussed at the beginning of Chapter III, topological mechanics is currently a burgeoning field, as properties that are topologically-protected are robust against local perturbations. Therefore, it would be quite promising to combine self-assembly techniques with topological properties. Since the deformed kagome lattice is a topological state, self-assembly techniques that could create such a lattice may be able to generate open lattices with topologically-protected novel properties.

A seemingly viable way to do this would be by exploiting the highly-directional binding of anisotropic capillary interactions. If triangles of specific non-equilateral geometries, or if two different shapes and sizes of non-equilateral triangles, could be fabricated, deformed kagome lattices that emulate those found in [7, 87], with novel and potentially topological properties, could manifest. Of course, in order to do so, isolating the fabricated prisms so that only a single bowing polarity is present, specifically designing the tips and their corresponding interactions to significantly favor certain tip-tip pairings to generate a deformed lattice structure with minimal defects, and also stabilizing the tip-to-tip binding, are all seemingly necessary hurdles to overcome in order to achieve the desired results. Stabilization of tip-to-tip binding could occur via a small blunting of the tips to mechanically prevent collapse. Other mechanisms for preventing collapse, such as making the centers of the particles' side faces repulsive, could also be explored further. Tip-tip pairings could perhaps be specified by fabricating bowed triangles with tips at varying heights. Consequently, tips of different triangles with the same height would encounter the strongest capillary attraction, as their combining would minimize excess area the most. Additionally, it would also be interesting to see if certain configurations of Janus particles and/or patches could allow for the creation of the desired deformed kagome lattices in order to attempt to create topological open structures.

Finally, subsequent study is needed to further understand the effect of thermal fluctuations on mechanical instability and associated phase transitions. It would be useful to study finite-temperature transitions between polymorphs in three-dimensional lattices to see which

results generalize. There is also interest in the analysis of topological phase transitions at finite temperature. For instance, introducing next-nearest neighbor bonds with a varying harmonic spring cofficient to a deformed kagome lattice and doing a similar analysis to that of Chapter III would be insightful and could lead to intriguing results.

APPENDICES

APPENDIX A

Deriving the effective force for an extensible rod

In this section, we derive the effective force as prescribed in Eq. (2.2.59). Starting from Eq. (2.2.37) and building on the calculations of Sec. 2.2.3, we have that

$$\begin{aligned} F^{<}(\boldsymbol{\pi}^{<}) &= H_0 + H_2(\boldsymbol{\pi}^{<}) + \langle H_4 \rangle_{>} - T \ln Z_0^{>} \\ &= H_0 + F_2^{<}(\boldsymbol{\pi}^{<}) + F_4^{<}(\boldsymbol{\pi}^{<}) - T \ln Z_0^{>} + O(T^2), \end{aligned} \tag{A.1}$$

with $F_2^{<}(\boldsymbol{\pi}^{<})$ defined as in Eq. (2.2.38), and $F_4^{<}(\boldsymbol{\pi}^{<})$ containing terms of quartic order in $\boldsymbol{\pi}^{<}$. The $O(T^2)$ terms, arising from four-point correlation functions of $\boldsymbol{\pi}^{>}$, can be discarded. It is more convenient, going forward, to write $F_2^{<}$ and $F_4^{<}$ in terms of $\boldsymbol{\pi}_1$:

$$F_2^{<} = \frac{\tilde{\tau} + \tilde{\kappa}\frac{\pi^2}{L_0^2}}{4L_0} |\boldsymbol{\pi}_1|^2 \equiv b_2 T |\boldsymbol{\pi}_1|^2 \tag{A.2}$$

and

$$F_4^{<} = \frac{-\frac{3}{2}\tau + 5\tau_c(0) + gL_0}{32L_0^3} |\boldsymbol{\pi}_1|^4 \approx \frac{g}{32L_0^2} |\boldsymbol{\pi}_1|^4 \equiv b_4 T |\boldsymbol{\pi}_1|^4, \tag{A.3}$$

where

$$b_2 \equiv \frac{\tilde{\tau} + \tilde{\kappa}\frac{\pi^2}{L_0^2}}{4TL_0}$$
$$b_4 \equiv \frac{g}{32TL_0^2}. \tag{A.4}$$

Once again, we have taken the limit of the stretching stiffness being much stronger than the bending stiffness in simplifying the expression for $F_4^<$. Thus, the Landau free energy becomes

$$F^< = H_0 - T\ln Z_0^> + b_2 T|\boldsymbol{\pi}_1|^2 + b_4 T|\boldsymbol{\pi}_1|^4. \tag{A.5}$$

Since the first two terms are independent of $\boldsymbol{\pi}_1$, we can easily obtain an expression for the free energy,

$$F = H_0 - T\ln Z_0^> - T\ln \int_{-\infty}^{\infty} d^{d-1}\boldsymbol{\pi}_1 e^{-b_2|\boldsymbol{\pi}_1|^2 - b_4|\boldsymbol{\pi}_1|^4}. \tag{A.6}$$

We now proceed to compute the latter two terms in this expression.

First,

$$\begin{aligned} -T\ln Z_0^> &= -T\ln \int \mathcal{D}\boldsymbol{\pi}^> e^{-H_2(\boldsymbol{\pi}^>)/T} \\ &= -T\ln \prod_{n=2}^{\infty} \left(\frac{4\pi TL_0}{\tau + \kappa(\pi n/L_0)^2}\right)^{\frac{d-1}{2}} \\ &= -\frac{T(d-1)}{2}\sum_{n=2}^{\infty} \ln \frac{4\pi TL_0}{\tau + \kappa(\pi n/L_0)^2}. \end{aligned} \tag{A.7}$$

Second, we need to evaluate the integral

$$Z_1 \equiv \int_{-\infty}^{\infty} d^{d-1}\boldsymbol{\pi}_1 e^{-b_2|\boldsymbol{\pi}_1|^2 - b_4|\boldsymbol{\pi}_1|^4}. \tag{A.8}$$

This integral can be evaluated using the $(d-1)$-dimensional spherical coordinates; we find

$$Z_1 = \frac{1}{4} b_4^{-\frac{d-1}{4}} \Omega_{d-1} \Bigg[\Gamma\left(\frac{d-1}{4}\right) {}_1F_1\left(\frac{d-1}{4}; \frac{1}{2}; \frac{c}{4}\right) \mp \sqrt{c}\, \Gamma\left(\frac{d+1}{4}\right) {}_1F_1\left(\frac{d+1}{4}; \frac{3}{2}; \frac{c}{4}\right) \Bigg], \tag{A.9}$$

where Ω_{d-1} is the solid angle subtended by the $(d-1)$-dimensional hypersphere, the dimensionless number

$$c \equiv \frac{|b_2|^2}{b_4} = \frac{2\left(\tilde{\tau} + \tilde{\kappa}\frac{\pi^2}{L_0^2}\right)^2}{gT}, \tag{A.10}$$

and ${}_1F_1$ represents the Kummer confluent hypergeometric function. The $-$ sign in Eq. (A.9) applies to $b_2 > 0$, which is the straight phase, whereas the $+$ sign corresponds to $b_2 < 0$, the buckled phase.

To better understand the expression in Eq. (A.9), we expand it in different regimes. The behavior of the ${}_1F_1$ function takes different limits for $c \ll 1$ (close to the transition – the *critical* regime) and $c \gg 1$ (far from the transition). The boundary between these two regimes, determined by $c \sim 1$, is indicated by the dashed curves in Figs. 2.1 and 2.3. For $c \ll 1$, we have

$$Z_1 \approx \frac{1}{4} b_4^{-\frac{d-1}{4}} \Omega_{d-1} \Gamma\left(\frac{d-1}{4}\right) \left[1 - \tilde{\Gamma}\frac{b_2}{\sqrt{b_4}} + \frac{d-1}{8}\frac{|b_2|^2}{b_4}\right], \tag{A.11}$$

where $\tilde{\Gamma} \equiv \Gamma(\frac{d+1}{4})/\Gamma(\frac{d-1}{4})$. For $c \gg 1$, the asymptotic expressions depend on the phase of the rod: for the straight phase ($b_2 > 0$),

$$Z_1 = \frac{1}{2}\Omega_{d-1}\Gamma\left(\frac{d-1}{2}\right) b_2^{-\frac{d-1}{2}}, \tag{A.12}$$

while for the buckled phase ($b_2 < 0$),

$$Z_1 = \frac{\sqrt{\pi}}{2^{\frac{d-1}{2}}} \Omega_{d-1} |b_2|^{\frac{d-3}{2}} b_4^{-\frac{d-2}{2}} e^{c/4}. \tag{A.13}$$

The expressions for Z_1 in the $c \gg 1$ regime yield simple expressions when specializing to $d = 2$ and $d = 3$, so it is useful to explicitly list them:

$$Z_1 = \begin{cases} \sqrt{\pi/b_2} & b_2 > 0 \text{ and } d = 2, \\ \pi/b_2 & b_2 > 0 \text{ and } d = 3, \\ \sqrt{2\pi/|b_2|}\, e^{c/4} & b_2 < 0 \text{ and } d = 2, \\ \sqrt{\pi^3/b_4}\, e^{c/4} & b_2 < 0 \text{ and } d = 3. \end{cases} \tag{A.14}$$

The $e^{c/4}$ factor in the latter two equations comes from the finite expectation value of $\boldsymbol{\pi}_1$ when $b_2 < 0$. It is straightforward to see this by plugging $\hat{\boldsymbol{\pi}}_1$ – as given in Eq. (2.2.28) – into H.

Next, we put the terms together and derive the effective force. Following Eq. (2.2.59),

$$\begin{aligned} f &= \frac{\partial H_0}{\partial L_0} - Tg\frac{\partial}{\partial \tau} \ln Z_0^{>} - Tg\frac{\partial}{\partial \tau} \ln Z_1 \\ &= \tau + \frac{d-1}{2}\bar{g}\bar{T}|\tau_c(0)|\mathcal{A}(\bar{\tau}) + f_1, \end{aligned} \tag{A.15}$$

where f_1 is from the $\ln Z_1$ term and can be expanded in the various limits.

In the critical regime, we use Eq. (A.11) and find

$$\begin{aligned} f_1 = &\left(\tilde{\Gamma}\sqrt{2gT} + \frac{1 - d + 4\tilde{\Gamma}^2}{2}\left(\tilde{\tau} + \tilde{\kappa}\frac{\pi^2}{L_0^2}\right)\right) \\ &\times \left(1 - (d-1)\bar{g}\bar{T}\mathcal{A}'(\bar{\tau})\right), \end{aligned} \tag{A.16}$$

where $\mathcal{A}'(\bar{\tau})$ is the derivative of $\mathcal{A}(\bar{\tau})$ with respect to $\bar{\tau}$. Deep in the straight phase, we use Eq. (A.12) to obtain

$$f_1 = \frac{d-1}{2}\frac{gT}{\tilde{\tau} + \tilde{\kappa}(\pi/L_0)^2}\left(1 - (d-1)\bar{g}\bar{T}\mathcal{A}'(\bar{\tau})\right), \tag{A.17}$$

while deep in the buckled phase, Eq. (A.13) gives us

$$f_1 = \left(-\tilde{\tau} - \tilde{\kappa}\frac{\pi^2}{L_0^2} + \frac{3-d}{2}\frac{gT}{\tilde{\tau} + \tilde{\kappa}(\pi/L_0)^2}\right) \times \left(1 - (d-1)\bar{g}\bar{T}\mathcal{A}'(\bar{\tau})\right). \tag{A.18}$$

In the latter regimes, where $c \gg 1$, it turns out that $\bar{g}\bar{T} \ll 1$; therefore, we can write the expressions for f_1 to $O(\bar{g}\bar{T})$. The complete force expressions then simply become a leading-order term plus an $O(\bar{g}\bar{T})$ correction. Specifically, in the straight phase,

$$f_1 = \frac{d-1}{2}\bar{g}\bar{T}|\tau_c(0)|\frac{1}{1-\bar{\tau}}, \tag{A.19}$$

so that

$$f = \tau + \frac{d-1}{2}\bar{g}\bar{T}|\tau_c(0)|\left[\mathcal{A}(\bar{\tau}) + \frac{1}{1-\bar{\tau}}\right], \tag{A.20}$$

and in the buckled phase,

$$f_1 = \tau_c(0) - \tau - \bar{g}\bar{T}|\tau_c(0)|\left[(d-1)\mathcal{A}'(\bar{\tau})(\bar{\tau}-1) + (d-1)\mathcal{A}(\bar{\tau}) + \frac{3-d}{2}\frac{1}{\bar{\tau}-1}\right], \tag{A.21}$$

so that

$$f = \tau_c(0) - \bar{g}\bar{T}|\tau_c(0)|\left[(d-1)\mathcal{A}'(\bar{\tau})(\bar{\tau}-1) + \frac{d-1}{2}\mathcal{A}(\bar{\tau}) + \frac{3-d}{2}\frac{1}{\bar{\tau}-1}\right]. \tag{A.22}$$

Notice the major difference between the two final expressions for the effective force: deep in the straight phase, the force is just the original and unmodified compression with a small

$O(\bar{g}\bar{T})$ correction; on the other hand, deep in the buckled phase, the force is the zero-temperature critical compression with a small correction of the same order.

The critical regime, however, is not constrained to only small values of $\bar{g}\bar{T}$, so a similar expansion cannot be made everywhere; therefore, we further divide this regime into two limiting cases. In the region where $\bar{g}\bar{T} \ll 1$, Eq. (A.16) becomes

$$f_1 = \tilde{\Gamma}\sqrt{2gT} + (\tau - \tau_c(T))\frac{1 - d + 4\tilde{\Gamma}^2}{2}, \tag{A.23}$$

where we discard all corrections of $O(\bar{g}\bar{T})$ and also note that $\tau - \tau_c(0) = \tau - \tau_c(T) + O(\bar{g}\bar{T})$, using Eq. (2.2.58). Furthermore, in this regime, τ will deviate minimally from $\tau_c(T)$; therefore, we can simply take $f_1 \approx \tilde{\Gamma}\sqrt{2gT}$ – which is indeed the value of f_1 on the transition curve – as a reasonable approximation for the entire critical region (for $\bar{g}\bar{T} \ll 1$). Thus, the total force in this regime is

$$f = \tau + \tilde{\Gamma}\sqrt{2gT}, \tag{A.24}$$

which indicates an $O(\sqrt{T})$ correction to the force in the critical regime.

Finally, when $\bar{g}\bar{T} \sim O(1)$ in the critical regime, the f_1 contribution to the total force is suppressed, as $1 - (d-1)\bar{g}\bar{T}\mathcal{A}'(\bar{\tau}) \approx 0$. In this case,

$$f = \tau + \frac{d-1}{2}\bar{g}\bar{T}|\tau_c(0)|\mathcal{A}(\bar{\tau}), \tag{A.25}$$

and there is, once again, an $O(\bar{g}\bar{T})$ correction to the compression.

APPENDIX B

The kagome lattice dynamical matrix

The central force potentials and their derivatives are given by

$$V_{NN} = \frac{k}{2}(\Delta R)^2 \qquad V'_{NN} = k\Delta R \qquad V''_{NN} = k \tag{B.1}$$

$$V_{NNN} = \frac{\kappa}{2}(\Delta R)^2 + \frac{g}{24}(\Delta R)^4 \qquad V'_{NNN} = \kappa\Delta R + \frac{g}{6}(\Delta R)^3 \qquad V''_{NNN} = \kappa + \frac{g}{2}(\Delta R)^2 \tag{B.2}$$

Recall that $\mathbf{A}_B$ contains $V'_{B\alpha} \equiv V'_B(|\mathbf{R}_B^\alpha| - |\mathbf{R}_B^{\alpha_0}|)$ and $V''_{B\alpha}$. Since the length of any NN bond is independent of the twisting angle, $|\mathbf{R}_B^\alpha| = |\mathbf{R}_B^{\alpha_0}|$; therefore,

$$V'_{B\alpha} = 0 \quad \text{and} \quad V''_{B\alpha} = k \quad \text{(NN bonds)}. \tag{B.3}$$

Then

$$\mathbf{A}_B = k\hat{\mathbf{t}}_B^\alpha \hat{\mathbf{t}}_B^\alpha \quad \text{(NN bonds)}. \tag{B.4}$$

B.1 The nearest-neighbor dynamical matrix

For the three intercellular NN bonds, $\mathbf{l}_B$ in (3.4.18) is equal to the lattice vector connecting the two unit cells together. In particular,

$$\begin{aligned}\mathbf{l}_1 &\equiv (1,\sqrt{3})a\cos\alpha \\ \mathbf{l}_2 &\equiv -(2,0)a\cos\alpha \\ \mathbf{l}_3 &\equiv (1,-\sqrt{3})a\cos\alpha\end{aligned} \tag{B.1}$$

The dynamical matrix can be written in terms of 2×2 block matrices,

$$\mathbf{D}_{\mathbf{q}} = k\begin{pmatrix}\mathbf{D}_{11} & \mathbf{D}_{12} & \mathbf{D}_{13}\\ \mathbf{D}_{21} & \mathbf{D}_{22} & \mathbf{D}_{23}\\ \mathbf{D}_{31} & \mathbf{D}_{32} & \mathbf{D}_{33}\end{pmatrix} = \begin{pmatrix}\mathbf{D}_{11} & \mathbf{D}_{12} & \mathbf{D}_{13}\\ \mathbf{D}_{12}^{\dagger} & \mathbf{D}_{22} & \mathbf{D}_{23}\\ \mathbf{D}_{13}^{\dagger} & \mathbf{D}_{23}^{\dagger} & \mathbf{D}_{33}\end{pmatrix} \tag{B.2}$$

with

$$\mathbf{D}_{11} = \begin{pmatrix}2-\cos 2\alpha & 0\\ 0 & 2+\cos 2\alpha\end{pmatrix} \tag{B.3}$$

$$\mathbf{D}_{12} = \frac{1}{4}\begin{pmatrix}\mathfrak{a}_{12} & \mathfrak{b}_{12}\\ \mathfrak{c}_{12} & \mathfrak{d}_{12}\end{pmatrix} = \frac{1}{4}\begin{pmatrix}\mathfrak{a}_{12} & \mathfrak{b}_{12}\\ \mathfrak{b}_{12} & \mathfrak{d}_{12}\end{pmatrix} \tag{B.4}$$

where

$$\mathfrak{a}_{12} = -2+\cos 2\alpha+\sqrt{3}\sin 2\alpha - e^{-i\mathbf{l}_1\cdot\mathbf{q}}\left(2-\cos 2\alpha+\sqrt{3}\sin 2\alpha\right) \tag{B.5}$$

$$\mathfrak{b}_{12} = -\sqrt{3}\cos 2\alpha+\sin 2\alpha - e^{-i\mathbf{l}_1\cdot\mathbf{q}}\left(\sqrt{3}\cos 2\alpha+\sin 2\alpha\right) \tag{B.6}$$

$$\mathfrak{d}_{12} = -2-\cos 2\alpha-\sqrt{3}\sin 2\alpha - e^{-i\mathbf{l}_1\cdot\mathbf{q}}\left(2+\cos 2\alpha-\sqrt{3}\sin 2\alpha\right) \tag{B.7}$$

$$\mathbf{D}_{13} = \frac{1}{4}\begin{pmatrix} \mathfrak{a}_{13} & \mathfrak{b}_{13} \\ \mathfrak{c}_{13} & \mathfrak{d}_{13} \end{pmatrix} = \frac{1}{4}\begin{pmatrix} \mathfrak{a}_{13} & \mathfrak{b}_{13} \\ \mathfrak{b}_{13} & \mathfrak{d}_{13} \end{pmatrix} \tag{B.8}$$

where

$$\mathfrak{a}_{13} = -2 + \cos 2\alpha - \sqrt{3}\sin 2\alpha - e^{i\mathbf{l}_3\cdot\mathbf{q}}\left(2 - \cos 2\alpha - \sqrt{3}\sin 2\alpha\right) \tag{B.9}$$

$$\mathfrak{b}_{13} = \sqrt{3}\cos 2\alpha + \sin 2\alpha + e^{i\mathbf{l}_3\cdot\mathbf{q}}\left(\sqrt{3}\cos 2\alpha - \sin 2\alpha\right) \tag{B.10}$$

$$\mathfrak{d}_{13} = -2 - \cos 2\alpha + \sqrt{3}\sin 2\alpha - e^{i\mathbf{l}_3\cdot\mathbf{q}}\left(2 + \cos 2\alpha + \sqrt{3}\sin 2\alpha\right) \tag{B.11}$$

$$\mathbf{D}_{22} = \frac{1}{2}\begin{pmatrix} 4 + \cos 2\alpha & \sqrt{3}\cos 2\alpha \\ \sqrt{3}\cos 2\alpha & 4 - \cos 2\alpha \end{pmatrix} \tag{B.12}$$

$$\mathbf{D}_{23} = \begin{pmatrix} \left(-1 - e^{-i\mathbf{l}_2\cdot\mathbf{q}}\right)\cos^2\alpha & \left(-1 + e^{-i\mathbf{l}_2\cdot\mathbf{q}}\right)\cos\alpha\sin\alpha \\ \left(-1 + e^{-i\mathbf{l}_2\cdot\mathbf{q}}\right)\cos\alpha\sin\alpha & \left(-1 - e^{-i\mathbf{l}_2\cdot\mathbf{q}}\right)\sin^2\alpha \end{pmatrix} \tag{B.13}$$

APPENDIX C

Deriving the three-band effective dynamical matrix

At any point $\mathbf{q}$ in the first Brillouin zone (though typically this is done at $\mathbf{q} = 0$), the dynamical matrix can be diagonalized such that its three low-energy modes and three high-energy modes are decoupled for all values of $\mathbf{q}$ as

$$\mathbf{D}_{\mathbf{q}} = \begin{pmatrix} \mathbf{D}_{LL} & \mathbf{D}_{LH} \\ \mathbf{D}_{HL} & \mathbf{D}_{HH} \end{pmatrix} \tag{C.1}$$

The resultant Hamiltonian of the system is, then,

$$\begin{aligned} H &= \frac{1}{2} \begin{pmatrix} \mathbf{u}_L^\dagger & \mathbf{u}_H^\dagger \end{pmatrix} \begin{pmatrix} \mathbf{D}_{LL} & \mathbf{D}_{LH} \\ \mathbf{D}_{HL} & \mathbf{D}_{HH} \end{pmatrix} \begin{pmatrix} \mathbf{u}_L \\ \mathbf{u}_H \end{pmatrix} \\ &= \frac{1}{2} \left(\mathbf{u}_L^\dagger \mathbf{D}_{LL} \mathbf{u}_L + \mathbf{u}_L^\dagger \mathbf{D}_{LH} \mathbf{u}_H + \mathbf{u}_H^\dagger \mathbf{D}_{HL} \mathbf{u}_L + \mathbf{u}_H^\dagger \mathbf{D}_{HH} \mathbf{u}_H \right) \end{aligned} \tag{C.2}$$

where $\mathbf{u}_L$ ($\mathbf{u}_H$) corresponds to low-energy (high-energy) fluctuations. Because the $\mathbf{u}_H$ modes are high-energy, they are "frozen out" and not affected by thermal fluctuations; they should be at equilibrium, as determined by the Hamiltonian. Therefore, for a given $\mathbf{u}_L$, we require

$\mathbf{u}_H$ to take values such that

$$\frac{\partial H}{\partial \mathbf{u}_H} = 0. \tag{C.3}$$

$$0 = \frac{\partial H}{\partial \mathbf{u}_H} = \frac{1}{2}\left(\mathbf{u}_L^\dagger \mathbf{D}_{LH} + \mathbf{u}_H^\dagger \mathbf{D}_{HH}\right), \tag{C.4}$$

where we note that

$$\frac{\partial \mathbf{u}_H^\dagger}{\partial \mathbf{u}_H} = 0, \tag{C.5}$$

analogous to how

$$\frac{\partial z^*}{\partial z} = \frac{1}{2}\left(\frac{\partial}{\partial x} - i\frac{\partial}{\partial y}\right)(x - iy) = 0. \tag{C.6}$$

for complex variables.

Note that the dynamical matrix is Hermitian and, therefore,

$$\begin{aligned} \mathbf{D}_{LL}^\dagger &= \mathbf{D}_{LL} & \mathbf{D}_{LH}^\dagger &= \mathbf{D}_{HL} \\ \mathbf{D}_{HL}^\dagger &= \mathbf{D}_{LH} & \mathbf{D}_{HH}^\dagger &= \mathbf{D}_{HH} \end{aligned} \tag{C.7}$$

Taking the Hermitian conjugate of both sides, we have

$$0 = \mathbf{D}_{LH}^\dagger \mathbf{u}_L + \mathbf{D}_{HH}^\dagger \mathbf{u}_H = \mathbf{D}_{HL}\mathbf{u}_L + \mathbf{D}_{HH}\mathbf{u}_H, \tag{C.8}$$

allowing us to solve for $\mathbf{u}_H$:

$$\mathbf{u}_H = -\mathbf{D}_{HH}^{-1}\mathbf{D}_{HL}\mathbf{u}_L. \tag{C.9}$$

Plugging this expression for $\mathbf{u}_H$ into H, we have

$$\begin{aligned} H &= \frac{1}{2}\Big(\mathbf{u}_L^\dagger \mathbf{D}_{LL}\mathbf{u}_L - \mathbf{u}_L^\dagger \mathbf{D}_{LH}\mathbf{D}_{HH}^{-1}\mathbf{D}_{HL}\mathbf{u}_L - \mathbf{u}_L^\dagger \mathbf{D}_{HL}^\dagger \left(\mathbf{D}_{HH}^{-1}\right)^\dagger \mathbf{D}_{HL}\mathbf{u}_L \\ &\qquad\qquad + \mathbf{u}_L^\dagger \mathbf{D}_{HL}^\dagger \left(\mathbf{D}_{HH}^{-1}\right)^\dagger \mathbf{D}_{HH}\mathbf{D}_{HH}^{-1}\mathbf{D}_{HL}\mathbf{u}_L\Big) \\ &= \frac{1}{2}\Big(\mathbf{u}_L^\dagger \mathbf{D}_{LL}\mathbf{u}_L - \mathbf{u}_L^\dagger \mathbf{D}_{LH}\mathbf{D}_{HH}^{-1}\mathbf{D}_{HL}\mathbf{u}_L\Big) \\ &= \frac{1}{2}\mathbf{u}_L^\dagger \left(\mathbf{D}_{LL} - \mathbf{D}_{LH}\mathbf{D}_{HH}^{-1}\mathbf{D}_{HL}\right)\mathbf{u}_L \\ &= \frac{1}{2}\mathbf{u}_L^\dagger \widetilde{\mathbf{D}}_{LL}\mathbf{u}_L \end{aligned} \tag{C.10}$$

where

$$\widetilde{\mathbf{D}}_{LL} = \mathbf{D}_{LL} - \mathbf{D}_{LH}\mathbf{D}_{HH}^{-1}\mathbf{D}_{HL} \tag{C.11}$$

is the effective 3×3 dynamical matrix, true for all $\mathbf{q}$.

BIBLIOGRAPHY

BIBLIOGRAPHY

[1] J.-H. Lee, J. P. Singer, and E. L. Thomas, "Micro-/nanostructured mechanical metamaterials", Advanced materials **24**, 4782–4810 (2012).

[2] J. L. Silverberg, A. A. Evans, L. McLeod, R. C. Hayward, T. Hull, C. D. Santangelo, and I. Cohen, "Using origami design principles to fold reprogrammable mechanical metamaterials", science **345**, 647–650 (2014).

[3] Z. G. Nicolaou and A. E. Motter, "Mechanical metamaterials with negative compressibility transitions", arXiv preprint arXiv:1207.2185 (2012).

[4] J. N. Grima, R. Caruana-Gauci, M. R. Dudek, K. W. Wojciechowski, and R. Gatt, "Smart metamaterials with tunable auxetic and other properties", Smart Materials and Structures **22**, 084016 (2013).

[5] L. M. Nash, D. Kleckner, A. Read, V. Vitelli, A. M. Turner, and W. T. Irvine, "Topological mechanics of gyroscopic metamaterials", Proceedings of the National Academy of Sciences **112**, 14495–14500 (2015).

[6] B. Florijn, C. Coulais, and M. van Hecke, "Programmable mechanical metamaterials", Physical review letters **113**, 175503 (2014).

[7] D. Z. Rocklin, S. Zhou, K. Sun, and X. Mao, "Transformable topological mechanical metamaterials", Nature communications **8** (2017).

[8] P. R. Onck, T. Koeman, T. van Dillen, and E. van der Giessen, "Alternative explanation of stiffening in cross-linked semiflexible networks", Phys. Rev. Lett. **95**, 178102 (2005).

[9] C. P. Broedersz, X. Mao, T. C. Lubensky, and F. C. MacKintosh, "Criticality and isostaticity in fibre networks", Nat. Phys. **7**, 983–988 (2011).

[10] A. A. Shah, B. Schultz, W. Zhang, S. C. Glotzer, and M. J. Solomon, "Actuation of shape-memory colloidal fibres of janus ellipsoids", Nature materials **14**, 117 (2015).

[11] Y. Ke, T. Meyer, W. M. Shih, and G. Bellot, "Regulation at a distance of biomolecular interactions using a dna origami nanoactuator", Nature communications **7**, 10935 (2016).

[12] J. Villain, R. Bidaux, J.-P. Carton, and R. Conte, "Order as an effect of disorder", J. Phys. France **41**, 1263–1272 (1980).

[13] X. Mao, A. Souslov, C. I. Mendoza, and T. C. Lubensky, "Mechanical instability at finite temperature", Nat. Commun. **6**, 5968 (2015).

[14] K. D. Hammonds, M. T. Dove, A. P. Giddy, V. Heine, and B. Winkler, "Rigid-unit phonon modes and structural phase transitions in framework silicates", American Mineralogist **81**, 1057–1079 (1996).

[15] C. R. Morelock, B. K. Greve, L. C. Gallington, K. W. Chapman, and A. P. Wilkinson, "Negative thermal expansion and compressibility of sc1–x y x f3", Journal of Applied Physics **114**, 213501 (2013).

[16] J. C. Maxwell, "On the calculation of the equilibrium and stiffness of frames", Philos. Mag. **27**, 294 (1864).

[17] C. Calladine, "Buckminster fuller's structures and clerk maxwell's rules for the construction of stiff frames", Int. J. Solids Struct. **14**, 161 –172 (1978).

[18] T. Lubensky, C. Kane, X. Mao, A. Souslov, and K. Sun, "Phonons and elasticity in critically coordinated lattices", Reports on Progress in Physics **78**, 073901 (2015).

[19] S. Feng and P. N. Sen, "Percolation on elastic networks: new exponent and threshold", Phys. Rev. Lett. **52**, 216–219 (1984).

[20] D. J. Jacobs and M. F. Thorpe, "Generic rigidity percolation: the pebble game", Phys. Rev. Lett. **75**, 4051–4054 (1995).

[21] D. J. Jacobs and M. F. Thorpe, "Generic rigidity percolation in two dimensions", Phys. Rev. E **53**, 3682–3693 (1996).

[22] M. V. Chubynsky and M. F. Thorpe, "Algorithms for three-dimensional rigidity analysis and a first-order percolation transition", Phys. Rev. E **76**, 041135 (2007).

[23] A. J. Liu and S. R. Nagel, "Jamming is not just cool any more", Nature **396**, 21 (1998).

[24] M. Wyart, "On the rigidity of amorphous solids", Ann. Phys. Fr **30**, 1–96 (2005).

[25] M. van Hecke, "Jamming of soft particles: geometry, mechanics, scaling and isostaticity", English, J. Phys. Condens. Matter **22** (2010) {10.1088/0953-8984/22/3/033101}.

[26] A. J. Liu and S. R. Nagel, "The jamming transition and the marginally jammed solid", Annu. Rev. Condens. Matter Phys. **1**, 347–369 (2010).

[27] C. P. Broedersz and F. C. MacKintosh, "Modeling semiflexible polymer networks", Rev. Mod. Phys. **86**, 995 (2014).

[28] X. Mao, O. Stenull, and T. C. Lubensky, "Elasticity of a filamentous kagome lattice", Phys. Rev. E **87**, 042602 (2013).

[29] D. Bi, J. Zhang, B. Chakraborty, and R. P. Behringer, "Jamming by shear", Nature **480**, 355 (2011).

[30] D. J. Durian, "Foam mechanics at the bubble scale", Phys. Rev. Lett. **75**, 4780–4783 (1995).

[31] C. S. O'Hern, S. A. Langer, A. J. Liu, and S. R. Nagel, "Random packings of frictionless particles", Phys. Rev. Lett. **88**, 075507 (2002).

[32] C. S. O'Hern, L. E. Silbert, A. J. Liu, and S. R. Nagel, "Jamming at zero temperature and zero applied stress: the epitome of disorder", Phys. Rev. E **68**, 011306 (2003).

[33] G. M. Whitesides and B. Grzybowski, "Self-assembly at all scales", Science **295**, Times Cited: 2019, 2418–2421 (2002).

[34] J. A. Pelesko, *Self assembly: the science of things that put themselves together* (Chapman & Hall/CRC, 2007).

[35] S. Glotzer, M. Solomon, and N. A. Kotov, "Self-assembly: from nanoscale to microscale colloids", AIChE Journal **50**, 2978–2985 (2004).

[36] S. C. Glotzer and M. J. Solomon, "Anisotropy of building blocks and their assembly into complex structures", Nat. Mater. **6**, 557–562 (2007).

[37] D. Frenkel, "Entropy-driven phase transitions", Physica A: statistical mechanics and its applications **263**, 26–38 (1999).

[38] P. G. De Gennes, "Soft matter", Rev. Mod. Phys. **64**, 645–648 (1992).

[39] S. J. Ebbens and J. R. Howse, "In pursuit of propulsion at the nanoscale", Soft Matter **6**, 726–738 (2010).

[40] H. Xie, Z.-G. She, S. Wang, G. Sharma, and J. W. Smith, "One-step fabrication of polymeric janus nanoparticles for drug delivery", Langmuir **28**, 4459–4463 (2012).

[41] A. Walther and A. H. Müller, "Janus particles", Soft Matter **4**, 663–668 (2008).

[42] L. Hong, A. Cacciuto, E. Luijten, and S. Granick, "Clusters of charged janus spheres", Nano letters **6**, 2510–2514 (2006).

[43] S. Gangwal, O. J. Cayre, and O. D. Velev, "Dielectrophoretic assembly of metallodielectric janus particles in ac electric fields", Langmuir **24**, 13312–13320 (2008).

[44] H. Shin and K. S. Schweizer, "Theory of two-dimensional self-assembly of janus colloids: crystallization and orientational ordering", Soft Matter **10**, 262–274 (2014).

[45] Q. Chen, S. Bae, and S. Granick, "Directed self-assembly of a colloidal kagome lattice", Nature **469**, 381–384 (2011).

[46] X. Mao, Q. Chen, and S. Granick, "Entropy favours open colloidal lattices", Nat. Mater. **7**, 217 (2013).

[47] D. S. Bedi and X. Mao, "Finite-temperature buckling of an extensible rod", Physical Review E **92**, 062141 (2015).

[48] L. Euler, *Calculus of variations* (1744).

[49] L. D. Landau and E. M. Lifshitz, *Elasticity theory* (Pergamon Press, 1986).

[50] R. M. Jones, *Buckling of bars, plates, and shells* (Bull Ridge Corporation, 2006).

[51] A. K. Harris, P. Warner, and D. Stopak, "Generation of spatially periodic patterns by a mechanical instability: a mechanical alternative to the turing model", J Embryol Exp Morphol. **80**, 1–20 (1984).

[52] M Kücken and A. Newell, "A model for fingerprint formation", Europhys. Lett. **68**, 141 (2004).

[53] T. Mullin, S. Deschanel, K. Bertoldi, and M. C. Boyce, "Pattern transformation triggered by deformation", Phys. Rev. Lett. **99**, 084301 (2007).

[54] M. Das, A. J. Levine, and F. MacKintosh, "Buckling and force propagation along intracellular microtubules", Europhys. Lett. **84**, 18003 (2008).

[55] D. R. Kovar and T. D. Pollard, "Insertional assembly of actin filament barbed ends in association with formins produces piconewton forces", Proc. Natl. Acad. Sci. U. S. A. **101**, 14725–14730 (2004).

[56] M. Dogterom and B. Yurke, "Measurement of the force-velocity relation for growing microtubules", Science **278**, 856–860 (1997).

[57] C. P. Brangwynne, F. C. MacKintosh, S. Kumar, N. A. Geisse, J. Talbot, L Mahadevan, K. K. Parker, D. E. Ingber, and D. A. Weitz, "Microtubules can bear enhanced compressive loads in living cells because of lateral reinforcement", J. Cell Biol. **173**, 733–741 (2006).

[58] S. Y. Ryu, J. Xiao, W. I. Park, K. S. Son, Y. Y. Huang, U. Paik, and J. A. Rogers, "Lateral buckling mechanics in silicon nanowires on elastomeric substrates", Nano Lett. **9**, 3214–3219 (2009).

[59] T. Kuzumaki and Y. Mitsuda, "Nanoscale mechanics of carbon nanotube evaluated by nanoprobe manipulation in transmission electron microscope", Jpn. J. Appl. Phys. **45**, 364 (2006).

[60] L. Zhang and X. Mao, "Finite-temperature mechanical instability in disordered lattices", Physical Review E **93**, 022110 (2016).

[61] X. Mao, "Entropic effects in the self-assembly of open lattices from patchy particles", Phys. Rev. E **87**, 062319 (2013).

[62] D. Z. Rocklin and X. Mao, "Self-assembly of three-dimensional open structures using patchy colloidal particles", Soft Matter **10**, 7569 (2014).

[63] M. Dennison, M. Sheinman, C. Storm, and F. C. MacKintosh, "Fluctuation-stabilized marginal networks and anomalous entropic elasticity", Phys. Rev. Lett. **111**, 095503 (2013).

[64] M. J. Bowick and L. Giomi, "Two-dimensional matter: order, curvature and defects", Adv. Phys. **58**, 449–563 (2009).

[65] T. Odijk, "Microfibrillar buckling within fibers under compression", J. Chem. Phys. **108**, 6923 (1998).

[66] P. L. Hansen, V. Adrian Parsegian, and R. Podgornik, "Buckling, fluctuations, and collapse in semiflexible polyelectrolytes", Phys. Rev. E **60**, 1956–1966 (1999).

[67] S. Carr, W. Lawrence, and M. Wybourne, "Accessibility of quantum effects in mesomechanical systems", Physical Review B **64**, 220101 (2001).

[68] W. Lawrence, "Phonon description and the euler buckling instability of a mesoscopic bar at fixed strain", Physica B **316**, 448–451 (2002).

[69] K. Baczynski, R. Lipowsky, and J. Kierfeld, "Stretching of buckled filaments by thermal fluctuations", Phys. Rev. E **76**, 061914 (2007).

[70] J. Blundell and E. Terentjev, "Buckling of semiflexible filaments under compression", Soft Matter **5**, 4015–4020 (2009).

[71] M. Emanuel, H. Mohrbach, M. Sayar, H. Schiessel, "Buckling of stiff polymers: influence of thermal fluctuations", Phys. Rev. E **76**, 061907 (2007).

[72] L. Golubovic, D. Moldovan, and A. Peredera, "Flexible polymers and thin rods far from equilibrium: buckling dynamics", Phys. Rev. E **61**, 1703 (2000).

[73] T. Odijk, "Stiff chains and filaments under tension", Macromolecules **28**, 7016–7018 (1995).

[74] P. Gutjahr, R. Lipowsky, and J. Kierfeld, "Persistence length of semiflexible polymers and bending rigidity renormalization", EPL (Europhysics Letters) **76**, 994 (2006).

[75] K Binder, "Critical properties from monte carlo coarse graining and renormalization", Physical Review Letters **47**, 693 (1981).

[76] W. Shan, Z Chen, C. Broedersz, A. Gumaste, W. Soboyejo, and C. Brangwynne, "Attenuated short wavelength buckling and force propagation in a biopolymer-reinforced rod", Soft Matter **9**, 194–199 (2013).

[77] X. Mao, N. Xu, and T. C. Lubensky, "Soft modes and elasticity of nearly isostatic lattices: randomness and dissipation", Phys. Rev. Lett. **104**, 085504 (2010).

[78] A. J. Liu, S. R. Nagel, W. van Saarloos, and M. Wyart, "The jamming scenario - an introduction and outlook", in *Dynamical heterogeneities in glasses, colloids, and granular media*, edited by L. Berthier, G. Biroli, J.-P. Bouchaud, L. Cipeletti, and W. van Saarloos (Oxford University Press, 2010) Chap. 9.

[79] W. G. Ellenbroek and X. Mao, "Rigidity percolation on the square lattice", Europhys. Lett. **96** (2011).

[80] X. Mao and T. C. Lubensky, "Coherent potential approximation of random nearly isostatic kagome lattice", Phys. Rev. E **83**, 011111 (2011).

[81] X. Mao, O. Stenull, and T. C. Lubensky, "Effective-medium theory of a filamentous triangular lattice", Phys. Rev. E **87**, 042601 (2013).

[82] L. Zhang, D. Z. Rocklin, B. G.-g. Chen, and X. Mao, "Rigidity percolation by next-nearest-neighbor bonds on generic and regular isostatic lattices", Phys. Rev. E **91**, 032124 (2015).

[83] X. Mao, P. M. Goldbart, X. Xing, and A. Zippelius, "Soft random solids and their heterogeneous elasticity", Phys. Rev. E **80**, 031140 (2009).

[84] M. J. Bowick, S. M. Catterall, M. Falcioni, G. Thorleifsson, and K. N. Anagnostopoulos, "The flat phase of crystalline membranes", Journal de Physique I **6**, 1321–1345 (1996).

[85] J. Paulose, G. A. Vliegenthart, G. Gompper, and D. R. Nelson, "Fluctuating shells under pressure", Proceedings of the National Academy of Sciences **109**, 19551–19556 (2012).

[86] K. Sun, A. Souslov, X. Mao, and T. C. Lubensky, "Surface phonons, elastic response, and conformal invariance in twisted kagome lattices", Proc. Natl. Acad. Sci. U. S. A. **109**, 12369–12374 (2012).

[87] C. L. Kane and T. C. Lubensky, "Topological boundary modes in isostatic lattices", Nat. Phys. **10**, 39–45 (2014).

[88] S. A. Brazovskii, "Phase-transition of an isotropic system to an inhomogeneous state", Russian, Zh Eksp Teor Fiz **68**, 175–185 (1975).

[89] Q. Chen, E. Diesel, J. K. Whitmer, S. C. Bae, E. Luijten, and S. Granick, "Triblock colloids for directed self-assembly", J. Am. Chem. Soc. **133**, 7725–7727 (2011).

[90] B. Madivala, J. Fransaer, and J. Vermant, "Self-assembly and rheology of ellipsoidal particles at interfaces", Langmuir **25**, 2718–2728 (2009).

[91] B. Madivala, S. Vandebril, J. Fransaer, and J. Vermant, "Exploiting particle shape in solid stabilized emulsions", Soft Matter **5**, 1717–1727 (2009).

[92] K. D. Danov, P. A. Kralchevsky, B. N. Naydenov, and G. Brenn, "Interactions between particles with an undulated contact line at a fluid interface: capillary multipoles of arbitrary order", Journal of colloid and interface science **287**, 121–134 (2005).

[93] D. Stamou, C. Duschl, and D. Johannsmann, "Long-range attraction between colloidal spheres at the air-water interface: the consequence of an irregular meniscus", Physical Review E **62**, 5263 (2000).

[94] T. Young, "An essay on the cohesion of fluids", Philosophical Transactions of the Royal Society of London **95**, 65–87 (1805).

[95] P.-G. De Gennes, F. Brochard-Wyart, and D. Quéré, *Capillarity and wetting phenomena: drops, bubbles, pearls, waves* (Springer Science & Business Media, 2013).

[96] D. Chan, J. Henry, and L. White, "The interaction of colloidal particles collected at fluid interfaces", Journal of Colloid and Interface Science **79**, 410–418 (1981).

[97] B. P. Binks and T. S. Horozov, *Colloidal particles at liquid interfaces* (Cambridge University Press, 2006).

[98] P. Kralchevsky, V. Paunov, N. Denkov, I. Ivanov, and K Nagayama, "Energetical and force approaches to the capillary interactions between particles attached to a liquid-fluid interface", Journal of colloid and interface science **155**, 420–437 (1993).

[99] J.-C. Loudet, A. M. Alsayed, J. Zhang, and A. G. Yodh, "Capillary interactions between anisotropic colloidal particles", Physical review letters **94**, 018301 (2005).

[100] J.-C. Loudet, A. G. Yodh, and B. Pouligny, "Wetting and contact lines of micrometer-sized ellipsoids", Physical review letters **97**, 018304 (2006).

[101] E. P. Lewandowski, M. Cavallaro Jr, L. Botto, J. C. Bernate, V. Garbin, and K. J. Stebe, "Orientation and self-assembly of cylindrical particles by anisotropic capillary interactions", Langmuir **26**, 15142–15154 (2010).

[102] J. W. Gibbs, *The scientific papers of j. willard gibbs*, Vol. 1 (Longmans, Green and Company, 1906).

[103] P Singh and D. Joseph, "Fluid dynamics of floating particles", Journal of Fluid Mechanics **530**, 31–80 (2005).

[104] F. Dutka, M. Napiórkowski, and S. Dietrich, "Mesoscopic analysis of gibbs criterion for sessile nanodroplets on trapezoidal substrates", The Journal of chemical physics **136**, 064702 (2012).

[105] J. Ally, M. Kappl, and H.-J. Butt, "Adhesion of particles with sharp edges to air–liquid interfaces", Langmuir **28**, 11042–11047 (2012).

[106] N. Chatterjee and M. Flury, "Effect of particle shape on capillary forces acting on particles at the air–water interface", Langmuir **29**, 7903–7911 (2013).

[107] C. Extrand and S. I. Moon, "Contact angles on spherical surfaces", Langmuir **24**, 9470–9473 (2008).

[108] E. P. Lewandowski, P. C. Searson, and K. J. Stebe, "Orientation of a nanocylinder at a fluid interface", The Journal of Physical Chemistry B **110**, 4283–4290 (2006).

[109] J. Ferrar, "Self-assembly and high-rate projection of colloids and microprisms", PhD thesis (University of Michigan, 2017).

[110] K. A. Brakke, "The surface evolver", Experimental mathematics **1**, 141–165 (1992).

[111] E. P. Lewandowski, J. A. Bernate, A. Tseng, P. C. Searson, and K. J. Stebe, "Oriented assembly of anisotropic particles by capillary interactions", Soft Matter **5**, Times Cited: 20, 886–890 (2009).

[112] L. Botto, E. P. Lewandowski, M. Cavallaro, and K. J. Stebe, "Capillary interactions between anisotropic particles", Soft Matter **8**, 9957–9971 (2012).